Metal Oxide Nanostructures for Sensor Applications

D. Nunes*, A. Pimentel, A. Gonçalves, S. Pereira, R. Branquinho, P. Barquinha, E. Fortunato, and R. Martins*

i3N/CENIMAT, Department of Materials Science, Faculty of Sciences and Technology, Universidade NOVA de Lisboa, Campus de Caparica, 2829-516 Caparica

Abstract

Human health, environmental protection and safety are just a few examples of current humankind main concerns, that drive the scientific community to develop sensors able to precisely monitor and alert to possible harms in real time. Over the years, semiconductor metal oxide-based materials have been largely employed as sensors dedicated to several applications, being particularly interesting at the nanometer scale, since it is largely known that smaller crystallite size enhances sensor's performance. Moreover, these materials are highly appealing as they can be produced by low-cost wet-chemical synthesis routes and are in general nontoxic, earth abundant and low-cost. This manuscript extensively reviews the recent developments of nanostructured semiconductor metal oxide sensors ranging from gas to humidity sensors, including ultraviolet (UV) sensors and biosensors. Zinc oxide (ZnO), titanium dioxide (TiO_2), tungsten trioxide (WO_3), copper oxide (CuO and Cu_2O), tin oxide (SnO and SnO_2), and vanadium oxide (VO_2, V_2O_5)-based sensors either as nanoparticles or as continuous films/layers are described. Their sensing properties are correlated to size, shape, presence of defects, doping elements, amongst other relevant parameters. Different techniques and methods of fabricating these materials are addressed. The review is concluded with novel approaches for functionalization and future perspectives for sensor developments.

Keywords: semiconductor metal oxides; low-cost materials; nanostructures; sensors; sensing properties.

**Corresponding Authors*: Rodrigo Martins and Daniela Nunes, *i3N/CENIMAT*, Department of Materials Science, Faculty of Science and Technology, Universidade NOVA de Lisboa, Campus de Caparica, 2829-516 Caparica, Portugal, Tel: (+351) 212948562, Fax: (+351) 21 294 8558, e-mails: rm@uninova.pt (R. Martins); daniela.gomes@fct.unl.pt (D. Nunes).

Outline

1. Introduction

1.1 Metal oxide nanomaterials

Nanotechnology is compromised as a group of novel technologies capable of designing, producing, characterizing and controlling structures, materials, devices and systems at the nanometer scale, i.e. less than 100 nanometres. This term is very transversal, being used across many fields, such as chemistry, medicine, biology, physics, materials science, environment, engineering, amongst others. The structures or materials at the nanometer scale can be classified as: 0D (zero dimension) if all three spatial dimensions are in the nanometric range, *i.e.* nanoparticles or clusters; 1D (one dimension) if two dimensions are in the nanometric range, like nanotubes, nanorods and nanowires; or 2D (two dimensions) if only one spatial dimension is nanometric, such as in thin films or nanosheets. 3D (three dimensional) materials implies that the 0D, 1D and 2D elements are in close contact forming interfaces, for example compact polycrystals with nanosized grains or 3D porous nanostructures (Figure 1) [1].

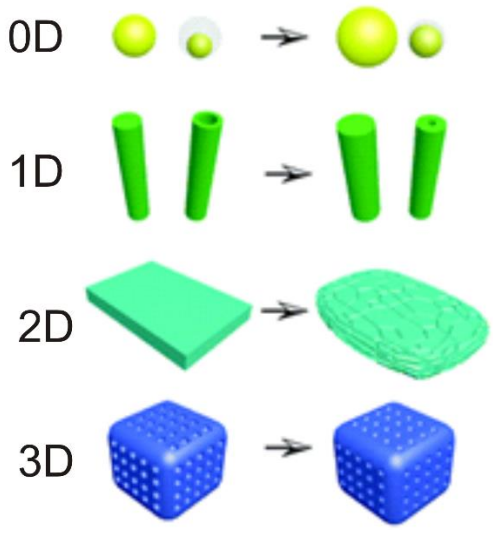

Figure 1. Scheme of the types of nanostructured materials based on their dimensions: 0D, 1D, 2D and 3D [1]. Reproduced with permission of *Royal Society of Chemistry* (2018).

Nanosized materials possess unique and enhanced chemical, physical and mechanical properties when compared to their bulk counterparts due to their high specific surface area and surface-to-volume ratio [2-4]. Generally, the high surface-to-volume ratio of nanomaterials increases as nanoparticle size decreases [5]. Moreover, the size reduction of materials gives rise to quantum confinement phenomena, which modify their intrinsic properties with respect to their corresponding bulk materials [6]. Nanomaterials can occur in several morphologies ranging from nanorods, nanowires, nanowhiskers, nanoflakes, nanocubes, nanopillars, nanospheres, and others [3, 7, 8]. Carbon-based, metal, ceramic, polymeric and metal oxide nanoparticles are well-known classes of nanoparticles [3]. The latter are largely investigated since these are earth abundant, environmentally benign, low cost and, in some cases, chemically stable with suitable electrical and optical characteristics [9-16]. Moreover, these materials display exceptional properties that include mechanical stress tolerance, high optical transparency, high carrier mobilities, wide band gap, high dielectric constant, superconductivity, amongst others [16, 17]. Metal oxides are ionic compounds composed by positive metallic and negative oxygen ions [16], and can exhibit metallic, semiconductor or insulator characteristics [18]. In metal oxides, although the s-shells of positive metallic ions are always fully filled by electrons, their d-shells may not be completely filled [19]. Semiconductor metal oxides can either be classified as *n*-type, in which electrons are the majority charge carriers, or *p*-type, in which the majority charge carriers are holes.

Metal oxide electronic, physical and chemical properties can be engineered by modifying their size, structure, composition, stoichiometry and by doping [4, 20]. Nevertheless, the electronic structure range of these materials is extensive, being divided into two main categories, i.e. transition and non-transition metal oxides, where the latter englobes the pre- and post-transition metal oxides. Transition metal oxides are known to

have small energy difference between a cation d^n and either a d^{n+1} or d^{n-1} configuration, which allows a fast transformation between the different forms, however with unstable structures. Metal oxides with d^0 and d^{10} electronic configurations are characterized as materials with stable properties. The d^0 configuration is found in transition-metal oxides such as, TiO_2, V_2O_5 and WO_3, whereas d^{10} configuration is found in post-transition-metal oxides, as ZnO or SnO_2. Regarding the pre-transition-metal oxides, these are expected to be inert in several applications, since these have large band gaps, electrons and holes are hardly formed [21]. In general, nanoparticles of metal oxides have high density of corner or edge surface sites [22].

Over the years, semiconductor metal oxides have been extensively studied for applications ranging from solar cells [23-26], passing through their integration in electrochromic devices [27-30], lithium-ion batteries [31-33], photocatalyst agents [9, 10, 14, 34-38] and as sensors [39-42]. The interest on the latter application with semiconductor metal oxides has been reported half a century ago and has been increasing along the years due to their practical applications in everyday life, as well as in environmental protection, bio detection, to name just a few. Nowadays, semiconductor metal oxide nanostructures are widely chosen to be integrated in sensors due to their exceptional intrinsic properties associated to their high surface-to-volume ratios, high surface reaction activity, high catalytic efficiency, strong adsorption ability, and electron and phonon confinements [43]. Gas sensors are amongst the most common sensing devices, in which semiconducting metal oxides are frequently used as gas-sensing materials [44]. Another type of sensor where metal oxides are largely present are humidity sensors, which normally determine the amount of water vapor present in a gas that can be a mixture, such as air, or a pure gas, such as nitrogen or argon [45]. UV photosensors/photodetectors are also frequently used in terms of sun/UV exposure, as

well in environmental safety, flame detection, among others [46]. And finally, biosensors that are designed to have a fast response, be low-cost and portable in both clinical and non-clinical applications [47].

1.2 Sensors for different applications

Detection systems for monitoring air and water quality using semiconductor metal oxides are of great interest to improve the selectivity and sensitivity of current sensing devices, and at the same time allowing simultaneous measurements of numerous parameters with real-time response [48]. In the literature, application of metal oxides in gas sensors is vast, with several studies reporting the advantages of integrating these materials in such devices, as well as their gas sensing performance in respect to the size properties [21, 44, 49-52].

The gas sensing technology is largely spread in different industrial fields, but also in domestic environments, some examples are the automotive industry, for indoor air quality control, greenhouse gas monitoring, among others [52]. The most important parameters of gas sensor devices are their sensitivity, operating temperature, selectivity, long-term stability, energy consumption, reversibility, low humidity dependence and finally production cost [44, 52]. Thus, for these devices to be commercially viable, they must be stable during operation, with a uniform and reproducible signal for a prolonged period of time, despite being able to precisely detect a specific gas even in mixtures of different gases. Moreover, the precise control of metal oxide electronic and structural properties, including grain size distribution, local doping, grain boundaries and surface states is mandatory to obtain optimized performance of such devices [53].

Liu *et al.* [52] has classified gas sensors based on their sensing methods in two groups: (a) methods based on variation of electrical properties and (b) methods based on variation of other properties. Semiconductor metal oxide gas sensing relies on the

variation of electrical properties [49]. Gas sensors based on ZnO, TiO_2, SnO/SnO_2, WO_3, CuO/Cu_2O, and V_2O_5 are commonly used to detect combustible, reducing, and oxidizing gases [41, 52, 54-59], and sensing is mainly based on the resistance change responses to the target gases [52]. SnO_2 followed by WO_3 (Figure 2 (a)) are the most commonly used semiconducting metal oxides in commercial gas sensors [60]. In general, reducing gases, such as H_2S, NH_3, CO, H_2, SO_2, CH_4, and HCHO cause an increase of conductivity in *n*-type semiconductors and a decrease in *p*-type semiconductors, while the opposite effect is observed for oxidizing gases (NO, N_2O, NO_2, CO_2, O_3 and Cl_2) [61, 62].

Humidity sensors have been receiving a lot of attention in industrial, medical and even in domestic environments for human comfort. For example, these devices are employed in microelectronic and automobile industries, but also in the pharmaceutical field, food processing, humidity control in hospitals and houses, among other applications [45]. The humidity sensor performance is directly related to the properties of the sensing material including porosity, surface area, pore size distribution and morphology [63]. In similarity to the gas sensors, these devices are expected to have constant response, high sensitivity, fast response time, negligible hysteresis, chemical and physical stability, wide operating humidity range and low cost [64].

There are several humidity evaluation terms, nevertheless the most accepted are absolute and relative humidity (RH), where the latter is normally described. Per million by weight (PPM_w) or volume (PPM_v) and dew/frost point (D/F PT) are subclasses of absolute humidity [45, 65]. Generally, RH is temperature dependent, and can be described by Equation 1 [65]:

$$RH = \frac{P_V}{P_S} \text{x } 100 \qquad (1)$$

where P_V is the actual partial pressure of water vapor present in a gas and P_S is the saturated vapor pressure of the gasat a given temperature. Nowadays, RH sensors are

largely commercialized and can be categorized into three classes, *i.e.* ceramic-based sensors, organic polymer-based sensors, and organic/inorganic hybrid sensors (polymer/ceramic). Ceramic-based sensors can be designed using either semiconducting or dielectric metal oxide materials. Moreover, these sensors are divided into two groups in accordance to their sensing mechanisms, *i.e.* impedance (resistive) or capacitive categories, in which the former uses the conductance, and the latter, the capacitance properties of the sensing layer. Impedance-based sensors are subdivided into ionic-conduction and electronic-conduction. The *p*-*n* heterojunction humidity sensors are also included in ceramic-based sensors [65]. Different approaches have also been suggested, in which an integrated solution having a humidity sensor chip that contains humidity sensors of capacitive type is shown on Figure 2 (b) [66].

Another kind of devices that have recently drawn growing attention are UV sensors/photodetectors, which are interesting for everyday life in terms of sun/UV irradiation exposure, but also for environmental safety, medicine, military defence, flame detection, environmental sensors, space exploration, among others [67, 68]. UV photodetectors detect light in the ultraviolet wavelength ranging from 100 nm to 400 nm.

A high-performance photodetector must have high sensitivity and spectral selectivity, as well as a fast and linear response speed, together with high light transmission and improved chemical and physical stability [69, 70]. The most important parameters of photodetectors are sensitivity, responsivity and external quantum efficiency (EQE) [69]. These parameters are normally used to categorize the UV sensor performance. UV photodetector sensitivity is given by Equation (2) [69], while the responsivity is estimated according to the Equation (3) [13, 71]. The external quantum efficiency, which is defined as the number of electrons detected per light photon, [69, 72] can be obtained by Equation (4).

$$S = \frac{\Delta I}{I_{dark}} \text{x } 100 \quad (2)$$

$$R = \frac{\Delta I}{P_{UV}} \quad (3)$$

$$EQE = \frac{hc}{e\lambda} . \frac{I_{ph} - I_{dark}}{P_{UV}} \quad (4)$$

where ΔI is the difference between the photocurrent and the dark current, I_{dark} is the dark current, and P_{UV} is the UV light power, h is Planck's constant, c is the speed of light in vacuum, e is the electron charge, and λ is the exciting wavelength. Several photodetectors types have been reported, including photoconductors, metal-semiconductor-metal (MSM) photodetectors, Schottky photodiodes and *p-n* junction photodiodes. A photoconductor is composed by a semiconductor material with two ohmic contacts, forming a radiation-sensitive resistor. MSM photodiodes are based on two back-to-back Schottky diodes and using an interdigitated electrode configuration on top of the active layer. Schottky diodes consist of a metal layer that contacts a semiconductor material, and the metal/semiconductor junctions exhibit rectifying behaviour. *p-n* junction photodiodes are based on a heterojunction of a *p*- and *n*- type materials, without the requirement of a reverse bias and displaying improved noise performance [73]. The *p-i-n* has an intrinsic layer and provides additional sensitivity and performance over that of the basic *p-n* junction photodiode due to the reveres bias operation. Nevertheless, innovative approaches to extract the best photodetector performance, more recently with nanostructured metal oxides, are under constant development (Figure 2 (c)).

Metal oxide nanostructures are also widely present in biosensors. A biosensor is described as a sensing device that combines a transducer for signal detection with a biologically sensitive and selective component, *i.e.* bioreceptor (antibody, enzyme, receptor protein, nucleic acid, whole cell or tissue section). Typically enzymes are used as bio component, and they are large protein molecules that act as a catalyst in chemical

reactions, remaining unchanged during the process [74]. Upon interaction of a target molecule with the bio component, a signal is generated and detected by the transducer (Figure 2 (d) [75]). It is possible to occur optical or electrical signals [76]. This signal is proportional to the concentration of the component. The target molecules/analytes can be proteins, DNA, glucose, cholesterol, toxins, hormones, bacteria, among others [77]. These devices are considered a powerful analytical tool in medical diagnostics with the fast and precise detection of diseases, virus , food quality and safety, fermentation industry, in metabolic engineering and other areas [47, 78]. The device is expected to be highly accurate, homogeneous and reproducible, despite having optimized response time, high stability, sensitivity, specificity, selectivity (low interference) and bioactivity [76, 79].

There are many types of biosensors, in which these are mainly classified according to bioreceptors and transducers. The most common are immunosensors, calorimetric, DNA, enzyme-based, tissue-based, optical, thermal, optical, piezoelectric and electrochemical biosensors, in which the latter is subdivided in conductimetric, amperometric and potentiometric sensors [74, 78]. The most successful commercial biosensor is the amperometric glucose biosensor, with which diabetic patients are able to periodically monitor blood glucose levels [74]. Nevertheless, the full integration of metal oxides nanostructures in biosensors still raises questions regarding the maintenance of their bioactivity for extended periods of time and their toxicity.

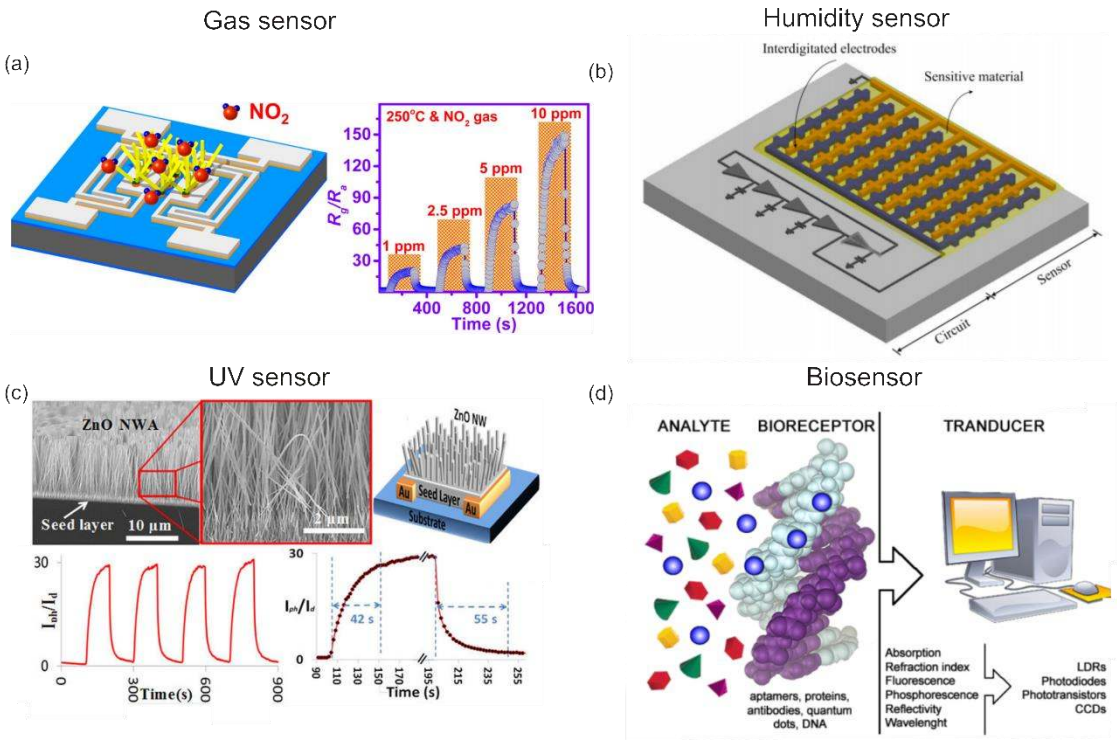

Figure 2. (a) Gas sensor and its respectively gas sensing characteristics for NO_2 [80], (b) integrated humidity sensor [66], (c) photoresponse characteristics of a UV photodetector [81] and (d) biosensor detection process [75]. Reproduced with permission of *Elsevier* [80], *MDPI* [66], *Springer Nature* [81], and *Intech* (2018) [75].

1.3 Sensing mechanisms

The mechanisms responsible for gas, humidity and UV responses have similar concepts. Despite being a controversial topic, the mostly accepted mechanism for these sensors is resultant of a change in electrical conductivity or resistivity of the semiconductor metal oxide materials [82, 83]. In the case of gas sensors, the gas sensing is resultant of a shift on equilibrium of the surface chemisorbed oxygen reaction due to the presence of a target gas, creating extrinsic surface acceptor states that immobilize conduction band electrons from the near-surface region of an *n*-type semiconductor material. For *p*-type semiconductor materials, the chemisorption of oxygen leads to an accumulation surface layer which alters their conductance [44, 61]. Under ambient conditions, the oxygen molecules are adsorbed on surface of the *n*-type

semiconductor materials and can capture inner free electrons from of these materials. The negative charge trapped in these oxygen species causes a depletion layer near the surface, which results in the reduction of the conduction layer [$O_{2(g)} + e^- \rightarrow O_{2^-(ads)}$] [71, 82]. When the sensor is exposed to reducing or oxidizing gases, this will affect the density of charge carriers (*n*-type electrons or *p*-type holes) in the near-surface region of each grain. Reducing gas molecules will remove surface-bound oxygen atoms, releasing immobilised electrons, whereas oxidising gases immobilise conduction-band electrons from the near-surface region by creating additional surface-acceptor states. Thus, the gas molecules will result in the decrease or increase of the depletion layer thickness by changing the surface-state density, which in consequence leads to a change in the materials' conductance [44].

In summary, upon interaction with oxidizing gases, the gas species will act as acceptors, which will lead to a resistance increase for *n*-type semiconductor metal oxides. When the oxidizing gases are adsorbed on *n*-type material surface, it will gain electrons from the adsorbed oxygen, which will increase the depletion region, and thus decrease its conductivity [39]. The opposite behaviour is observed for *p*-type metal oxide materials. Figure 3 (a) shows the negative surface charge causing the upward band bending of conduction (E_C) and valence (E_v) bands, the electron depleted region (space-charge layer), the average thickness, *i.e.* the depth of band bending region (q.Vs), and the effective surface potential barrier (eV*)*. The depth and height (eV*)* of the band bending depend on the overall surface charge present (amount and type of adsorbed oxygen). In Figure 3 (b), it is represented the grain boundary structures and corresponding band models showing the electron conduction mechanism. In polycrystalline sensing materials, the electronic conductivity occurs through the percolation paths along grain-to-grain contacts depending on the value of potential barrier (eV*)* or Schottky barrier of the surrounding grains. Upon gas exposure, the Schottky barrier between two grains is

lowered facilitating the electronic conduction in sensing layers through different grains via grain to grain percolation path [84].

In fact, the gas adsorption on the surface and the change in the resistance of metal oxide semiconductors are quite complex processes. It has been accepted that the sensor resistance is a function of the gas partial pressure, following a power-law response, in which the power-law exponent is specific to the gas and temperature used [85-87]. Several studies have extensively discussed the processes, including when using metal oxide nanostructures. In the case of metal oxide nanowires, the conductivity for *n*- and *p*-type materials, Equations 6 and 7, respectively, can be described as [88, 89]:

$$G_n = \frac{\sigma_d}{\ell}\pi\left(\frac{D}{2} - L_{D_n}\right)^2 = N_d q \mu_n \frac{\pi(D-2L_{D_n})^2}{4\ell} \quad (6)$$

$$G_p = \frac{\sigma_a}{\ell}\pi\left(\left(\frac{D}{2}\right)^2 - \left(\frac{D}{2} - L_{D_p}\right)^2\right) = N_a q \mu_p \frac{\pi(DL_{D_p} - L^2{}_{D_p})}{\ell} \quad (7)$$

where $\sigma = q\mu N$ is the conductivity of the nanowire; D is its diameter; ℓ is the length; N is the carrier concentration; μ is the carrier mobility; q is the carrier charge; and L_{Dn} and L_{Dp} are the thicknesses of the depletion and accumulation layers, respectively.

The gas-sensing response for *n*-type (Equation 8, (S_{OX}^n)) and *p*-type (Equation 9, (S_{OX}^p)) semiconducting metal oxide to an oxidizing gas can be defined as [62]:

$$S_{OX}^n = \frac{R_{og}}{R_a} \quad (8)$$

$$S_{OX}^p = \frac{R_a}{R_{og}} \quad (9)$$

where R_{og} and R_a are the sensor electrical resistances measured with an oxidizing gas and pure dry air, respectively.

In the case of reducing gases, the gas species act as donors, *i.e.* electrons will be injected into *n*-type material surface, reducing the depletion region and releasing the band bending, and this will lead to a resistance decrease in the case of *n*-type materials and

increase for *p*-type materials [39, 61]. The gas-sensing response for *n*-type (Equation 10, (S_{rd}^{n})) and *p*-type (Equation 11, (S_{rd}^{p})) semiconducting metal oxide to a reducing gas is normally represented as [62]:

$$S_{rd}^{n} = \frac{R_a}{R_{rg}} \quad (10)$$

$$S_{rd}^{p} = \frac{R_{rg}}{R_a} \quad (11)$$

where R_{rg} and R_a are the sensor electrical resistances measured with an reducing gas and pure dry air, respectively.

Mechanisms of water vapor adsorption on metal oxide surfaces have been well studied [45, 90, 91], and it is known that most metal oxides have adsorbed hydroxyl groups on their surface which influences the surface phenomena, including the response of a sensor to the detected gas [92]. In general, water molecules can be adsorbed by an acid-base type dissociative chemisorption followed by hydrogen bonded physisorption, however some oxides can also chemisorb water vapor through redox reactions involving electron transfer to the metal oxide [63, 92]. Moreover, water molecules have been reported to increase the conductivity of *n*-type semiconductor metal oxides and to decrease the conductivity of *p*-type semiconductor metal oxides, in which this effect was related to the donation of electrons from the chemically adsorbed water molecules to the oxide surface [67, 91].

The mechanism of all the ceramic humidity sensors, of ionic and electronic conduction (resistive) types and capacitive, depends on the superficial water vapour adsorption, which is based on chemical and physical adsorptions and capillary condensation processes. Resistivity-type humidity sensors measure the electrical resistance in response to humidity. Most of the available humidity sensors utilize the ionic type humidity-sensing mechanism. In ionic sensing devices, when the ceramic surfaces adsorb water, their electrical properties change, and by increasing the humidity, the

conductivity increases and thus the dielectric constant increases [65, 93]. On the other hand, capacitive-type humidity sensor mechanism relies on electrical permittivity that is sensitive to humidity variation, and the electrical response is linked to water adsorption-desorption processes on the exposed surface of the sensing material [94].

The UV sensing process occurs when the semiconductor metal oxide with oxygen molecules adsorbed on its surface and without any UV irradiation, can capture free electrons present in the *n*-type semiconductor and form a low conductivity depletion layer in the near-surface region. When exposed to UV irradiation at a photon energy above the materials' band gap, electron-hole pairs are photogenerated [$hv \rightarrow e^{-} + h^{+}$], and the holes migrate to the surface along the potential slope. This potential slope is produced by band bending and discharge of negatively charged adsorbed oxygen ions through surface electron-hole recombination, leading to oxygen photo desorption [95] [$h^{+} + O_{2}^{-}{}_{(ads)} \rightarrow O_{2(g)}$] (Figures 3 (c) and (d)). This hole-trapping mechanism through oxygen adsorption and desorption enhances the high density of trap states due to the dangling bonds at the surface and thus enhances the photoresponse [96]. The stability and performance of UV sensors are highly influenced by the surrounding environment. Several studies reported that the photodetection of metal oxide nanostructured sensors is strongly dependent on the ambient gas conditions, with significant differences regarding measurements in air, vacuum or inert gases [97-99].

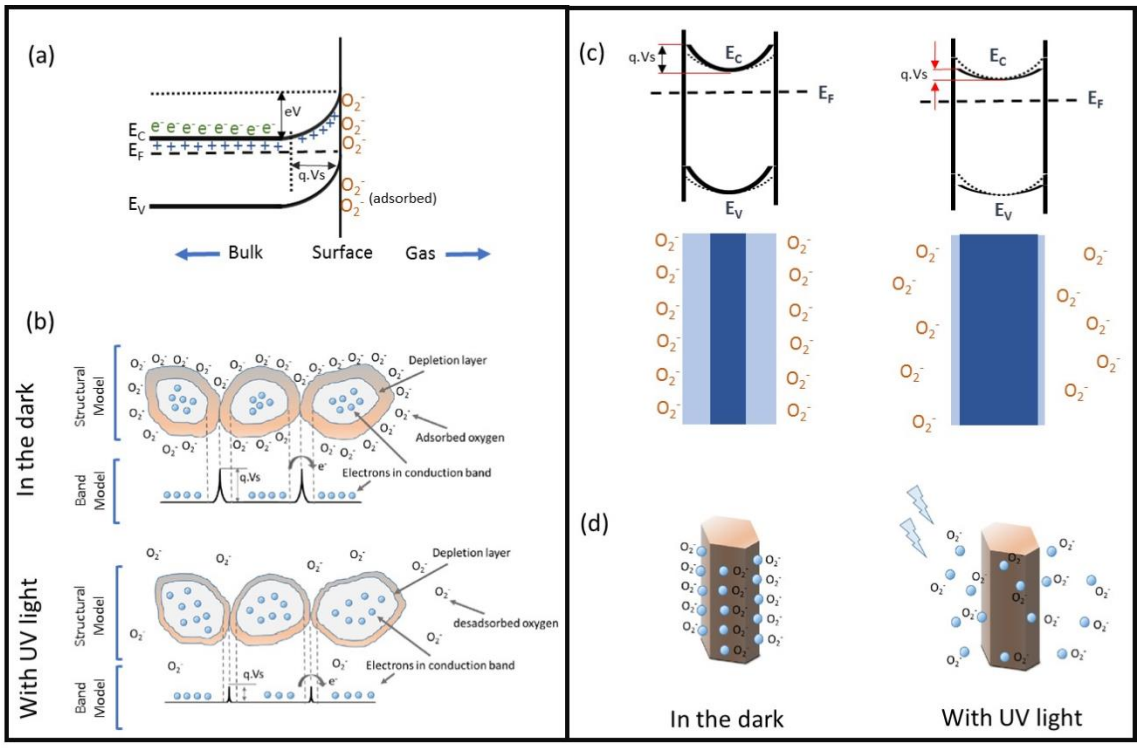

Figure 3. (a) Scheme of the band bending in a wide band gap semiconductor after chemisorption of charged species on surface sites (E_C and E_V are the conduction and valence band energies in the grain bulk, respectively, E_F is the Fermi level, e^- is the conducting electrons and $^+$ the donor positions [49, 85]. (b) Schemes of the structural and band models of a *n*-type semiconductor, and (c) and (b) dark and UV irradiation processes [71, 88]. Reproduced with permission *MDPI* [71], and *Elsevier* [49], [85] and [88] (2018).

Regarding biosensors, as previously described, the devices combine a biological element with a transducer to detect specific target analytes and thus produce quantifiable and processable signals [47, 77, 100]. Generally, the measurement of electrical properties in biological systems is from electrochemical nature, in which the bioelectrochemical element will act as the main transduction element. Moreover, for electrochemical detection, enzymes are mostly used, due to their specific binding capabilities and biocatalytic activity. Antibodies, antibody fragments or antigens are usually used in immunosensor to monitor binding events in bioelectrochemical reactions [100]. These electrochemical detection techniques can generate a measurable current (*amperometric*),

a measurable potential or charge accumulation (*potentiometric*), or change in the medium conductive properties between electrodes (*conductometric*), but also measurements as function of impedance, both resistance and reactance (*impedimetric)*, and using transistor technology (*field-effect*) to measure current as a result of a potentiometric effect at a gate electrode [100].

Recently, metal oxide materials have been integrated in novel biosensing devices, since they exhibit enhanced electron-transfer kinetics and strong adsorption capability. These properties guarantee appropriate microenvironments for the immobilization of bio molecules and result in enhanced electron transfer and improved biosensing characteristics. The biosensing process involving metal oxide materials relies on the biomolecules binding to these materials via physical adsorption or chemical binding. Physical adsorption of a biomolecule depends on several parameters such as surface morphology, reaction medium and net surface charge, especially when it arises due to weak interactions, such as van der Waals, electrostatic and physisorption. Nevertheless, short-range forces including charge, steric, depletion and solvent interactions can also affect the biointerface. An effective biointerface with metal oxide materials guarantees an enhanced electron transfer rate and assists the biomolecule to maintain a stable biological activity [47]. It has also been reported that adding metal oxides to unlike surfaces can increase the adhesion of negatively-charged bacteria due to their positive charge and hydrophobicity, this is of particular importance for producing high performance biosensing devices [101].

This review will address the two main types of nanostructured semiconducting metal oxide sensors including *n*-type, *i.e.* zinc oxide, titanium dioxide, tungsten oxide, tin dioxide, and vanadium oxides, but also materials displaying *p*-type characteristics, *i.e*. copper oxides and tin monoxide. Their sensing properties, production techniques and

methods will be discussed from an application-oriented perspective. An overview on different sensors such as gas, humidity, UV and biosensors having these nanomaterials integrated will also be presented.

2. Semiconductor metal oxide nanostructures

Semiconductor metal oxides have been largely employed in electronics and opto-electronics with their incorporation on transistors, circuits, or panel displays, and more recently on printed and paper electronics [102-104]. Nevertheless, the sensing technology has evolved over the last years and continues to grow to guarantee human well-being, quality and safety from food to air, but also for environmental protection. ZnO, TiO_2, WO_3, CuO/Cu_2O, SnO/SnO_2 and VO_2/V_2O_5 are examples of such materials and have been integrated in several kinds of sensors, *e.g.* gas, humidity, UV and biological sensors. These materials can adopt the most distinct structures at the nanoscale, ranging from nanowires to nanospheres or nanosheets, which will directly influence their performance in the final sensing applications.

2.1 Zinc oxide

Zinc oxide has been extensively studied since 1935 due to its integration in several applications with special interest in ZnO-based electronic and optoelectronic devices. ZnO is an *n*-type semiconductor with a wide band gap of 3.2-3.4 eV and a large exciton binding energy of 60 meV at room temperature [105]. At room temperature and pressure, ZnO crystallizes in the hexagonal *wurtzite* structure in which each anion is surrounded by four cations at the corner of a tetrahedron [105]. Other structures may appear like "*zinc blend*" (the term is originated from compounds like ZnS that can present cubic or hexagonal phases) and "*rocksalt*" (with a cubic phase) but, under ambient conditions they are not thermodynamically stable phases. Hexagonal ZnO *wurtzite* structure has a unit cell with lattice constants a= 0.3296 nm and c= 0.52065 nm [106] and ratio c/a = 1.602,

corresponding to *P6₃mc* space group [105, 107]. This ZnO space group is characterized by presenting two interconnecting sublattices of Zn^{2+} and O^{2-} ions in which each zinc ion is surrounded by a tetrahedral of four oxygen ions [105]. The zinc and oxygen ions are arranged alternatively along the *c*-axis and exhibit positive and negative polar plane rich in Zn^{2+} and O^{2-}, respectively. This Zn^{2+} and O^{2-} tetrahedral coordination is the origin of a polar symmetry along the hexagonal axis [105, 108]. This asymmetry along the *c*-axis is responsible by an anisotropic growth of 1D ZnO crystallites. The most common and stable ZnO crystal exhibit a *wurtzite* structure with four face terminations – the polar Zn terminated (0001) and O terminated $(000\bar{1})$ facets, and the non-polar $(10\bar{1}0)$ facets, containing equal number of Zn and O atoms [14, 105, 108-110]. Figure 4, shows a schematic representation of the ZnO hexagonal *wurtzite* structure facets and an atomic model of the polar and non-polar facets.

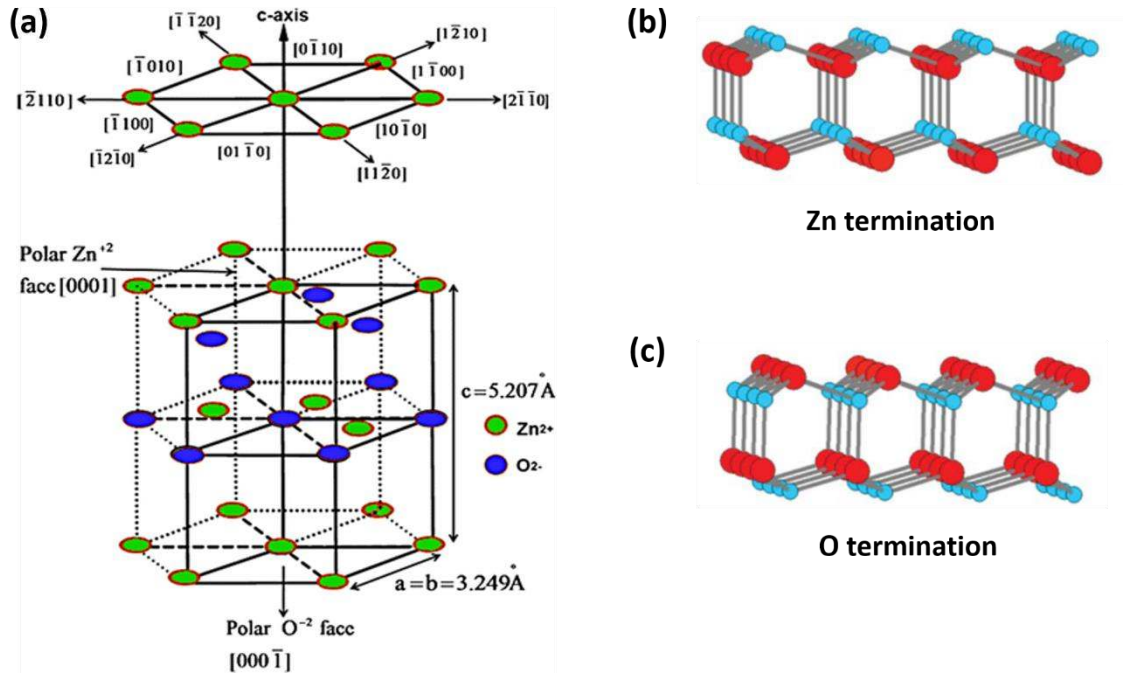

Figure 4. (a) Schematic of the unit cell of the ZnO hexagonal wurtzite structure and the correspondent ionic position of Zn^{2+} and O^{2-} [107]; (b) and (c) Side view of ZnO *wurtzite* facets with (0001) Zn and $(000\bar{1})$ O termination, respectively [111]. Reproduced with permission of *Springer Nature* [107] and the *Royal Society of Chemistry* (2018) [111].

It is well known that polar facets possess different chemical and physical properties from non-polar facets, and that O terminated polar facets also present a slightly different electronic structure [105]. These characteristics are responsible for the vast properties presented by ZnO such as piezoelectricity and spontaneous polarization, being a key factor in crystal growth and in defect generation [105].

When used in gas sensing or in other applications, it has been found that the polar Zn terminated (0001) facets are more active than polar O terminated ($000\bar{1}$) and the non-polar ($10\bar{1}0$) facets due to the abundance of OH^- that adheres to low-coordinated Zn sites, forming highly active ·OH radicals [111, 112].

The growth of different ZnO nanostructures has been reported by several authors in the past few years. Different synthesis methods can be employed to produce ZnO nanostructures, such as chemical bath deposition, electrospinning, electrodeposition, laser assisted flow deposition (LAFD) and also hydrothermal/solvothermal synthesis, either by conventional or by microwave assisted heating [13, 14, 113-123]. Depending on the synthesis method, precursors used and their concentration, solution pH or even the solvents selected, zinc oxide may present different nanostructures ranging from nanorods, nanofibers, nanoneedles, nanowires, nanoplates, nanostars, tetrapods to nanoflowers [14, 108, 113, 124-127], as shown in Figure 5.

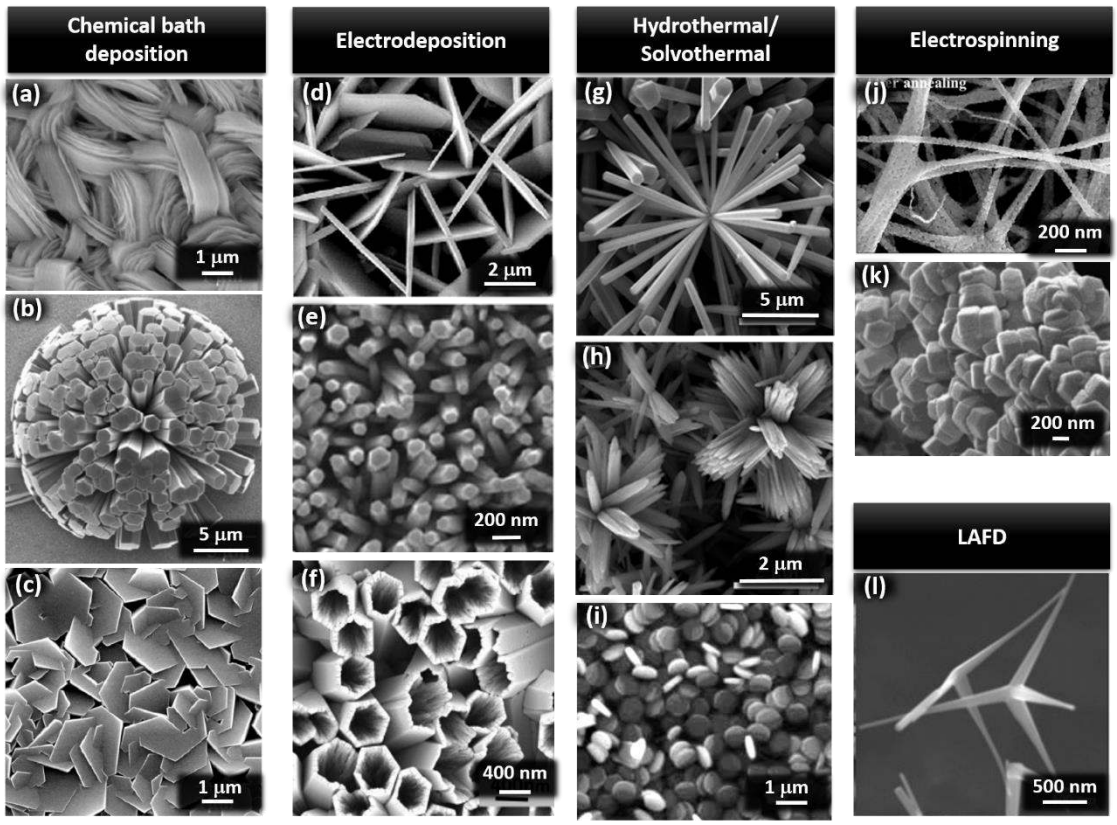

Figure 5. Different ZnO morphologies produced by different synthesis techniques: (a), (b) and (c) chemical bath deposition [113]; (d), (e) and (f) electrodeposition [123, 128, 129]; (g), (h) and (i) hydrothermal/solvothermal synthesis [112, 130]; (j) and (k) electrospinning [116, 117] and (l) laser assisted flow deposition [121]. Reproduced with permission of *Elsevier* [112, 113, 116-118, 121, 123, 128, 129] and *Royal Society of Chemistry* (2018) [130].

Zinc oxide is an inexpensive and earth abundant material, nontoxic and chemically stable, which makes it suitable to be used in several applications, such as field effect transistors [131-134], solar cells [121, 135-137], piezoelectric generators [138-140], photocatalysis [14, 141, 142], as a platform for SERS applications [143, 144] and in sensors [13, 71, 122, 145].

Metal oxides semiconductors are commonly used as gas sensors in environmental monitoring and in industrial applications allowing the production of low cost and small devices [146]. ZnO is capable to detect a great variety of different gases, such as CO_2, H_2S, NO_2, NO, NH_3, C_3H_8 and CH_4 [146-150]. The detection of carbon dioxide is of vital

importance for human life. The use of inexpensive and highly sensitive miniaturized sensors are of great interest for environmental control of indoor air quality and pollution (considering the impact of CO_2 emissions on the global warming) [147].

The most recent studies are focused on devices miniaturization allied to increased sensitivity. So, many authors are studying the influence of ZnO morphology on gas detection since just by changing its shape it is possible to enhance sensor performance, opening new ways to produce more selective gas sensors [150]. Gupta *et al.* [146] studied the sensitivity of different ZnO nanostructures, nanowires, nanobelts and tetrapods in the detection of H_2S and NO. Gupta found that sensors based on ZnO nanobelts were more sensitive to NO gas, and that ZnO tetrapods were more sensitive in detecting H_2S gas while ZnO nanowires had no response in detecting NO, H_2S, NH_3, CO and CH_4. The high sensitivity of nanobelts to these gases may be due to their low thickness (< 20 nm) when compared to the nanowire's diameter (≈ 100 nm), thus presenting a larger surface to volume ratio. It was found that the response mechanism to detect H_2S arises from changes in the grain boundary resistance, while for the detection of NO it arises from changes in the grain boundary and intragrain resistances [146].

Jonca *et al.* [150] studied the use of cloudy-like, isotropic and nanorods ZnO nanostructures for detection of CO, NH_3 and C_3H_8 gases. The ZnO nanorods nanostructures presented higher sensitivity to the detection of this type of gases.

Nitrogen oxide gases like NO and NO_2 are environmentally harmful gases formed during the combustion in automotive and factories and are frequently associated to greenhouse gas effect [149]. NO_2 is a very strong oxidizing gas, so the reaction takes place directly with the ZnO surface and not with the oxygen chemisorbed at the surface. NO_2 molecules will then consume conduction electrons, increasing the depletion region at the surface, thus reducing ZnO conductivity [151]. Several authors have studied the

use of different ZnO nanostructures for detection of NO and NO_2 gases. Sadek *et al.* [151] used ZnO nanobelts to detect NO_2 gas with concentration as low as 0.51 ppm. Cho *et al.* [152] used ZnO nanorods and was able to detect NO_2 gas concentrations of 1 ppm. Figure 6 shows several gas sensors produced with nanostructured ZnO sensitive layers.

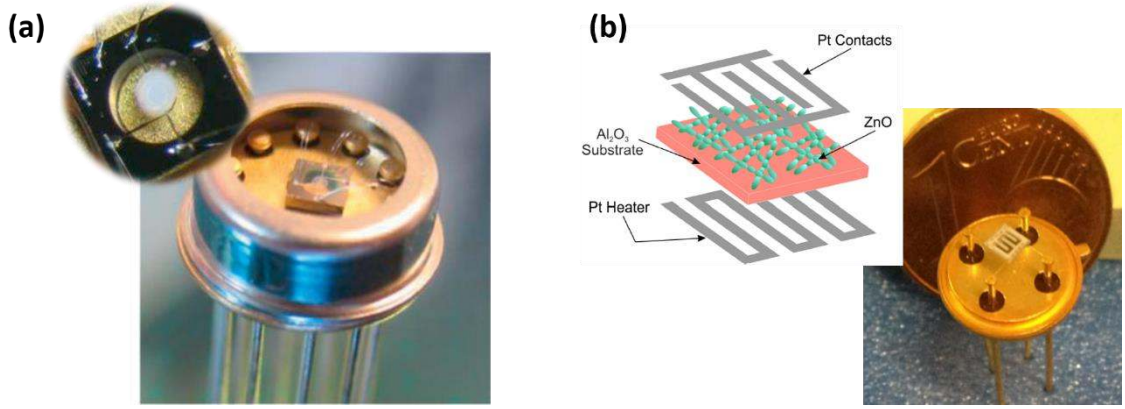

Figure 6. (a) Miniaturized gas sensor with a ZnO sensitive layer for the detection of CO, NH_3 and C_3H_8 gases [150]; (b) Schematic and digital image of a ZnO based sensor for the detection of NO_2, H_2 and CH_4 gases [153]. Reproduced with permission of *Elsevier* (2018) [150] and [153].

Another way to improve ZnO gas sensor performance is by doping the semiconductor metal oxide with other materials. Dilonardo *et al.* [154] doped ZnO nanostructures with Au nanoparticles and was able to detect NO_2 gas at 0.2 ppm concentration , presenting a total recovery time of 30 seconds after removing the gas. Moreover, Li *et al.* [155] used ZnO/NiO nanoheterojunction with porous morphology to detect ethanol. Li was able to detect 100 ppm of ethanol at 200 °C. By using a heterojunction the sensing mechanism may be a result of two factors. ZnO is a *n*-type semiconductor and in the presence of ethanol interaction with O^{2-}, O^- at the crystal surface will occur, leading to an increase of conductivity. On the other hand, NiO is a *p*-type semiconductor as such, the reductive ethanol molecules will react with oxygen ions adsorbed at the NiO surface and release electrons that will recombine with holes in *p*-type NiO, leading to a decrease in holes concentration and, consequently to a resistance

increase [155]. Ethanol molecules may also combine with holes in NiO nanostructures and produce intermediates CH_3CHO molecules which will react with the absorbed oxygen, resulting in increased sensitivity ethanol for this type of heterojunction [155]. Moreover, it has been reported that in the heterostructure sensor, electrons will be transferred from *n*-type ZnO to *p*-type NiO, while holes are transferred in the opposite way until the system reaches equilibrium at the Fermi level. This will lead to the formation of the hole depletion layer and increase the amount of chemisorbed oxygen species. The increase of such species allows more surface chemisorbed oxygen species to participate in the oxidation-reduction reactions at the sensing material's surface and thus impose an enhanced change in sensor resistance [155, 156].

The control of humidity levels is of great importance in some environments, such as in clean rooms, food management, medical area and chemical substances storage [157]. When using ZnO nanostructures, it is expected that the impedance of the sensor increases with the increase of adsorbed water at the sensor's surface and that sensors present low hysteresis, high sensitivity with a short recovery time. Some researchers have studied the use of ZnO nanostructures in humidity sensing applications.

Ghanem *et al.* [157] produced a humidity ZnO sensor that presented a resistivity variation in the presence of humidity changing between 15-95 %, with hysteresis error of 2 % at 100 °C. Also, Herrán *et al.*[158] used ZnO nanoparticles to monitor humidity at room temperature. With a response time of 5 seconds, Herrán was able to measure humidity in the range of 0 to 80 %.

Also, in the case of humidity sensors, it is possible to improve sensor properties by synthesizing a composite nanostructured material. Sin *et al.* [159] produced humidity sensors based on ZnO/SnO_2 cubic structures. The advantages of using a composite sensor are higher thermal stability and increased electron mobility. When using a ZnO/SiO_2

cubic structure, Sin was able to obtain sensitivity of 22.5 at 90 RH%, a much higher value when compared to the sensitive values of 7.5 and 2.3, obtained with only ZnO or SnO_2, respectively [159]. The same ZnO/SiO_2 composite was used by Qing *et al*. [160]. The mesoporous ZnO/SiO_2 produced by Qing presented a high surface area, with uniform structured pores that enhanced water vapour adsorption at the surface, enhancing sensitivity. The produced sensor presented improved humidity sensing in a range of 11 to 95 RH%, with a response time of 50 seconds and maximum humidity hysteresis of 2 % [160].

Leilei *et al*. [161] have reported the use of a ZnO/TiO_2 composite for humidity detection . The main disadvantage of using ZnO in humidity sensors is the fact that this semiconductor material can be very hydrophobic, which difficults sensitivity improvement . On the other hand, TiO_2 is a hydrophilic material due to the observed dissociative adsorption of water at Ti^{3+} defects sites. Nevertheless, the use of this material may bring some disadvantages, such as high resistance, pronounced hysteresis and short long-time stability [161-163]. So, the use of a ZnO/TiO_2 composite as complementary materials will favour the enhancement of humidity sensor properties. The ZnO/TiO_2 nanorods composite produced by Leilei *et al.* [161] presented a considerable sensitivity enhancement when compared with single ZnO or TiO_2 sensors, with an enhancement of 31 and 1380, respectively. The use of a TiO_2 coating will enhance the water adsorption at the sensor's surface, due to the rough surface of TiO_2 and its remarkable hydrophilicity. Moreover, with the increase of humidity, capillary condensation will occur in the pores with smaller radius than the Kelvin critical radius (TiO_2 surface and ZnO/TiO_2 interface). The formation of these pores is due to the nanoscale grain boundaries of the TiO_2 shell. The introduction of this shell leads to the adsorption of more water molecules by increasing the hydrophilicity of the surface area and by inducing capillary condensation.

The phenomenon will contribute to the polarization of adsorbed water molecules and induce accelerated capacitance response [161].

Figure 7, shows the adsorption model proposed by Leilei *et al.* [161].

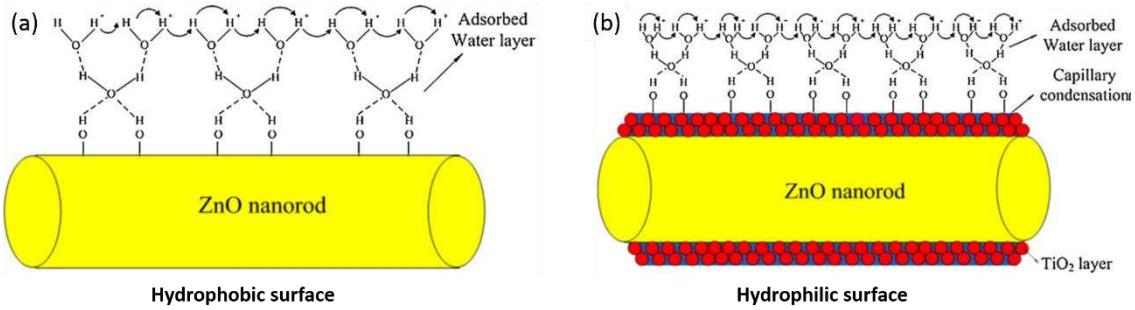

Figure 7. Humidity adsorption models for (a) ZnO nanorods; (b) ZnO/TiO_2 composite nanorods [161]. Reproduced with permission of *Elsevier* (2018).

The UV photoresponse of ZnO material was first observed by Mollow in the 1950s [164]. Since then, zinc oxide has been one of the most studied metal oxide material used in UV sensor applications. Initially, researchers had focused their attention on the development of ZnO thin films-based sensors however these films presented some intrinsic drawbacks, such as a slow response time and recovery speed. So in the past decade, many authors have reported the use of ZnO nanostructures (like nanorods, nanostars and tetrapods) with the aim of increasing the photoresponse by increasing the sensor surface area [114, 165-170]. Due to the fact that ZnO photoresponse is related to adsorption and desorption of chemisorbed oxygen from (0001) polar facets, the use of 1D nanostructures presents some advantages due to its large surface to volume ratio, allowing increase of the sensor's photoresponse and/or reduction of the active area (very important for devices miniaturization) [164, 166].

Many are the factors that can influence the sensitivity of a ZnO UV sensor including substrate, ZnO particles morphology or even sensor configuration. Alenezi *et al.* [81] developed a series of flexible sensors with different configurations that presented distinct values of photocurrent response. With a bridging nanosizing configuration,

Alenezi *et al.* [81] were able to improve sensitivity, with an ultrafast response time (90 ms) and also a fast recovery time (210 ms). Pimentel *et. al.* reported a set of studies demonstrating the production of ZnO UV sensors constructed on rigid or flexibles substrates (glass or PET/PEN) and also on cellulosic based substrates [13, 71, 122]. Figure 8 shows ZnO UV sensors produced on cellulosic based substrates and glass.

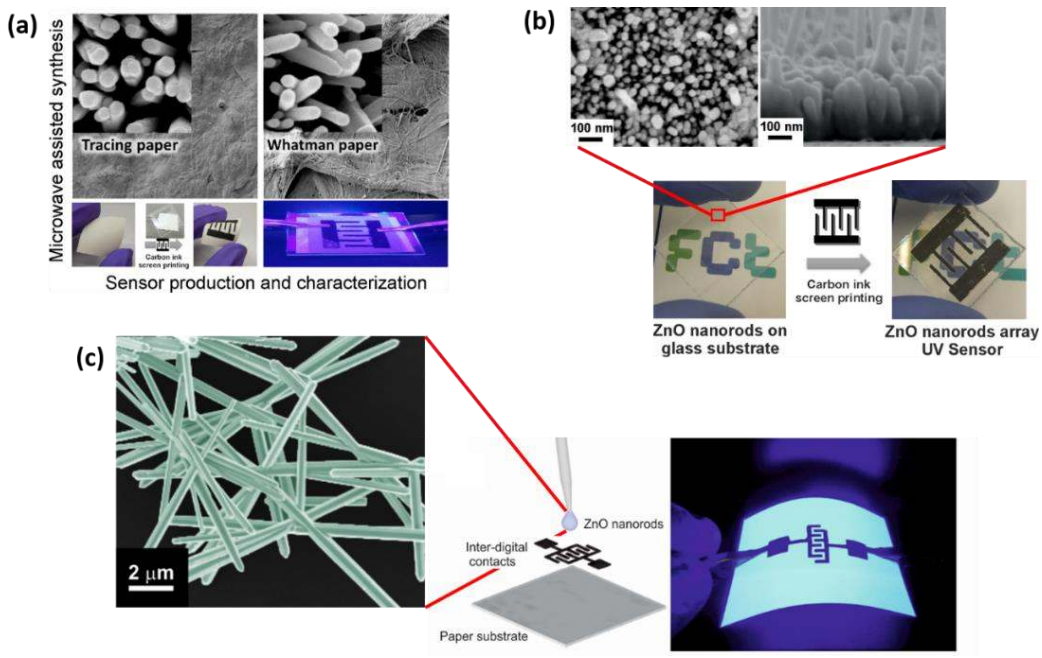

Figure 8. (a) ZnO UV sensor produced on tracing and Whatman paper [13]; (b) Transparent UV sensor produced on glass substrate [71]; (c) UV sensor produced with ZnO nanowires on top of graphite electrodes, screen printed on paper substrate [122]. Reproduced with permission of *MDPI* [13] and [71], and *ACS publications "Copyright (2018) American Chemical Society"* [122].

A disadvantage of using ZnO nanostructures in UV sensing is the low photocurrent value, mainly due the small size of individual nanowires. Some different methodologies are being employed by researches in order to enhance the photoresponse of ZnO UV sensors. Bai *et al.* [171] showed the difference in using ZnO nanowires aligned horizontally along the substrate or using the same nanowires placed vertically against the substrate. By a transfer process, it was possible to transfer the vertically oriented nanowires into a well aligned horizontal orientation and this way increasing the

photoresponse current from 1.8 μA to 12.22 mA, with an on/off current ratios of 82000 [171].

One of the most important characteristics that are being studied by scientific community is sensor miniaturization. Portable and small photodetectors have a wide range of applications, such as the monitoring of UV dosage for skin cancer prevention, optical communications and also in astronomy [172]. Nasiri *et al.* [172] produced small ZnO photodetectors with excellent selectivity and milliampere photocurrents. A spray flame synthesis technique was used (see Figure 9 (a)), producing ZnO nanoparticles with a diameter of ≈ 19 nm. The high sensitivity of this sensor is mainly due to the highly pure crystal surface and the very small particle size that originated ultra-porous ZnO nanoparticle film, presenting increased photocurrent from 260 μA to 1.2 mA [172].

Another very interesting concept for UV sensor application is presented by Park *et al.* [164]. Park was able to produce a wireless UV sensor platform based on ZnO nanorods where real-time collected signals are sent to a smartphone through Bluetooth connection, with responsivity as high as 0.55 A W^{-1}, response time of 3.1 s and recovery time of 1.25 s. Figure 9 (b) shows a photograph of the photocurrent measurement by a smartphone.

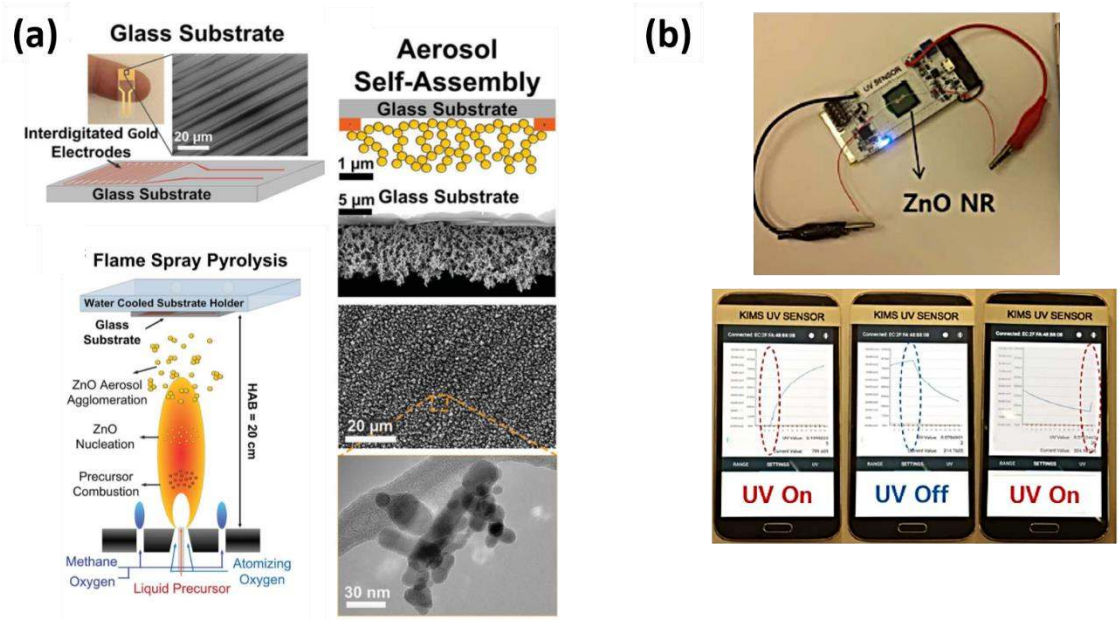

Figure 9. (a) Schematic of a ZnO photodetector production by flame spray pyrolysis [172]; (b) Photographic image of a ZnO UV sensor Bluetooth-connected to a smartphone [164], where it is visible the photocurrent variation under on/off cycles of UV radiation. Reproduced with permission of *John Wiley and Sons* [172] and *Royal Society of Chemistry* (2018) [164].

The most recent approach in ZnO UV sensors is the use of graphene as conductive layer to improve their performance [173-175]. The advantage of using graphene relies on its superior conductivity (that prevents recombination of electron-hole pairs in the ZnO/graphene composite) and transmittance (over 97.7 % for a single layer graphene, which maximizes UV-light absorption), allowing a reduction in response and recovery time, and increasing the photocurrent gain [174]. Duan *et al.* [174] was able to produce a ZnO UV sensor with responsivity of 0.039 A W^{-1}, extremely short response and decay time of 37 µs and 330 µs, respectively.

Zinc oxide is a biocompatible material, with high isoelectric point ($IEP_{ZnO} \approx 9.5$), high surface activity and electron communication feature [176, 177]. For these reasons, ZnO can be functionalized with a wide range of biological materials with low IEP values, through electrostatic interaction, such as enzymes (like glucose oxidase and cholesterol

oxidase), antibodies or even DNA [176, 178, 179]. Several reports have demonstrated the application of ZnO as biosensors, *i.e.* in DNA immobilization [180], in glucose level detection [176, 177, 181], for cardiac biomarker detection [179, 182, 183] and also for cancer diagnostic [178, 184, 185].

Probably the application of ZnO for glucose detection is one of the most studied biosensors. For glucose levels detection , ZnO biosensors are produced by immobilization of glucose oxidase enzyme onto ZnO nanostructures [176]. The high IEP_{ZnO} value will promote the formation of zinc oxide/ glucose oxidase complexes during functionalization (glucose oxidase are negatively charged molecules, that will be readily attracted and immobilized onto positively charged zinc oxide).

The detection of glucose by the functionalized electrodes can be described by the following electrochemical reactions: glucose oxidase enzyme oxidizes glucose and as a result δ-gluconolactone and H_2O_2 are produced [181]. Finally, with the oxygen consumption and H_2O_2 oxidation, it is possible to evaluate the amperometric response of the biosensor [176, 181]. The use of ZnO nanostructures, with high surface-to-volume, in glucose biosensors, will provide a large specific surface area for glucose oxidase adsorption.

Gallay *et al.* [176] was able to produce a ZnO nanowire-based glucose sensor capable of detecting very low glucose concentrations of about 9 μM. Wahab *et al.* [181] used ZnO nanorods for the detection of glucose with concentration ranging from 1 μM to 10 mM. Wang *et al.* [177] synthesized ZnO nanocombs, forming a highly porous structure, that were then immobilized with glucose oxidase, showing a detection limit of 0.02 mM.

One of the most key areas of investigation is the development of rapid systems for the diagnostic of cancer. Researchers have found that some biomolecules like DNA

molecules, human serum albumin and angiotensin II molecules can be effectively immobilized just by modifying the ZnO nanostructures surface [184]. Viter *et al*. [178] have demonstrated that by using photoluminescence properties of ZnO nanorods, it was possible to develop a cancer cell recognition system. By immobilization of SSEA-4 antibodies on ZnO nanorods that were then deposited on the cell probe, it was possible to record photoluminescence spectra that increased when compared with the signal of control samples. Moreover, it was possible to observe that the intensity was correlated with the extent of malignancy in target cell population [178]. Another method for the detection of cancer cells was presented by Rui *et al.* [185]. By adsorbing Cytochrome *c* (Cyt.c) onto ZnO surface, this latter study used ZnO nanosheets to detect H_2O_2 from living cancer cells. Cyt.*c* was found to promote direct electron transfer at the electrode surface [186].

For cardiovascular disease diagnosis, it was possible to develop a sensor that may detect specific concentration ranges of biomarkers that are associated with those diseases. The presence of cardiac troponin (cTnT and cTnI biomarkers) in blood circulation is an indicative of cardiovascular disease [179, 182]. Shanmugam *et al.* [182] developed a flexible and disposable electrochemical sensor capable of detecting very low concentrations of target analyte cTnT with only 20 μL of solution. The limit of detection was identified at 0.1 ng L^{-1}. Tan *et al.* [183] produced a biosensor based on ZnO nanoparticles that was capable of converting the biological interaction of cTnI into an electrical signal. This study also detected the cTnI biomarker in a concentration range of 1 ng mL^{-1} to 10 μg mL^{-1}, withdetection limit of 2.191 ng ml^{-1} and sensitivity of 15.8 nA $(g/mL)^{-1}$.

2.2 Titanium dioxide

TiO_2 is a *n*-type semiconductor usually appearing in an amorphous state or as three crystalline phases: the tetragonal phases, anatase and rutile, and an orthorhombic phase, brookite [187]. Rutile is the most stable phase, in which both anatase and brookite are metastable, transforming to rutile when heated [188]. It has been reported that phase transformation of the amorphous state to anatase occurs from 300 to 500 °C, and further transformation to rutile occurs at 600-1000 °C [103, 189].

Rutile and anatase tetragonal structures contain six and twelve atoms per unit cell, respectively. For both phases, each Ti atom is coordinated to six O atoms and each O atom is coordinated to three Ti atoms. The TiO_6 octahedron is slightly distorted, with two Ti-O bonds somewhat greater than the other four, having some of the O-Ti-O bond angles distorted from 90 º (greater distortion in anatase than rutile). The structures of rutile and anatase crystals consist of chains of TiO_6 octahedra, sharing four edges in anatase and two in rutile. In the case of brookite, it has distorted TiO_6 octahedra sharing three edges. Moreover, brookite has eight formula units in the orthorhombic cell, in which the interatomic distances and O-Ti-O bond angles are similar to those of rutile and anatase, nevertheless it has six different Ti-O bonds [190, 191]. Rutile, anatase and brookite unit cells are presented in Figure 10.

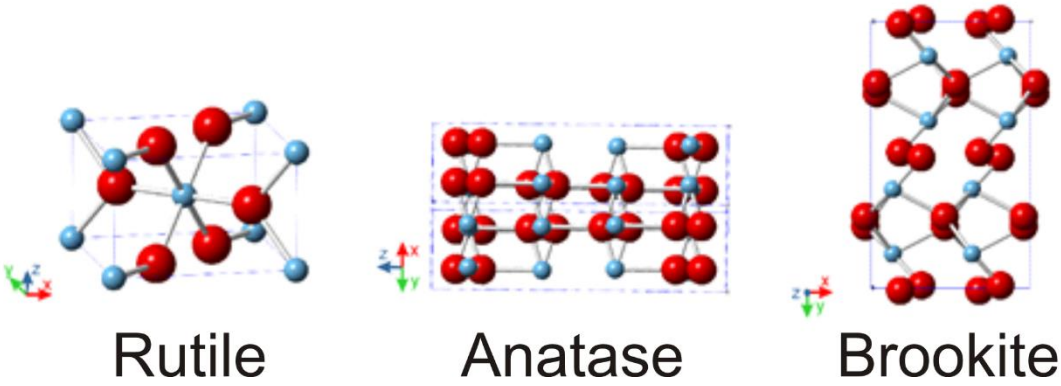

Figure 10. Unit cells of TiO_2 rutile, anatase and brookite [192]. Reproduced with permission of *Intech*.

TiO_2 is a wide energy band gap material, typically displaying optical band gaps of 3.0 and 3.2 eV for rutile and anatase, respectively [193], and varying from 3.13 to 3.40 eV [188, 193] for brookite. Nevertheless, its optical bang gap for nanostructured materials can be engineered by adding structural defects or doping with non-metal and metal elements also to narrow its band gap [194-196]. TiO_2 has a high refractive index (2.71 for rutile, 2.53 for anatase and 2.64 for brookite [191]), high dielectric constant (TiO_2 thin films ranging from 40 to 86 [197, 198]) and high resistivity extending to 10^8 Ω.cm [199]. The lattice parameters for rutile ($P4_2/mnm$) are a= 0.4594 nm and c= 0.2958 nm, while anatase ($I4_1/amd$) has lattice parameters of a= 0.3785 nm and c= 0.9515 nm, and brookite (*Pbca*) has lattice parameters of a= 0.9184 nm, b= 0.5447 nm, and c= 0.5145 nm [191, 200].

Several techniques have been reported to produce TiO_2 nanostructures or thin films including sol-gel method [201], wet-chemical techniques [202, 203], thermal evaporation [204], sputtering [205], electrodeposition [206], hydrothermal and solvothermal synthesis [207-210], microwave irradiation [10, 192], amongst others. Various and distinct structures have been reported for TiO_2 nanomaterials, especially as nanoparticles, including nanowires, nanorods, nanotubes, nanobelts, nanowhiskers, nanospheres and others [10, 203, 211-213].

TiO_2 is known to be an inexpensive material, earth abundant, chemically stable, non-toxic, biocompatible, and environmentally friendly [203, 214], which makes it prone to be applied in numerous fields, including solar cells [25, 215, 216], self-cleaning [217, 218], photocatalysis [9, 10, 192], H_2 production [219], CO_2 reduction [220, 221], sensors [222-224], among others. Anatase is the preferred phase for solar cell integration since it has high electron mobility, low dielectric constant and lower density [225, 226]. TiO_2 has been widely investigated for photocatalytic H_2 evolution, photoelectrochemical water

splitting, reduction of CO_2 to hydrocarbons, and pollutant degradation for many years. In terms of photocatalytic activity, anatase is expected to exhibit an indirect band gap that is smaller than its direct band gap. Rutile presents a direct band gap or an indirect band gap that is comparable to the direct one. It is known that semiconductors with indirect band gap generally exhibit longer charge carrier life times and thus longer electron-hole pair life would facilitate charge carriers participation in surface reactions [227]. Nevertheless, it has been reported that the mixture of both phases displayed higher photocatalytic activity than pure phases [228]. In the case of brookite, this material is the least investigated TiO_2 polymorph, however it has been reported to display higher photocatalytic activity than anatase or rutile [229].

In terms of sensors, and as previously mentioned, a high-quality sensor is expected to have greater sensitivity, high detection limit, response/recovery time and stability and longer life cycles. These parameters are related to characteristics of the sensing material, such as grain size and microstructure, which directly influence the sensor's sensitivity [199]. In this sense, nanostructured materials have been extensively used in sensors over the years, including nanostructured TiO_2 materials that have enhanced chemical stability allowing low temperature operation. This materials has inert characteristics, and is resistance to harsh atmospheric conditions, despite being low-cost in terms of production and compatible with wet-chemical synthesis routes [230].

TiO_2 has been widely used as photoactive layer of gas sensors, where TiO_2-based gas sensors are typically chemiresistive, having the working principle of typical *n*-type semiconductor gas sensor materials based on its conductance change mechanism due to adsorption/desorption process of oxidizing and reducing gases [231].

Liu *et.al.* [232] reported the hydrothermal synthesis of TiO_2 nanocrystals with various percentages of exposed {001} facets displaying *p*-type and *n*-type sensing responses

towards ethanol (Figure 11 (a)). In another study, TiO_2 nanowire sensors revealed excellent selectivity and high sensitivity down to 100 ppm NO_2 at room temperature with response and recovery times of 10 s and 19 s, respectively. Furthermore, the nanowires displayed good repeatability and selectivity against various interfering gases such as NH_3, H_2, and CH_4 [233]. TiO_2 nanostructured films composed of different morphologies, nanoparticles and nanotubes were synthesized by hydrothermal method and it has been shown that sensing films composed of nanotubes demonstrated a high sensor response to toluene [234].

It is also known that well-ordered porous metal oxide structures are highly efficient for improving gas sensing, in which this porosity increases surface area of the material, enhancing its interaction with the gaseous species [231]. TiO_2 spongy layers with double-scale porosity at the meso and nano-scale have been reported and exhibited sensitivity of 44 ppm to ethanol at 250 °C. Moreover, response of the material was demonstrated to be independent of ambient humidity with a response time as low as ~10 s [235].

Another approach that has been widely used is doping with small metal clusters. Doping will have a significant effect for the metal oxides which are dominated by defect chemistry (via oxygen vacancies). Oxygen vacancies are considered important reactive agents for several adsorbates, in such a way that surface reactions are influenced by this type of point defect [49]. Ruiz *et al.* [236] reported the effect of doping TiO_2 with chromium, in which it has been observed that the addition of Cr retarded the anatase-to-rutile TiO_2 transformation, moreover these materials revealed to be sensitive to 1000 ppm CO, but also to NO_2. In another study, it has been described TiO_2 sol-gel films doped with gold nanoparticles used as both optical and conductometric sensors for the detection of CO and H_2 [237]. The combination of different oxides has also been reported to surpass limitations of each metal oxide material. Carney *et al.* [238] produced TiO_2-SnO_2

nanofiber-structured films that were tested for sensing H_2. This combination allowed to increase TiO_2 gas sensitivity and supress SnO_2 sensors limitations that utilize low-temperature chemisorption (under 400 °C) of gases on the surface. Above 400 °C, SnO_2 exhibits poor sensing performance, while TiO_2 is stable at higher temperatures.

In terms of humidity sensors, TiO_2 is known to have superior humidity sensitivity with the preferably hydrophilic property resulting from the surface defects, *i.e.* the Ti^{3+} defect sites or oxygen vacancies sites, that can adsorb water molecules in the atmosphere [239]. Nevertheless, reported TiO_2-based humidity sensors usually display limited sensitivity resultant of low surface/volume ratio, high resistance or poor charge transfer process of single phased TiO_2 material. Thus, several approaches have been designed to overcome these limitations. Ultrathin 2D TiO_2 nanosheets with high specific surface area and surface oxygen vacancy defects have been reported as having ultrahigh humidity sensing performance. These nanostructured sensors revealed significant impedance variation from RH 11% to 95%, short response time (3 s) and recovery time (50 s), as well as small hysteresis ~ 4.6% (Figure 11 (b)) [239]. Lin *et al.* [240] reported a humidity sensor based on graphene/TiO_2 that at 12-90 %relative humidity , exhibited a sensing response (S = 151) and humidity hysteresis value of < 0.39 %. In another study, flexible sensors based on TiO_2 and conducting polymers have been described. These humidity sensors demonstrated hysteresis (range of 30–90 % RH) of 2 % RH, with response time of 30 s, and recovery time of 45 s [241]. Doping TiO_2 was also considered for producing enhanced humidity sensors. Zare *et al.* [242] reported the effect of doping TiO_2 with silver in terms of humidity sensitivity, while Buvailo *et al.* [243] showed TiO_2-based nanomaterial doped with LiCl to produce conducting thin film sensors. The latter sensors were measured in the RH range of 5-95 % and revealed 0.75 and 1 s for sensor response and recovery time, respectively.

Recently, TiO_2 has been considered as a good alternative for the most common used UV sensors, *i.e.* silicon-based sensors [244], as TiO_2 is highly photoactive and stable under UV irradiation due to its band gap [67, 245, 246]. Highly oriented rutile TiO_2 nanorod arrays were synthesized by hydrothermal method and tested as UV sensors achieving a photocurrent of 12.87 μA cm^{-2} under 365 nm UV light exposure [224]. In another study, anodic TiO_2 anatase nanotube arrays were tested as UV sensors showing high responsivity of 13 A W^{-1} under λ = 312 nm and fast response with rise time and decay time of 0.5 and 0.7 s, respectively [247]. Epitaxial TiO_2 thin films were fabricated on $LaAlO_3$ single crystal substrates by RF magnetron sputtering, and the sensor exhibited a maximum photoresponse of 3.63 A W^{-1} at 310 nm and ultrahigh response speed (~90 ns) [248]. Nano-branched TiO_2 arrays were integrated on self-powered UV sensors. The photosensitivity increased from 0.03 to 0.22 A W^{-1} exhibiting excellent spectral selectivity and fast response (0.05 s decay time) [249].

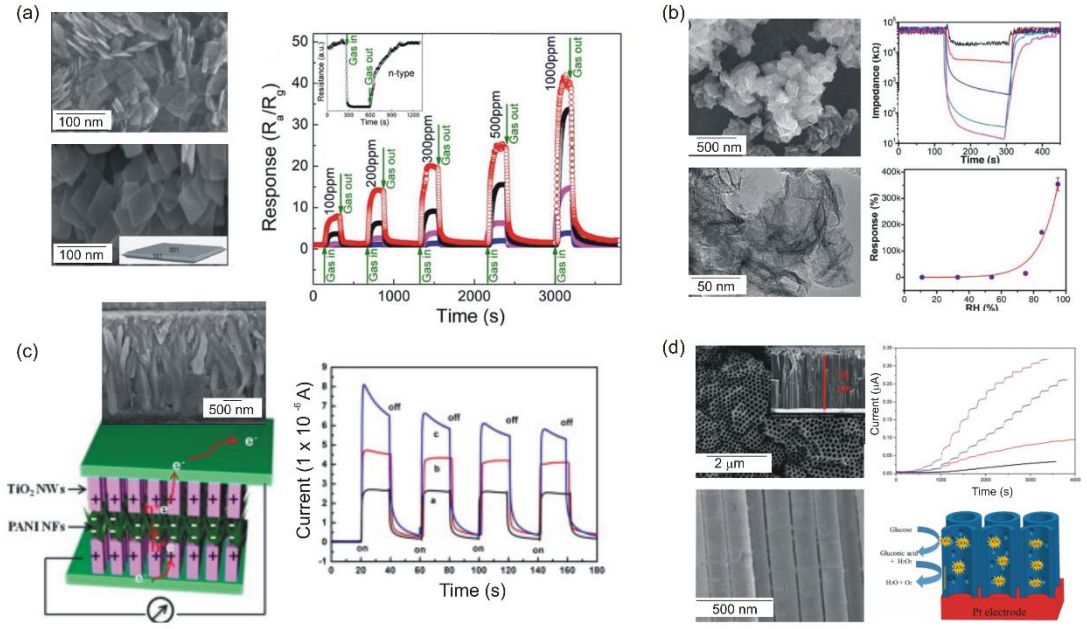

Figure 11. (a) SEM images of TiO_2 nanosheets together with the response and recovery curves of the sensors as a function of ethanol concentration [232]. (b) SEM and TEM images of TiO_2 nanosheets for humidity sensors together with the transient responding dynamics of the impedance of TiO_2 nanosheets-based sensor and calibration curve [239]. (c) SEM images of TiO_2 nanowires/PANI/TiO_2 nanowires heterostructured arrays to be used as UV photodetectors together with the time responses of photocurrents under UV light [250]. (d) SEM and schematic diagram of glucose detection on mesoporous GO/TiO_2 nanotubes. The graph showed the current responses with successive injections of glucose [251]. Reproduced with permission of *Elsevier,* [232], [239] and [250], and *Royal Society of Chemistry* (2018) [251].

D. Nunes *et al.* [246] reported the microwave synthesis TiO_2 nanostructured films grown on bacterial nanocellulose (BNC), tracing paper and polyester film substrates to produce flexible and disposable UV sensors (Figure 12). The UV devices showed responsivities of 0.33 μA W^{-1}, 0.16 μA W^{-1} and 0.07 μA W^{-1} for TiO_2 films grown on BNC, tracing paper and polyester substrates, respectively. The structural characteristics of the TiO_2 films and substrates were correlated to differences in the UV photodetection.

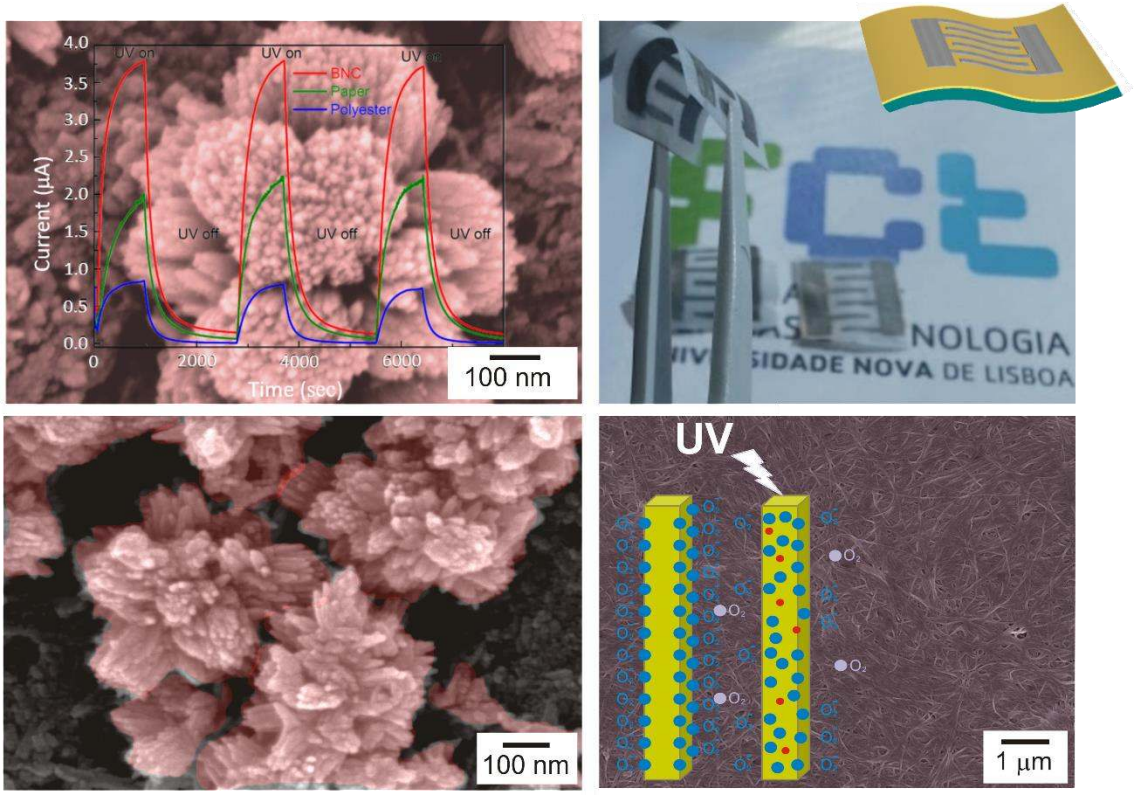

Figure 12. TiO_2 nanostructured films composed by nanorod flower-like structures to be integrated as the photoactive layer of flexible UV sensors. The films were grown on tracing paper, bacterial nanocellulose and polyester substrates. The cycling behaviour of the photodetectors at 10 V and under a 360 nm UV source were investigated. The schematic diagrams of dark and UV irradiation processes are presented. Images reproduced with permission of *Springer Nature* (2018) [246].

Another solution proposed to reduce electron-hole recombination is production of metal-doped TiO_2 materials. It has been reported that Au nanoparticles deposited on TiO_2 nanotubes showed good wavelength selectivity with high photocurrent as compared to pure TiO_2 devices [252]. The addition of other oxides has also been addressed, for example in the case of SnO_2, it possesses high electron mobility, suggesting a faster diffusion transport of photon-induced electrons to TiO_2 [253]. Chen *et al.* [253] reported SnO_2-TiO_2 nanomace arrays exhibited responsivity of 0. 145 A W^{-1} at 365 nm, rising time of 0.037 s, and decay time of 0.015 s. Zu *et al.* [250] reported a self-powered UV photodetector based on heterostructured arrays of TiO_2 nanowires/polyaniline

nanoflowers/TiO_2 nanowires (Figure 11 (c)). The heterostructure revealed improved sensing performance when compared to bare TiO_2 nanowires.

Metal oxides sensing applications, including in biosensors, is growing fast in recent years. In the case of biosensors, these devices are a rapidly expanding field in analytical chemistry, with an estimated 60 % annual growth rate [254]. This impulse is coming from health-care industry, food quality and safety, but also from environmental monitoring. When comes to using TiO_2 in biosensors, several studies have focused on producing 1D nanostructures forming continuous arrays [223, 251, 255, 256]. The use of TiO_2 nanotube/nanorod arrays is related to large internal surface area, negative surface charge and high refractive index of these arrays allowing incorporation of biomolecules and high analyte sensitivity [223, 255]. Mun *et al.* [223] reported the production of TiO_2 nanotube arrays for label-free optical interferometric biosensing using a protein A capture probe and an immunoglobulin analyte [223]. Mesoporous TiO_2 nanotube arrays had immobilized glucose oxidase (GO) to produce a biosensor for amperometric detection of glucose. The amperometric response of glucose on the GO/TiO_2 electrode was reported to be proportional to glucose concentration in the range from 0.1 to 6 mM with a sensitivity of 0.954 $\mu A\ mM^{-1}\ cm^{-2}$ (Figure 11 (d)) [251]. Hu *et al.* [255] produced carbon-doped TiO_2 nanotube arrays for simultaneous detection of 5-hydroxytryptamine and ascorbic acid, which can also be readily regenerated photocatalytically to recover its high selectivity and sensitivity. Gao *et al.* [256] reported a graphene/TiO_2 nanorods/chitosan nanocomposite modified carbon ionic liquid electrode to produce an electrochemical DNA biosensor for detection of the transgenic soybean sequence of MON89788. The target ssDNA sequence was detected in the range from 1.0×10^{-12} to 1.0×10^{-6} mol L^{-1} with detection limit of 7.21×10^{-13} mol L^{-1}.

In another approach, TiO_2 nanoparticles were used to produce a nanocomposite with graphene oxide nanosheets. The amperometric response of the glucose biosensor fabricated by the TiO_2-graphene composite was linear against a concentration of glucose ranging from 0 to 8 mM at -0.6 V. The highest sensitivity was shown at 6.2 μA mM^{-1} cm^{-2}, and the glucose biosensor based on the TiO_2-graphene composite showed higher catalytic performance for glucose redox than a pure TiO_2 and graphene biosensor [257]. Another study demonstrated the enzyme immobilization by amperometric biosensors with TiO_2 nanoparticles to detect phenol compounds [258].

2.3 Tungsten trioxide

Tungsten trioxide is one of the most investigated transition metal oxide materials exhibiting a wide variety of novel properties. WO_3 is a *n*-type semiconductor material with a wide energy band gap varying from 2.6 to 3.25 eV [29, 259]. WO_3 can present different crystallographic phases, such as cubic, hexagonal, monoclinic, triclinic, tetragonal and orthorhombic [260-264]. The cubic WO_3 is hardly obtained experimentally, but oxygen vacancies in the WO_3 lattice are capable of increasing the cell symmetry from monoclinic via tetragonal to cubic phase [265].

The most studied WO_3 phases are the monoclinic ($P2_{1/n}$), orthorhombic (*Pbcn*) and hexagonal (*P6/mmm*). The monoclinic phase lattice parameter was reported to be *a*= 0.7301 nm, *b*= 0.7539 nm, and *c*= 0.7689 nm [266] and consists of WO_6 octahedral connected by corner sharing of oxygen atoms, connected in the *a-, b-* and *c-* directions; the orthorhombic phase with lattice parameters of *a*= 0.7333 nm, *b*= 0.7573 nm, and *c*= 0.7740 nm [267] is based on two octahedral, $WO_5(H_2O)$ (with two oxygen atoms forming W=O and W-OH_2 bonds) and WO_6 with W-O bonds sharing the same bond length; the hexagonal phase with cell parameters *a*= 0.7298 nm and *c*= 0.7798 nm [268] consists of WO_6 octahedral structures sharing equatorial oxygen atoms, forming trigonal and

hexagonal tunnels [261, 264]. Both monoclinic and hexagonal phases consist of WO_6 octahedral, but with different arrangements. Figure 13shows SEM images of the different morphologies and WO_3 crystallographic phases.

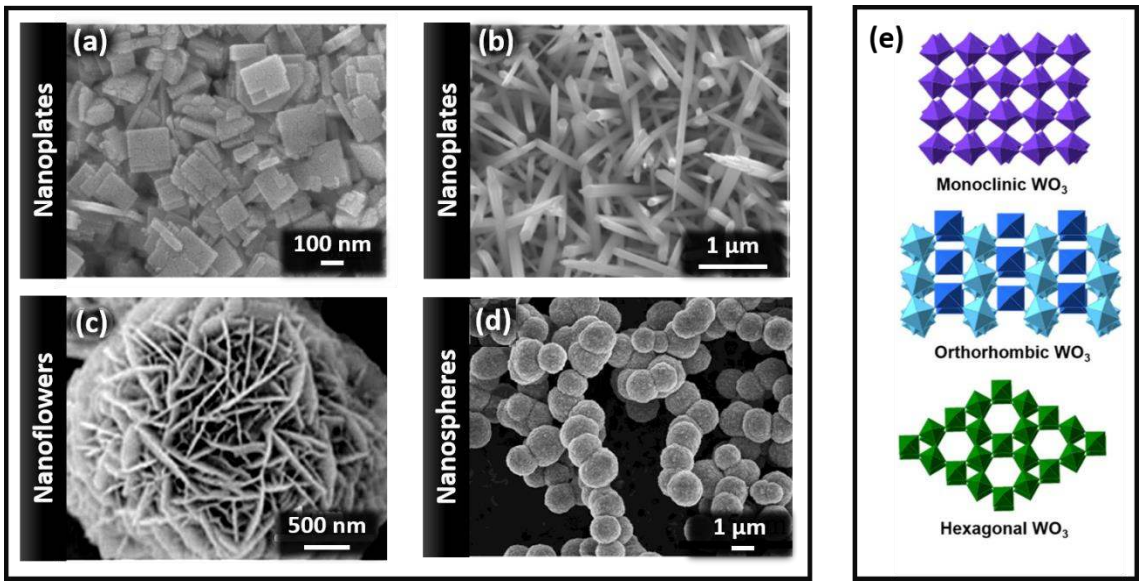

Figure 13. SEM images of WO_3 (a) nanoplates produced by microwave hydrothermal method [269]; (b) nanowires produced by thermal evaporation [270]; (c) nanoflowers produced by hydrothermal method [271]; (d) microspheres produced by hydrothermal method [272]. (e) Crystallographic structures of different WO_3 phases [262]. Reproduced with permission of *Hindawi* [269], *Elsevier* [270], [271], and [272], and *Springer Nature* (2018) [262].

Many researchers have concentrated their studies on novel and more efficient synthesis techniques for producing WO_3 nanostructures, such as conventional and microwave hydrothermal/solvothermal syntheses [273-275], electrodeposition [276], chemical bath deposition [277], chemical vapour deposition [278] and electrospinning [279, 280]. By using these different synthesis techniques, tungsten trioxide may grow with different morphologies like nanoplates [269, 281, 282], nanowires [270, 283, 284], nanorods [285, 286], nanoflowers [271, 287] and hollow nanospheres [272, 288].

Due to its thermochromic properties, WO_3 is mostly used in intelligent electrochromic windows, surfaces for energy-efficient architectures and flat-panel displays [289-295]. Moreover, this material is widely used in solar photocatalysis [273, 296, 297], but it has

also been demonstrated that this semiconductor material exhibits enhanced chemical sensing properties and is used in several sensing applications [298-301].

WO_3 has been largely employed in gas sensors with remarkable gas sensing properties for the detection of NO_2 [302-304]. In Ref. [303], it has been shown the NO_2 response of lamellar-nanostructured WO_3 particles. The gas sensor exhibited high sensor response (S = 150-280) to dilute NO_2 (50-1000 ppb) in air at 200 °C. Sensitive porous WO_3 nano-crystalline based NO_2 sensor has been reported in [304]. The sensor showed high sensitivity to low NO_2 concentration in the range from 50 to 550 ppb with relatively fast response time (~ 3 min) and recovery time (~ 1 min). A three-dimensional hierarchical WO_3 nanostructure with nanosheet-assembled morphology has been used in gas sensors. The sensor response to 40 ppb NO_2 was reported to be 2.4. It has also been reported that this sensor has good selectivity to NO_2, as the signal was higher for this gas when compared to other oxidizing gases (Cl_2) or reducing gases (CO, H_2S, NH_3, acetone and ethanol) [305]. An *et al.* [306] reported WO_3 nanotube sensors with responses of 144-677% in NO_2 concentration range of 1-5 ppm at 300 °C.

Lin *et al.* [57] reported WO_3 hollow-sphere gas sensors with satisfactory sensitivity to alcohol, acetone, CS_2, NH_3, and H_2S. With increasing gas concentration, sensitivity of the sensors sharply increased. The sensors were more sensitive to alcohol and acetone than to other organics. Another work showed a WO_3 nanowire-like structure for high sensitivity NH_3 gas sensor. The NH_3 gas-sensing properties of these nanowires were measured, showing maximum response of 9.7-1500 ppm at 250 °C with response and recovery times of 7 and 8 s, respectively [307]. WO_3 nanostructures synthesized by hydrothermal method were reported in Ref. [308]. The responses for the sensors increased significantly with the increase of the acetone gas concentration. One of the sensors demonstrated increased sensitivity from 4.1 to 15.8 when the concentration of acetone

was changed from 10 ppm to 400 ppm. The sensing selectivity was also explored by comparing the response to acetone, ethanol, formaldehyde and ammonia gases with various concentrations.

The use of WO_3 in the form of films for gas sensing was also investigated. Oriented WO_3 nanoflakes array films were tested as gas sensors in Ref. [298]. The WO_3 thin film sensor exhibited responses of 2.8-9.8%, 12.8-68.9% and 26.2%-85% respectively, to 0.1-10 ppm of H_2S concentration at various operating temperature such as 100 °C, 200 °C and 300 °C, respectively. The WO_3 thin film sensor showed a high response to H_2S that increased with H_2S gas concentration. Sulfur dioxide gas sensors based on WO_3 screen printed thick films composed of nanopowders were demonstrated in [309]. The sensors exhibited responses to 1-10 ppm SO_2 at 200-300 ºC, which has been shown to be strongly dependent on WO_3 morphology. Nanoparticle WO_3 films were used as gas sensors for ethanol and H_2S. The working temperature of the sensor was between 150 and 250 °C and it was possible to detect 200 ppb of ethanol and 20 ppb of H_2S [310].

Different approaches have been designed to efficiently enhance the gas sensing characteristics of WO_3, including doping with noble elements, other metal oxides (forming of *p-n* heterojunction) or carbon-based materials. Au nanoparticle modified WO_3 nanorods were tested as H_2 sensors, exhibiting larger response to H_2, *i.e.* 50 ppm and recovery time lower than 10 s [311]. In another study, Pt nanoparticles were functionalized on WO_3 hybrid nanorods to be used as gas sensor. The gas sensing to varied concentrations (1, 5, 20, 100 and 200 ppm) of ethanol and methanol at 220 °C were demonstrated, with better performance than pure WO_3 [312]. In Ref. [313], Cr-doped WO_3 nanofibers were reported to have high response towards 100 ppm xylene and long term stability. Ag doped WO_3-based powder sensors for detection of NO gas in air were reported in Ref. [314], demonstrating a sensitivity of 38.3 at 250 ºC. This value was

compared to the sensor without Ag doping. 3D hierarchical monoclinic-type structural Sb-doped WO_3 gas sensing material was described in Ref. [315]. The results of gas sensor measurements indicated that the 3D material has superior sensitivity (S = 122) and high selectivity to ppm-level NO_2 at 30 °C. It has been demonstrated that abundant structural defects derived from Sb doping modification, reduced band gap, and 3D hierarchical microstructure played a key role on the NO_2 gas sensing performance.

Ref. [316], reports CuO/WO_3 heterostructured nanocubes that were used to sense H_2S gas in a concentration as low as 50 ppb. By combining these with electric modulation, the sensors simultaneously exhibited fast recovery and ultrahigh sensitivity for detecting H_2S gas at low temperature. Nanocrystalline TiO_2:WO_3-based hydrogen sensors were reported in Ref. [317]. The sensitivity to H_2 was observed to be 0.91 and 0.94 at 200 ºC depending on the amount of Pd doping, with a response time of 1 min. Kumar *et al.* [318] reported a sensor based on the Pd/WO_3-ZnO nanocomposite showing remarkably improved H_2 sensing performance, good stability and excellent selectivity when compared to that of pure WO_3 and ZnO, at a relatively lower operating temperature (200 ºC) and with a low detection range of 10-1000 ppm. The Pd/WO_3-ZnO composite sensor exhibited a stable response over 20 cycles towards 100 ppm of H_2 at 200 ºC. The response and recovery time achieved were 16 s and 62 s, respectively, towards 100 ppm H_2 at 200 ºC. Shouli *et al.* [319] reported WO_3-SnO_2 nanocomposites to act as NO_2 sensors. The sensor exhibited the highest response for 186 to 200 ppm of NO_2 at operating temperature of 200 °C, with an increased response when Zn or MgO were added (responses of 251 and 418, respectively).

Zhang *et al.* [279] produced pure WO_3 and graphene oxide-WO_3 composite nanofibers to be applied as gas sensors. The graphene oxide-WO_3 composite nanofibers displayed the highest response of 35.9-100 ppm acetone at 375 °C, which is 4.3 times

higher than that of pristine WO_3 nanofibers. Good selectivity and stability to acetone were also demonstrated for the composite nanofibers (Figure 14 (a)). WO_3 nanorods/graphene nanocomposites to act as NO_2 sensors were described in [320], and their gas sensing performance was compared to pure WO_3 nanorods. The response of WO_3 nanorods/graphene to 25 ppb, 100 ppb, 500 ppb and 1 ppm NO_2 were 13, 25, 40 and 61, respectively, while those of WO_3 nanorods were 2.6, 3.3, 5 and 5.3, respectively. In Ref. [321], Pd-WO_3/reduced graphene oxide (rGO) hierarchical nanostructures were used as efficient hydrogen gas sensors. These materials were sensitive to 20 ppm of hydrogen gas at room temperature, and the best operating temperature in terms of sensitivity (10^2) was 100 ºC with responses of < 1 min.

The relation between humidity and gas sensing was also explored. In Ref. [322], the effect of relative humidity on NO_2 sensitivity of a SnO_2/WO_3 heterojunction gas sensor was investigated. The sensor showed high sensitivity and a pseudo-linear response to NO_2 in the range 0-5 ppm in dry air. Response to variations in relative humidity was reported to be small at RH levels below 40%, with the sensor becoming saturated at higher values of RH. Strong interference effects were observed, with sensitivity to NO_2 decreasing rapidly as the RH of the atmosphere increased. Hybrid sensors were developed from Fe-doped WO_3 film and reduced graphene oxide top layer. The sensors were tested towards different concentrations of NO_2 and relative humidity at different temperatures ranging from 25 °C to 100 °C, showing fast dynamics to humidity when compared to NO_2. A response time of 6.7, 6.6 and 4.9 min and 6.54, 5.9 and 5.47 min to 10 % RH and 50 % RH, respectively at temperatures of 25, 50 and 100 °C were obtained [323].

The humidity-sensing process is generally based on the adsorption of water molecules and structure defects play a key role in this process. WO_3 is an interesting alternative as

a humidity sensing material since it has a variety of nonstoichiometric defects and oxygen vacancies [324]. Several approaches have been developed to increase WO_3 humidity sensitivity. In Ref. [325], the effect of Ni doping was studied, in which the humidity sensing properties of pure WO_3 were significantly improved by Ni dopant. This was justified with the high surface area and smaller band gap energy of Ni-WO_3. The sensitivity was improved with the increase in relative humidity. A Li/K co-doped 3D ordered material (3DOM) WO_3 humidity sensor was presented in Ref. [324] (Figure 14 (b)). The sensor response and recovery times were 15 and 10 s, respectively, with the maximum hysteresis of 3 % RH for 11 to 95 % RH, indicating good sensor reliability. The enhanced humidity sensing behaviour was attributed to structural defects, adsorbed oxygen and the coeffect of Li/K. Moreover, to access the interaction of this material with other gaseous species that might be present in ambient air, its gas sensing performance was evaluated.

Several other studies reported the humidity sensing of WO_3 materials and when in association with other materials. In Ref. [326], the photoelectric responses of nanocrystalline WO_3 film to humidity under UV light irradiation were investigated in humidity range of 20-80 % RH at room temperature. Dong *et al.* [327] reported a WO_3 film deposited on silicon nanoporous pillar arrays to be used in capacitive humidity sensors. With relative humidity changing from 11 % to 95 % sensitivity over 16000 % at an optimal measuring frequency of 1000 Hz, has been reported. The response and recovery times were determined to be ~104 and ~ 94 s, respectively, with maximum humidity hysteresis ~ 5.3 % at 65 % RH. Patil *et al.* [328] reported on the humidity sensing properties of poly(2, 5-dimethoxyaniline)/WO_3 composites. The sensor demonstrated to change linearly over an humidity range of 23-84 % with maximum percentage response factor of ~651 at 87 % RH, as well as quick response (humidification,

27 s and desiccation, 136 s) and narrow hysteresis (~5 %). In another study, WO_3-ZnO nanocomposites were produced and their humidity sensitivity tested. It has been shown that when % RH increases, there is a decrease in the resistance for the humidity range from 15 % to 95 %. The sensor showed a maximum sensitivity of 16.42 M Ω/% RH and narrow hysteresis (1.09 %) [329].

WO_3 has also the potential to be integrated in UV photodetectors/sensors since it has an indirect large energy band gap (3.3 eV). Lately, WO_3 nanostructures have been used to overcome limitations reported for WO_3-based UV sensors, such as slow response times (> 1 min) [330]. WO_3 nanosheets were used as high-performance UV photodetectors/sensors, showing excellent optoelectronic performance with high sensitivity (293 A W^{-1}), fast response speed (40 ms), high on/off ratios (2000) and high external quantum efficiency (997 %) [331]. Li *et al.* [332] reported WO_3 nanowires synthesized on carbon papers to be used as UV photodetectors/sensors (Figure 14 (c). These WO_3 hierarchical sensors demonstrated response and decay times of about 3 s and 20 s, respectively. In another study, hexagonal WO_3 nanowires were also tested as UV photodetectors. An increase of more than two orders of magnitude in conductance was obtained under UV illumination at 312 nm with a photoconductivity gain of 4.6×10^3 [333]. In Ref. [334], WO_3 nanobelts were produced via electrospinning for application as UV photodetectors. The sensor's photocurrent increased to ~ 12 nA and then rapidly decreased to its initial value (12 pA) once the light is turned off, suggesting high sensitivity of the photodetector with photo-dark current ratio up to 1000. A responsivity and external quantum efficiency up to 2.6×10^5 A W^{-1} and 8.1×10^7 %, respectively, have also been demonstrated. Shao *et al.* [335] reported 3D WO_3 nanoshale structured materials synthesized using hydrothermal synthesis. The UV photodetector fabricated with 3D WO_3 nanoshale showed good photoresponsivity (5.1 A W^{-1}), which was

attributed to the internal gain introduced by surface oxygen adsorption–desorption process, as well as high surface to volume ratio of the 3D nanoshale structure. In Ref. [330], an ultraviolet photodetector was fabricated from WO_3 nanodiscs and reduced graphene oxide composite material. A maximum photoresponsivity of 6.4 A W^{-1} at 347 nm was observed under 20 V bias. The rise time (as measured from 10 % to 90 %) and fall time (from 90 % to 10 %) of the photodetector were reported to be 13 and 16 ms, respectively.

UV photodetectors/sensors with WO_3 in the form of films were also explored. Cook *et al.* [336] reported WO_3 films produced by inkjet printing to be used as UV photodetectors. Large on/off ratio of 3538 and high responsivity up to 2.70 A W^{-1} at 5 V bias (0.54 A W^{-1} V^{-1}) were obtained. In another study, a monolayer WO_3-based UV-A photodetector was reported. The sensor has demonstrated fast response time of less than 40 μs and photoresponsivity reaching ~0.329 A W^{-1}. Long-term stability exceeding more than 200 cycles without any visible degradation was also showed [337].

In terms of biosensors, the remarkable properties of WO_3 that include reversible change of conductivity, high sensitivity, selectivity and biocompatibility, make this material suitable for integration in biosensors [338]. Deng *et al.* [339] reported direct electron transfer of cytochrome *c* at WO_3 nanostructures. A combination of direct electrochemistry of cytochrome *c* at the nanostructured WO_3 surface and enzymatic catalytic activity of cytochrome *c* towards H_2O_2 resulted in a third-generation H_2O_2 biosensor with high selectivity. The biosensor demonstrated a wide linear detection range from 3×10^{-7} to 3×10^{-4} M, low-detection limit (2.4×10^{-7} M) and short response time of 5 s. Liu *et al.* [340] reported WO_3 nanowires with high length-diameter ratio that were used to immobilize hemoglobin to fabricate a mediator-free nitrite biosensor. The biosensors displayed superior performance for detection of nitrite with a wide linear range

of 1 to 4200 μM, as well as an extremely low detection limit of 0.28 μM (Figure 14 (d)). Anithaa *et al*. [341] reported WO_3 nanoparticles with monoclinic (γ) and orthorhombic (β) structures synthesized by simple microwave irradiation to be applied for mediator-free dopamine detection. The γ-WO_3 modified glassy carbon electrode exhibited a linear response over a wide concentration range of 0.1 μmol L^{-1}-600 μmol L^{-1} of dopamine with lowest detection limit of 24 nmol L^{-1}. The dopamine sensor showed excellent anti-interference ability against electroactive species and metal ions with good stability and reproducibility. In Ref. [342], polyethylene glycol assisted WO_3 nanoparticles were used for L-dopa bio-sensing applications. The detection limit to L-dopa was demonstrated to be 120 nM.

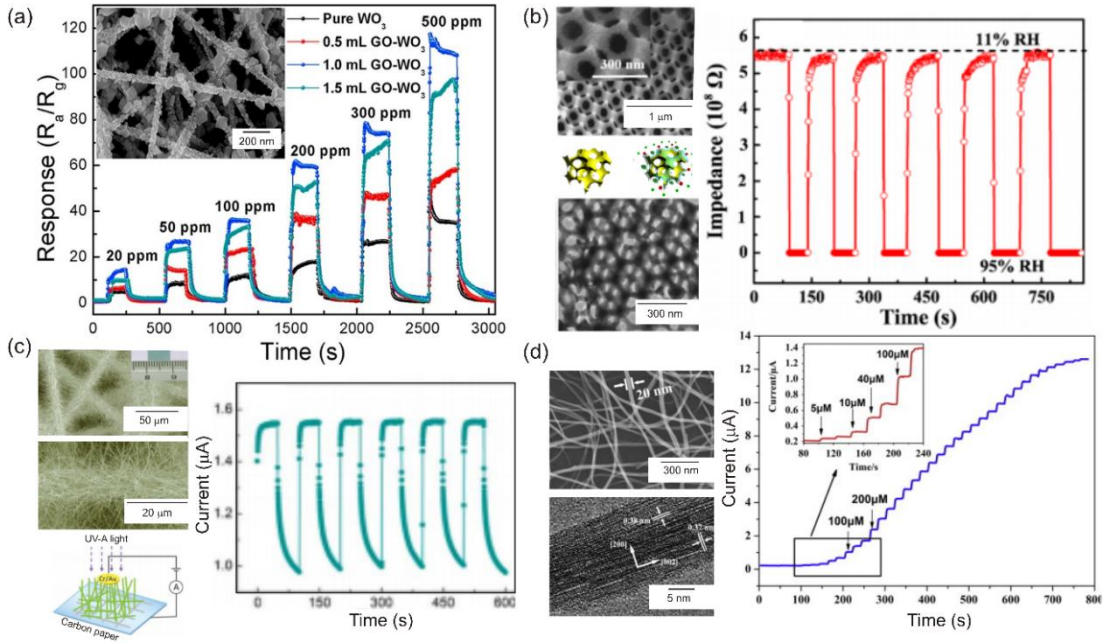

Figure 14. (a) Graphene oxide-WO_3 composite nanofibers and dynamic gas sensing curves of the sensors as a function of acetone concentration [279], (b) SEM and TEM image of a Li/K co-doped 3D ordered material to be used as WO_3 humidity sensor [324] and realtime impedance under different RH. (c) SEM images of WO_3 nanowires and the scheme of the UV photodetector with its corresponding light switching ''ON'' and ''OFF'' curve [332]. (c) SEM and TEM images of WO_3 nanowires and the graph shows the current–time response of the Nafion/hemoglobin/WO_3 nanowires/glassy carbon electrode [340]. Reproduced with permission of *Elsevier* [279] and [340], *ACS publications "Copyright (2018) American Chemical Society"* [324], and *Royal Society of Chemistry* (2018) [332].

In Ref. [343], bovine hemoglobin was electrostatically immobilized on WO_3 nanoparticles, multiwalled carbon nanotubes were added and this was applied to modify a carbon paste electrode. The fabricated biosensor showed suitable electrocatalytical properties in the simultaneous determination of levodopa (L-DOPA), folic acid, and uric acid. Santos *et al.* [338] reported the synthesis of WO_3 nanoparticles by hydrothermal method with different structures (Figure 15) to be used as nitrite biosensors. In this study, c*c*NiR was chosen as model enzyme due to its high catalytic activity towards nitrite reduction, and c*c*NiR modified (c*c*NiR/WO_3/ITO) electrodes were produced. The biosensors demonstrated sensitivities of 2143 mA M^{-1} cm^{-2}.

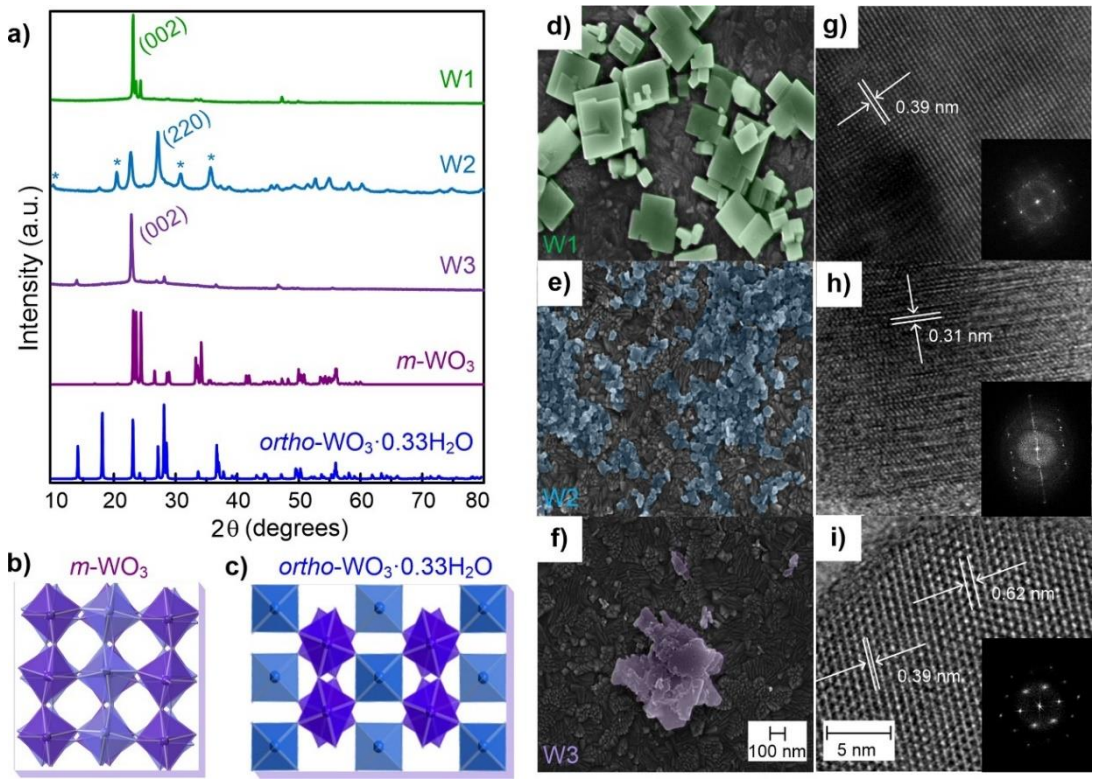

Figure 15. (a) to (i) XRD, SEM and TEM measurements of hydrothermally synthesized WO_3 powders to be used as nitrite biosensor [338]. Reproduced with permission of *Elsevier* (2018).

Marques *et al.* [262] reported WO_3 nanoparticles synthesized by microwave assisted hydrothermal synthesis which were used to impregnate non-treated regular office paper substrates. This allowed the production of a paper-based colorimetric sensor (Figure 16 (a)) able to detect electrochemically active bacteria in different growing stages

by electrochromic reaction. A colorimetric relation between the growing stage of bacteria and WO_3 nanoparticles concentration was presented with RGB analyses (Figure 16 (b)).

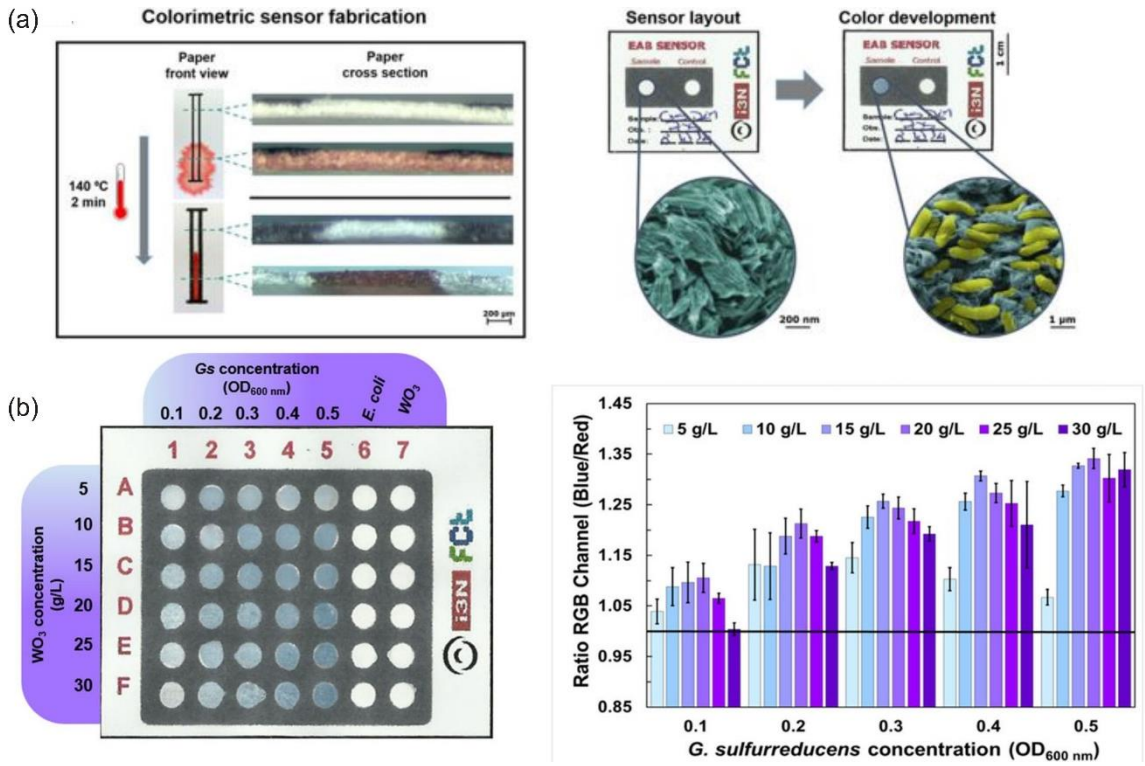

Figure 16. (a) Scheme of the colorimetric sensor fabrication with the hydrophobic barriers formation together with the photograph of paper-based sensor photograph of the Colorimetric assays of h-WO_3 nanoparticles at different concentrations, and (b) RGB analyses of *h*-WO*3* nanoparticles at 15 g/L in contact with *Geobacter sulfurreducens* cells, with the negative control *E. coli* and a blank test [262]. Reproduced with permission of *Springer Nature* (2018).

Righettoni *et al.* [344] reported Si:WO_3 sensors for highly selective detection of acetone for easy diagnosis of diabetes by breath analysis. The biosensor was able to detect low acetone concentrations (down to 20 ppb) with high signal-to-noise ratio in ideal (dry air) and realistic (up to 90 % RH) conditions. At 90 % RH, healthy humans (≤ 900 ppb acetone) and diabetes patients (≥ 1800 ppb) could be distinguished by a gap of 40 % in sensor response. In Ref. [345], 3D graphene network and WO_3 nanowire composites were demonstrated to produce a multifunctional colorimetric and electrochemical biosensing platform. The peroxidase-like activity of composite was investigated to colorimetrically

detect H_2O_2. Moreover, the produced biosensor showed an ultrahigh sensitivity of 1.306 mA mM^{-1} cm^{-2} to dopamine and linear range up to 150 μM, as well as low detection limit (238 nM) and response time (4 s). Li *et al.* [346] reported WO_3-TiO_2 hybrid films prepared on ITO electrodes for multi-functionalized biosensors. Electrochemical oxidation and reduction of of norepinephrine and riboflavin (Vitamin B2) was demonstrated. In another study, an universal photoelectrochemical sensing platform was fabricated based on the composition of protoporphyrin IX, WO_3 and reduced graphene oxide on ITO electrode for detecting cysteine in aqueous solution. The biosensor for detection of cysteine showed linear range of 0.1 to 100 μM and the detection limit was 25 nM [347]. Santos *et al.* [348] reported WO_3 nanoparticle-based conformable pH sensors compatible with wearable biomedical devices, since pH is a vital physiological parameter that can be used for disease diagnosis and treatment as well as in monitoring other biological processes. These sensors showed sensitivity of -56.7 ± 1.3 mV/pH in a wide pH range of 9 to 5.

2.4 Copper oxides

Copper oxides are abundant materials, eco-friendly, non-toxic and are compatible with wet-chemical synthesis routes that originate low-cost devices [11, 349, 350]. The most common copper oxides are copper(I) oxide or cuprous oxide (Cu_2O), reddish material, and copper(II) oxide or cupric oxide (CuO), black material. Both copper oxides are *p*-type semiconductors displaying a bulk direct band gap from 2-2.17 eV in the case of Cu_2O [351, 352] and a narrow bandgap of 1.2 eV (bulk) for CuO, that is controversial regarding being direct or indirect [353, 354]. The *p*-type character of both oxides is usually attributed to the presence of negatively charged Cu vacancies [355-357]. Cu_2O possesses high carrier mobility of about 100 cm^2 $V^{-1}s^{-1}$ at room temperature and long

carrier diffusion length ranging up to several micrometers [358]. Upon photoexcitation, the excitons of Cu_2O are found to be long-lived (10 µs) [351].

Cu_2O crystallizes as in a cubic structure with space group *Pn3m* (224) and lattice parameter of 0.42696 nm [350]. Its unit cell contains six atoms, in which four copper atoms are positioned in a face-centred cubic lattice and the two oxygen atoms forming a body-centred cubic sublattice a face-centered cubic (fcc) sublattice. The oxygen atoms occupy tetrahedral interstitial positions in respect to the copper sublattice, in a way that oxygen is tetrahedrally coordinated by copper, while copper is linearly coordinated by two adjacent oxygens [350, 359]. CuO has a complex monoclinic tenorite crystallographic structure, and it belongs to the *C*2/*c* (15) space group with lattice parameters *a*= 0.46833 nm, *b*= 0.34208 and *c*=0.51294 nm [360, 361]. Each Cu is coordinated to four coplanar O at the corners of a nearly rectangular parallelogram (CuO_4-plaquettes) [362]. The oxygen is coordinated to four Cu at the corners of a distorted tetrahedron. The six nearest O to each Cu complete a strongly distorted octahedron. The CuO_4 parallelograms form ribbons along [110] direction altering to [010] direction. Each ribbon is linked to adjacent chains of other groups by sharing corners [360, 361]. The structure can be considered as being based on two types of zig-zag Cu-O chains running along the [101] and the [10$\bar{1}$] directions [363]. Both copper oxides unit cells are represented in Figure 17.

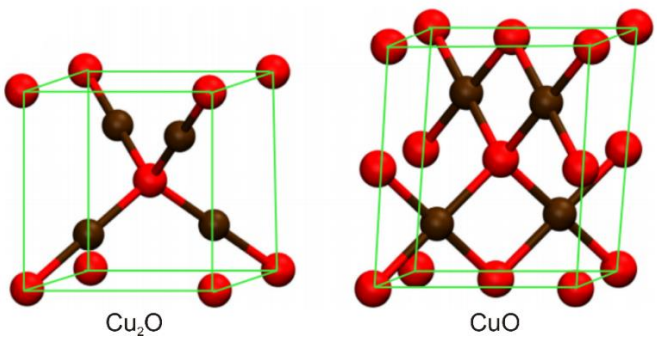

Figure 17. Unit cells of cuprous oxide Cu_2O and cupric oxide CuO [364]. Reproduced with permission of *Elsevier* (2018).

The thermal oxidation of metallic copper into both Cu_2O and CuO has been largely reported [11, 349, 365-371], as copper displays high oxygen affinity [372]. The oxide phase formation starting from copper by thermal oxidation can be described as follows: $Cu \rightarrow Cu + Cu_2O \rightarrow Cu_2O \rightarrow Cu_2O + CuO \rightarrow CuO$. Cu_2O oxidation occurs at temperatures as low as 100 °C [372]. In contrary, CuO formation is slow and is considered a product of Cu_2O oxidation (CuO starts at 300 ºC [373]). Its formation is possible above a certain critical thickness of a Cu_2O layer on the metal surface, thus Cu_2O serves as precursor to CuO [372]. The reactions involved can be summarized as follows [366]:

$$4Cu + O_2 \rightarrow 2Cu_2O \quad (12)$$

$$2Cu_2O + O_2 \rightarrow 4CuO \quad (13)$$

Thermal oxidation of copper, is an attractive technique due to its simplicity, high-quality and low-cost, nevertheless it is a time consuming route [374]. Besides thermal oxidation, several other techniques have been used to produce copper oxides, including hydrothermal synthesis [367, 375], microwave irradiation [376] and microwave oxidation [11], sol-gel method [377, 378], spray pyrolysis [25, 379], electrodeposition [380, 381], sputtering [382, 383], among others.

Several structures at the nano/micrometer scales have been reported for both Cu_2O and CuO materials, such as nanowires [384-386], nanorods [387, 388], nanobelts [389, 390], nanowhiskers [391, 392], nanocubes [55, 393, 394], octahedral nanostructures [395, 396], nanospheres [349, 397-400], hierarchical nanostructures [401], and others (Figure 18).

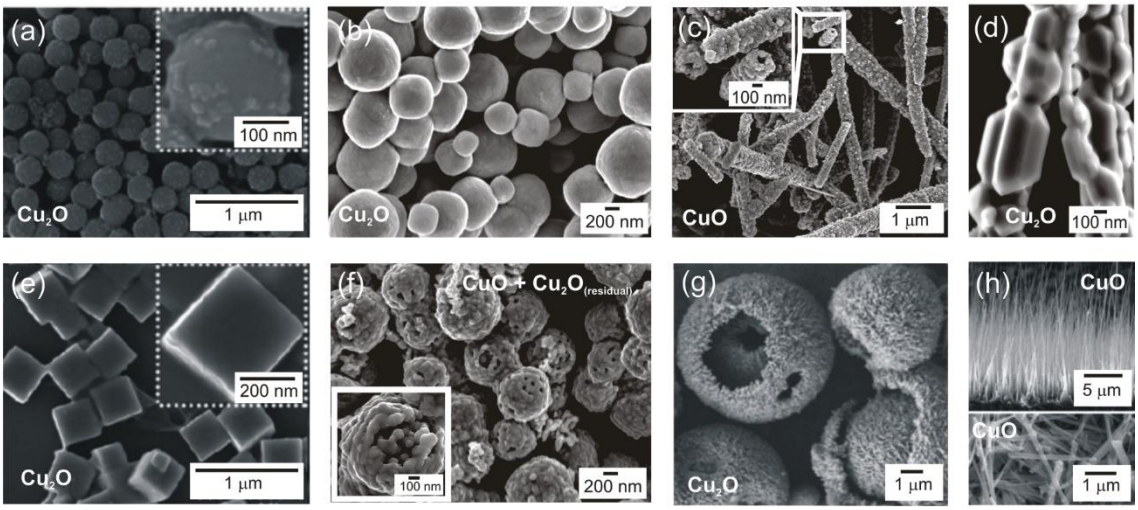

Figure 18. SEM images of Cu_2O spheres in (a) [55] and (b) [349], (c) CuO nanotubes, (d) Cu_2O nanowires [11], (e) Cu_2O nanocubes, (f) CuO nanospheres [349], (g) hierarchical hollow Cu_2O microspheres [401] (h) CuO nanowires [386]. Reproduced with permission of *Royal Society of Chemistry* [55] and [11], *Materials Research Society* [349], *John Wiley and Sons* [401], and *Elsevier* (2018) [386].

Cu_2O and CuO have been proposed for several applications over the years, including photocatalysis [402, 403], solar cells [404, 405], electrodes in lithium ion batteries [406, 407], thin-film transistors [368], sensors [375, 408, 409], among others. With emphasis to the latter application, integration of both materials in sensors has been extensively investigated over the years, due to their intrinsic *p*-type properties [410]. The application of Cu_2O in gas sensors is much less studied than for CuO [55]. Cu_2O nanowires were tested as gas sensors towards H_2, showing a response of 33.3 % and recovery time of ~10 min [411]. Tang *et al.* [412] reported on the gas sensing performance of Cu_2O nanocages towards gasoline. In another study, sensitivity of hierarchical Cu_2O microspheres toward 100 ppm ethanol was estimated to be 8.2, which is much higher than the value of 1.5 measured for solid Cu_2O microspheres [401]. The gas sensitivity of Cu_2O nanocubes and nanospheres were tested for ethanol vapor, with clear sensitivity differences regarding particle size and morphology [55]. Sensors based on Cu_2O films have also been reported, demonstrating high sensitivity, fast response time, and fast recovery time for methane gas at an operation temperature as low as 180 °C. At a 2.5 %

CH_4 concentration, the films demonstrated sensitivity around 70 %. The fast and high response of Cu_2O sensor for methane was justified by the increase of resistance in intrinsic *p*-type Cu_2O in the presence of methane gas [413].

CuO nanostructures have been integrated in gas sensors for detection of a variety of reducing as well as oxidizing gases including acetone, ethanol, propanol, H_2S, CO, O_3, NO_x, methanol, formaldehyde, H_2, toluene and ammonia [414]. Kim *et al.* [386] reported CuO nanowire gas sensors for air quality control in automotive cabin, showing a resistance decrease upon exposure to 30–100 ppm NO_2, and increase upon contact with ≤ 5 ppm NO_2. Yang *et al.* [415] reported on the synthesis of CuO 3D flower- and 2D branching sheet-like CuO nanostructures exhibiting an enhanced gas response to the five gases. At 1000 ppm, the CuO flower sensor demonstrated responses to ethyl-acetate (4.6), ethanol (4.0), acetone (3.8), xylene (3.6) and toluene (2.8). The sheet-like structures resulted in lower responses. The gas-sensing mechanism of *p*-type CuO semiconductor was explained by the change in resistance caused by the adsorption/desorption and reactions of gas molecules at the semiconductor surface. In another study, CuO nanoparticles were used for ethanol sensing showing fast response and recovery times below 10 s and responses greater than 2.3 at 100 ppm of ethanol at 200 °C (Figure 19 (a)) [416]. Flower-like CuO nanostructures with porous nanosheets demonstrated good H_2S gas sensing performance with maximum responses between 2.10 and 2.15 for five consecutive sensing cycles at 1 ppm, showing good reproducibility. The flower-like CuO nanostructured sensor was exposed to other types of gases (NO_2, H_2, CO, C_2H_5OH and NH_3) and for 100 ppm of NH_3, the sensor showed a response sensitivity of 1.42 [417]. CuO nanowires were integrated as ethanol gas sensors, showing responses of 1.06, 1.11, 1.14, 1.18, 1.24, and 1.27 for ethanol gas concentration of 25, 50, 100, 200, 500,

and 1000 ppm, respectively [418]. CuO wormlike structures were also tested as gas sensors towards ethanol [419].

When it comes to gas sensors with films, Choi *et al.* [420] reported on the direct printing synthesis of CuO hollow spheres to form a film. This film based on CuO hollow spheres exhibited a high, stable response of ~2 to H_2S, while for C_2H_5OH, the response was ~3, which was 2 times higher than that (~1.5) of CuO powder. CuO thin films were also reported for gas sensing applications. The gas sensitivity was demonstrated to increase up to 5.1 in the presence of CO_2 gas at 160 °C, while in the presence of N_2 gas, it reached only 1.43 even at 200 °C [421].

It has also been reported combinations of metal oxide materials to obtain a *p*-/*n*-heterojunction. In Ref. [422], flower-like *p*-CuO/*n*-ZnO nanorods heterojunction was produced showing response of 98.8to 100 ppm ethanol, which was 2.5 times that of ZnO material, with response and recovery time of 7 s and 9 s, respectively. Good selectivity and long-term stability were also reported with response to low concentration of ethanol (1 ppm) of 9.68 using the flower-like *p*-CuO/*n*-ZnO heterojunction nanorods. In another study, sensors based on ZnO/CuO nanostructures were tested as gas sensors and had investigated their H_2S-sensing properties, with sensor response of 2.7, and response time within 37 s [423]. CuO-MnO_2 nanocomposites were also reported, with response time of 120 s and recovery within 600 s [424]. Sensors based on mixtures of Cu_2O and CuO has also been reported. Meng *et al.* [425] showed Cu_2O/CuO sub-microsphere based sensors with responses up to 2.1–50 ppb of H_2S gas at 95 °C, with recovery time of about 76 s. Zhou *et al.* [426] reported porous Cu_2O/CuO cubes with enhanced gas sensing properties. For acetone concentrations of 50, 100, 200, 400, 500 ppm, the obtained responses were 3.0, 4.4, 6.5, 9.0 and 9.9, respectively. Cu_2O and

CuO were also mixed with metal nanoparticles, forming a hierarchical hollow nanostructure that was applied for CO sensing [427].

The mixture of copper oxides to carbon-based materials has also been addressed. In Ref. [428], CuO-reduced graphene oxide sandwiched nanostructure was investigated to determine its hydrogen sensing characteristics. In another study, reduced graphene oxide conjugated Cu_2O nanowire mesocrystals demonstrated higher sensitivity toward NO_2 at room temperature, surpassing the performance of Cu_2O nanowires networks and rGO sheets. This composite showed sensitivity of 67.8 % at 2 ppm and calculated limits of detection of 82 ppb [429].

Humidity-sensing studies of *p*-type semiconducting materials are scarce. Hsueh *et al*. [430] reported on the fabrication of humidity sensors by growing CuO nanowires on glass substrates. These sensors demonstrated that resistance of the CuO nanowires increased with the increase of relative humidity (52-90 %) due to the *p*-type nature of CuO. In another study, nanostructured Cu_2O porous films were exposed to humidity. The increase of resistance with increasing RH values is a characteristic response of *p*-type metal oxides, in which holes are the majority charge carriers. Up to 48 %RH , the linear increase of response percentage has been reported. The average response and recovery time evaluated for low RH were 151±6 and 145±18 s, respectively, with a maximum rate of 4.38±0.16%/RH [431]. Wang *et al.* [432] reported on CuO nanowire humidity sensors, that show steady state currents of about 2.44, 2.32, 2.23, and 2.15 μAwhen measured with 20, 40, 60, and 80 % relative humidity, respectively.

A blend of Cu_2O nanopowder and poly-N-epoxypropylcarbazole was also tested as humidity sensor, with an abrupt decrease of resistance at 30 % RH [433]. In another study, the electronic conduction and capacitance of an Au/CuO/Cu_2O/Cu sandwich structure was investigated and revealed to be dependent on humidity [434]. Yuan *et al.* [435]

reported highly sensitive humidity sensors based on CuO inorganic-organic hybrid nanowires. Ref. [436] showed an urchinlike CuO modified by rGO composite that was integrated in humidity sensors revealing much higher impedance than pure CuO (Figure 19 (b)). The mixture of metal oxides was also investigated, in which moisture sensing of Cu_2O doped ZnO nanocomposites was reported by Pandey *et al.* [437], with the response and recovery time of this material shown to be 76 and 296 s, respectively.

Copper oxides based UV/near-UV sensors have also been reported, but in this case composing a heterojunction to enhance their performance due to an additional charge separation effect [438]. Wang and Cho [438] reported *p*-CuO nanowire/*n*-ZnO nanosheet heterojunctions and its application for near-ultraviolet light detection. Under different illumination conditions, the photocurrent detection limit was around 16.8 mW mm^{-2}. Hong *et al.* [439] demonstrated n-silicon nanowire arrays with a layer of CuO nanoflakes to be applied as photodetectors/sensors highly sensitive to visible and near-infrared light irradiation. The photocurrent obtained for this device was 0.96 μA at 0.48 W cm^{-2} for a 405 nm laser, 4.41 μA at 5 W cm^{-2} for a 532 nm laser and 4.92 μA at 5.5 W cm^{-2} for a 1064 nm laser (Figure 19 (c)). In another study, CuO nanowires were used to produce a *p*-CuO/*n*-ZnO heterojunction nanostructured photodetector/UV sensor. The responsivity was reported to be 0.040 A W^{-1} for 350 nm and an applied bias of 1 V and for a 2 V bias it increased to 0.123 A W^{-1} [440]. Ok *et al.* [441] demonstrated UV photodetectors/sensors based on *p*-Cu_2O thin film and *n*-ZnO nanowires for formation of a *p–n* heterojunction. These named all-oxide UV devices resulted in a responsivity of ~ 50 A W^{-1} at 360 nm.

Several studies reported the integration of copper oxides in biosensors [442-446]. Liu *et al.* [442] reported a sensor for the detection of glucose and hydrogen peroxide based on Cu_2O nanocubes wrapped by graphene nanosheets. A linear response over glucose

concentration range of 0.3 to 3.3 mM was reported, with a detection limit of 3.3 μM, high selectivity and short response time (< 9 s). The enzymeless sensor also exhibited good response toward H_2O_2, with the linear response ranging from 0.3 to 7.8 mM at −0.4 V and detection limit of 20.8 μM. Cu_2O shuriken-like nanostructures produced by hydrothermal synthesis were tested as nonenzymatic glucose biosensors. The glucose sensors exhibited wide linear detection range (from 0.01 μM to 11.0 mM), ultra-low detection limit (0.035 μM) and high sensitivity (0.933 mA mM^{-1} cm^{-2}) [444]. In another study, carbon quantum dots/octahedral Cu_2O nanocomposites were tested as non-enzymatic glucose and hydrogen peroxide amperometric sensors. Amperometric sensing of glucose was realized with linear response range from 0.02 to 4.3 mM and showed a detection limit of 8.4 μM. The nonenzymatic sensor revealed an electrocatalytic reduction of H_2O_2 with linear response range from 5 μM to 5.3 mM and detection limit of 2.8 μM [447]. Ref. [446] showed leaf-like CuO nanoparticles for detecting glucose. This sensor exhibited high sensitivity (246 mA mM^{-1} cm^{-2}), short response time (within 5 s), linear dynamic range of 1.0 to 170 mM and low limit of detection (0.91 mM). In Ref. [448], CuO nanotube arrays were used as biosensors for glucose detection showing sensitivity of 1.89 mA mM^{-1} cm^{-2} and linear range from 5 μM to 3.0 mM.

Copper oxides were also tested as biosensors in film form. Inkjet-printed CuO nanoparticles to produce films were integrated in nonenzymatic glucose biosensors. The sensors showed high and reproducible sensitivity of 2762.5 μAm M^{-1} cm^{-2} with wide linear-detecting range of 0.05−18.45 mM and detection limit of ~0.5 μM [449]. A nonenzymatic glucose biosensor based on printed CuO nanoparticles film was also demonstrated in [450]. The biosensor showed linear response toward glucose in the range of 0.1 to 6.5 mM at a lower detection limit of 0.5 μM glucose. CuO thin film based uric acid biosensor has been reported to have good linearity over a wide uric acid

concentration range of 0.05 mM to 1.0 mM with enhanced response of 2.7 mA mM^{-1} and long shelf life (> 14 weeks) [445].

Two metal oxides were also employed in biosensors. In Ref. [451], a ZnO–CuO composite matrix based biosensor was demonstrated for detection of total cholesterol, for which sensitivity was reported to be 680 µA mM^{-1} cm^{-2} and 760 µA mM^{-1} cm^{-2} towards free cholesterol and total cholesterol respectively with response time of 5 s, with long shelf life. Vertically-aligned ZnO nanorods decorated with CuO were produced and integrated in high-performance nonenzymatic glucose sensors. The fabricated electrodes exhibited high sensitivity (2961.7 µA mM^{-1} cm^{-2}), linear range up to 8.45 mM, low limit of detection (0.40 µM) and short response time < 2 s (Figure 19 (d)) [443].

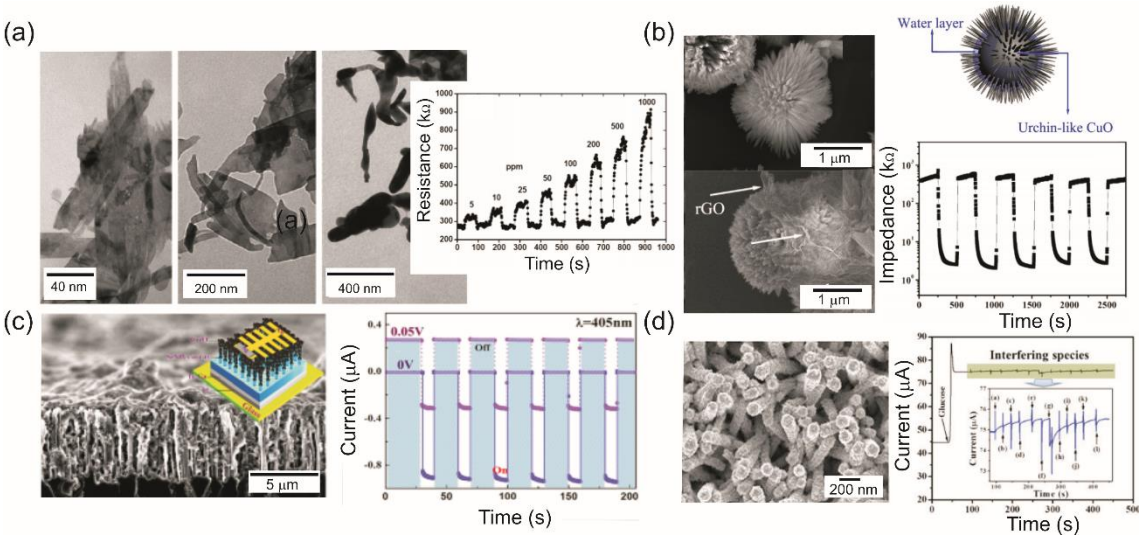

Figure 19. (a) TEM images of CuO nanoparticles for ethanol gas sensing [416], (b) SEM images of CuO/rGO composites for humidity sensors [436]. (c) *p–n* Heterojunctions of CuO/Si Nanowire Array to be used as photodectors/UV sensors [439]. (d) CuO modified ZnO nanorods to produce highly efficient non-enzymatic glucose sensors [443]. The graphs represent the sensors' response, resistance, current and impedance variations. Reproduced with permission of *ACS publications "Copyright (2019) American Chemical Society"* [416], *"Copyright (2018) American Chemical Society"* [436] and [439], and *Springer Nature* (2018) [443].

2.5 Tin oxide

There are two well-known tin oxide compounds, *i.e.* tin (IV) oxide or stannic oxide (SnO_2) and tin (II) monoxide or stannous oxide (SnO). SnO_2 is a *n*-type semiconductor, with a wide energy band gap ($Eg \sim 3.6$ eV for bulk at room temperature). SnO_2 has a tetragonal structure ($a= b= 0.4737$ nm and $c= 0.3186$ nm), similar to the rutile structure [452, 453] with space group $P4_2/mnm$ (136) [454]. SnO is a *p*-type semiconductor with a direct band gap of 2.5-3.0 eV and an indirect band gap of 0.5-0.7 eV [455-458]. The origin of *p*-type conductivity of SnO is mainly attributed to Sn vacancies and O interstitials [355]. Moreover, the native *p*-type character of SnO has been reported to result in more effective hole transport path and higher hole mobility due to the closer position of Sn-5s and O-2p components [458, 459]. SnO also has tetragonal structure ($a=b= 0.37986$ nm, $c= 0.48408$ nm) with space group $P4/nmm$ (129) [460].

The SnO_2 unit cell consists of two metal atoms and four oxygen atoms. Each Sn atom is placed at the center of six O atoms, nearly forming the corners of a regular octahedron. Oxygen atoms are surrounded by three Sn atoms that approximate the corners of an equilateral triangle [461]. In the case of SnO, this material has a layered structure with Sn-O-Sn layered pyramids, where oxygen atoms are tetrahedrally bonded to tin atoms. The Sn atoms are situated at the apex of regular square-based pyramids that are based on O atoms [355]. The unit cells of tetragonal SnO_2 and SnO are represented in Figure 20.

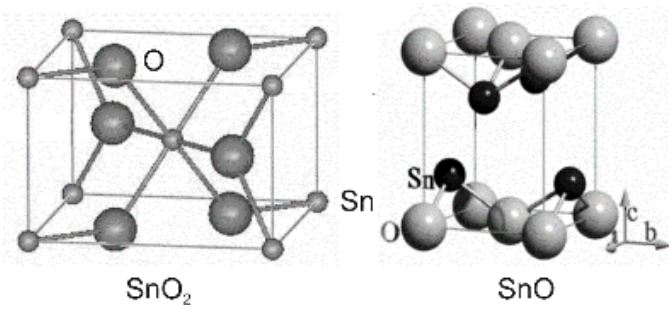

Figure 20. Unit cells of both SnO_2 [462] and SnO [463]. Reproduced with permission of *MDPI* [462] and *APS Physics* (2018) [463].

SnO is formed at the initial stage of Sn oxidation and it is a metastable phase that converts to SnO_2 even in the absence of oxygen if exposed to a certain temperature. The specific temperature to convert SnO to SnO_2 is unclear, varying from 250 to 600 ºC and depends on several factors, such as deposition method, initial oxygen concentration, annealing temperature and humidity [464]. Nevertheless, it is accepted that SnO is unstable above 270 °C in comparison with SnO_2, which makes it frequently known as precursor or intermediate phase in the production of SnO_2 nanostructures [457].

Several techniques have been reported to yield SnO and SnO_2 nanostructures and thin films, including hydrothermal synthesis [465-467], microwave irradiation [468, 469], precipitation method [470, 471], sol-gel technique [472-474], rf magnetron sputtering [475, 476], spray pyrolysis [477, 478], among others. SnO_2-doped material plays an important role as transparent conductive oxide material with remarkable electrical and optical properties in the form of thin films [453]. Antimony, indium and fluorine are examples of doping elements. The electrical properties of the SnO_2 films are critically depend upon its oxygen stoichiometry [477]. When passing to nanostructures, several nano- and microstructures have been reported for both SnO and SnO_2, such as nanoparticles [479, 480], nanorods [468, 481], nanobelts [482, 483], nanowhiskers [484, 485], nanowires [486-488], nanoflowers [489, 490], spheres [491, 492], among others.

Both SnO and SnO_2 have been used in numerous applications, such as thin film transistors [475], anodes for Li-ion batteries [493-495], water splitting for production of hydrogen [496], photocatalysis [497, 498] and sensors. In the latter application, SnO_2 has been extensively applied, with emphasis on gas sensing. In fact, SnO_2 is one of the most used materials as gas sensors [499]. Several SnO_2 nanostructures have been investigated for the detection of different gases, such as ethanol, H_2, O_2, CO, NO, NO_2 and NH_3 at moderate temperature, due to its fast-response speed, high exciton binding energy, high

chemical stability, prominent selectivity, and low cost [500-503]. In Ref. [503], it has been shown ethanol gas sensors based on nanosheets-assembled SnO_2 hollow spheres showing responses from 2.4 to 23.5 for 10–500 ppm ethanol, and at the ppb level, showed a response of 1.1 toward 500 ppb of ethanol. The sensor response time was about 5 s (Figures 21 (a) and (b)). SnO_2 nanoparticles were also produced using the hydrothermal synthesis with conventional oven (Figure 21 (c)). Huang *et al.* [504] reported porous flower-like SnO_2 nanostructures for gas sensors (Figure 21 (d)). The sensor responses to 100 ppm ethanol and n-butanol were 42.6 and 77.2, respectively, at a working temperature of 240 °C. In addition, these sensors also exhibited a good response to methanol, 2-propanol, and acetone. Ref. [497] demonstrated hierarchical SnO_2 based ultrathin nanosheets that were tested as gas sensors for ethanol, ammonia, benzene, acetone, toluene, methanol and diethyl ether. The sensor sensitivity to 5 ppm ethanol is around 5.13 which increases to 183.8 for 500 ppm ethanol. The response and recovery time of hierarchical nanostructures to 100 ppm of ethanol were 1 and 2 s, respectively. The responses of this sensor to eight gases were also compared and the largest response was observed only for ethanol with a value of up to 44.7, implying good selectivity of the sensor for ethanol (Figure 21 (e)). In another study, square-shaped SnO_2 nanowires forming a sphere-like superstructure were tested as gas sensors. These sensors showed sensitivity of 5.5 for acetone concentration as low as 20 ppm, and the response and recovery times were 7 and 10 s, respectively [505]. SnO_2 nanorod sensors were also reported in Ref. [506] exhibiting sensitivity of 31.4 for 300 ppm of ethanol with both response and recovery time around 1 s. Liu *et al.* [507] reported tubular SnO_2 nanomembranes fabricated by rolled-up technology. The sensor exhibited a highly stable response to acetone detection at 20 ppm. Kuang *et al.* [508] reported hierarchical SnO_2 nanostructures composed of numerous one-dimensional nanorods and tested as gas

sensors. The responses of sensors with six different ethanol concentrations (5, 10, 25, 50, 75 and 100 ppm) were 7, 13, 32, 44, 59 and 72, respectively (Figure 21 (f)).

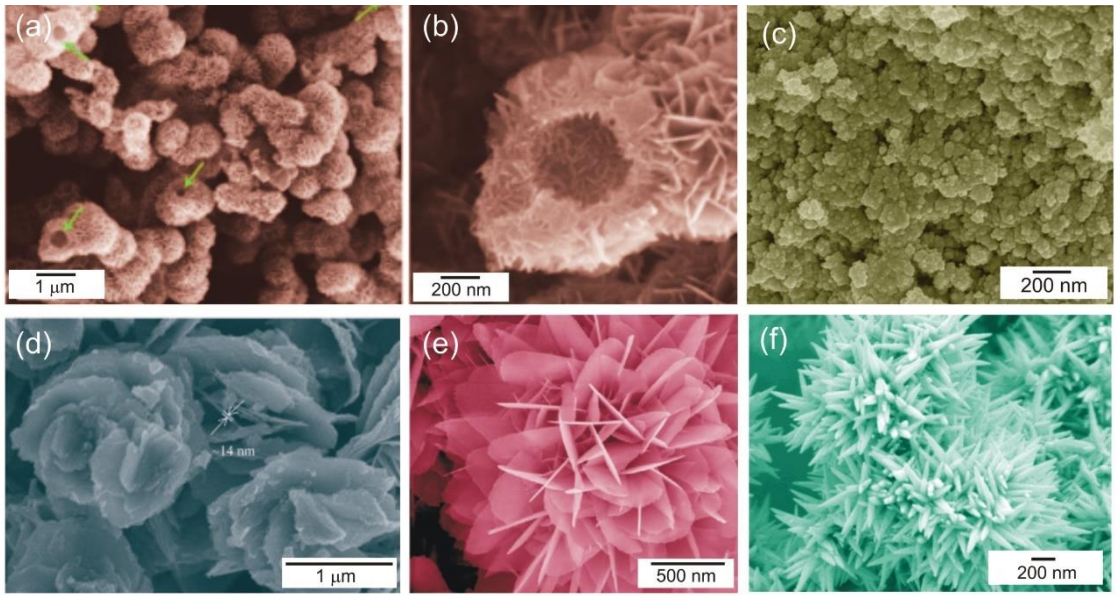

Figure 21. SEM images of (a-b) nanosheets-assembled SnO_2 hollow spheres for ethanol gas sensor [503], (c) SnO_2 nanoparticles produced at CENIMAT using hydrothermal synthesis, (d) porous flower-shaped SnO_2 nanostructures [504], (e) hierarchical SnO_2 based ultrathin nanosheets [497], and (f) hierarchical SnO_2 nanostructures made of superfine nanorods [508]. Reproduced with permission of *Elsevier* [503], [504] and [508] and *ACS publications "Copyright (2018) American Chemical Society"* [497],

Choi *et al.* [509] reported a SnO_2 nanowire-based gas sensor for detecting NO_2. The sensitivity was determined to be 18 and 180 when NO_2 concentration was 0.5 and 5 ppm, respectively (at 200 ºC). Suman *et al.* [510] reported a sensor based on SnO micro-disks, showing a response of ~13 to 100 ppb of NO_2, and selectivity against potential interferent gases such as H_2, CO and CH_4 was also demonstrated. In another study, SnO, SnO_2 and Sn_3O_4 nanobelts had their efficiency as gas sensors compared. SnO and Sn_3O_4 exhibited higher sensitivity and selectivity relative to potential interferent gases (H_2, CO and CH_4) than SnO_2 nanobelts (Figure 22 (a)) [511].

Doping elements, such as, Ag, Au, Pd, Pt, and other metal oxides are used to enhance the sensing properties, such as, sensitivity, response time and reproducibility for

a specific gas [502]. Kolmakov *et al.* [486] reported the sensing ability toward oxygen and hydrogen of individual SnO_2 nanowires and nanobelts before and after functionalization with Pd catalyst particles. Sb-doped SnO_2 nanowires were tested as gas sensors and resulted in sensitivity of 1.76 upon exposure to 10 ppm ethanol and recovery time of about 5 s [512]. Reduced graphene oxide was also explored with tin oxides for gas sensors. Wei *et al.* [513] reported the gas-sensing of a silver-decorated tin oxide/reduced graphene oxide (Ag/SnO_2/rGO) composite with a sensitivity to 400 ppm ethanol of 95.3 at optimum operating temperature (280 °C). The SnO_2/rGO sensor was also tested demonstrating a lower sensitivity of 55.3. A hierarchical SnO_2/rGO nanostructure was described in Ref. [514], with sensitivity of 78 to 10 ppm H_2S at 100 °C and response time of 7 s. NH_3 gas sensors based on Pd, SnO_2 and rGO ternary nanocomposite was demonstrated in Ref. [515], with response and recovery time of 7 and 50 min, respectively, at NH_3 testing concentration of 100 ppm.

The combination of different metal oxides has also been widely addressed in gas sensing. Core-shell WO_3-SnO_2 nanofibers have been synthesized via a coaxial electrospinning approach. The sensors exhibited good response to ethanol (5.09 at 10 ppm) and short response/recovery time (18.5 s and 282 s) [516]. A sensor based on ZnO/SnO_2 composites with a hollow nanostructure was reported in Ref. [517]. The sensitivity to 30 ppm ethanol was shown to be 34.8, which was about seven times higher than the sensor based on pristine SnO_2 hollow spheres (the response was 5.1). The sensor exhibited response to ppb-level ethanol and response time was 1 s. In another study, gas sensors fabricated from SnO_2-SnO nanocomposite with *p-n* heterojunctions exhibited an enhanced sensing performance for NO_2 gas detection, with limit of detection and sensitivity of 0.1 ppm and 0.26 ppm^{-1}, respectively [518]. Another *p-n* heterojunction was demonstrated with CuO–SnO_2 gas sensors for CO gas [519]. A sensor based on a

hierarchical CoO/SnO_2 heterojunction demonstrated response up to 145 when exposed to 100 ppm ethanol gas. This sensor was demonstrated to be effectively higher when compared to SnO_2 only sensors (13.5 for SnO_2) [520]. Gas sensors based on SnO_2-decorated NiO nanostructures demonstrated excellent sensitivity and selectivity towards toluene, with response of 66.2-100 ppm, which was 50 times higher than that of pure NiO nanospheres (1.3-100 ppm). Additionally, the sensor had surpassingly low detection limit (ppb-level), showing response of 1.2-10 ppb toluene [521].

Similarly to copper oxides, integration of *p*-type materials, *i.e.* SnO, in humidity sensors is diminished. However, as observed for gas sensors, there are several studies demonstrating the use of SnO_2 in such sensors. Parthibavarman *et al.* [522] reported humidity sensors based on SnO_2 nanoparticles produced under microwave irradiation. This sensor showed fast response time (32 s) and recovery time (25 s) with relative humidity range of 5-95% in air at room temperature. Kuang *et al.* [92] reported the production of SnO_2 humidity nanodevice using a single SnO_2 nanowire as the sensing unit. The response time and recovery time of this sensor was 120-170 and 20-60 s, respectively. Ordered SnO_2 nanostructures were used as humidity sensors, showing a response and recovery time of 32 s and 42 s for 11-96 % RH, respectively. The hysteresis for the SnO_2 nanostructured sensor was < 5 % [523]. SnO_2 and Li^+-doped SnO_2 porous nanofibers were fabricated via electrospinning and tested as humidity sensors. The doped materials demonstrated better performance than the SnO_2 nanofiber-based sensor, in which an ultrafast response and recovery time within 1 s has been reported for the doped-sensor at a relative humidity level of 85 % [524]. Another study described humidity sensors based on ion-doped SnO_2 nanofibers (KCl) developed by screen-printing. It has been shown that impedance of the sensor decreased by more than five orders of magnitude

with increasing relative humidity from 11 % to 95 %, with response and recovery time of 5 and 6 s, respectively [525].

Several studies also demonstrated humidity sensors based on different metal oxides. In Ref. [526], SnO_2/ZnO heterojunction nanostructured films demonstrated remarkable humidity-sensing performance exhibiting sensitivity of 90.56 to humidity. Nanostructured TiO_2–SnO_2 thin films produced by sol–gel process showed over three orders change in the resistance during relative humidity variation from 20 to 90 % [527]. Hybrid nanomaterials have also been described. Zhang *et al.* [528] reported a MoS_2/SnO_2 hybrid film sensor with ultrafast response/recovery behaviours. Three distinct nanocomposites based on SnO_2-CuO, SnO_2-Fe_2O_3 and SnO_2-SbO_2 and their humidity sensing performance were described in Ref. [529]. It has been shown that when relative humidity increases, the resistance of the nanomaterials decreases. of Amongst all other composites, SnO_2-SbO_2 showed maximum sensitivity for humidity (12 MΩ/%RH). Humidity sensors based on reduced graphene oxide and tin oxide (rGO-SnO_2) nanocomposites were also reported [530]. These sensors demonstrated stability over 30 days at 95 % RH (Figure 22 (b)).

As SnO_2 is wide bandgap material with consequent transparency in the visible spectral region, it has been reported for UV sensing. Huang *et al.* [72] reported single-crystalline SnO_2 nanobelt with amorphous embedded Sn nanodots , to produce an individual nanobelt-based UV photodetector/sensor. The responsivity value of the nanobelt photodetector excited by 300 nm-light was 56 A W^{-1}. This sensor also demonstrated high external quantum efficiency (EQE) (~ 2.3×10^4), fast response time (less than 0.3 s) and high on/off current ratio (~ 2.75×10^3). The photoresponse of SnO_2 nanobelts has been investigated under UV light in Ref. [531], and shown that the source–drain current increased to ~ 80 μA in air and up to ~ 900 μA in vacuum, demonstrating SnO_2 nanobelts

potentialities as UV sensors. SnO_2 nanowires were tested as UV photodetectors in [532], with the photoelectric current exhibiting rapid photo-response as an UV lamp was switched on and off. In another study, photodetectors based on thin SnO_2 nanowires have been reported. These exhibited excellent light selectivity and stability and high EQE value of 1.32×10^7 [533]. SnO_2 hollow nanospheres have been used as an active material to fabricate UV photodetectors. The UV sensor exhibited peak UV responsivity of 2680 A W^{-1} and high external quantum efficiency of 9.8×10^5 % [534]. Lu *et al.* [535] reported ultrahigh gain in photodetectors based on single SnO_2 nanowires with ferromagnetic Ni electrodes.

SnO_2 has been also combined with other metal oxides to produce UV photodetectors/sensors. Xie *et al.* [536] reported UV photodetectors based on CuO/SnO_2 *p-n* nanoscale heterojunctions. The responsivity for the single SnO_2 nanodevice was 1.9 A W^{-1} while for the *p-n* heterojunction it was 10.3 A W^{-1}. The wavelength-dependent photocurrent-to-dark current ratio was estimated to be ~592 for the CuO/SnO_2 photodetector at 290 nm. ZnO-SnO_2 nanowire arrays were synthesized by a near-field electrospinning method for flexible ultraviolet photodetectors application. These sensors exhibited excellent photoresponse properties to 300 nm ultraviolet light illumination including high I_{on}/I_{off} ratios (up to 10^3), good stability and reproducibility [537]. Another work described fully transparent photodetectors produced from electrospun ZnO-SnO_2 heterojunction nanofibers. This photodetector exhibited excellent operating characteristics, including high UV-sensitivity and photo-dark current ratio, and fast response speed [538]. TiO_2/SnO_2 branched heterojunction nanostructures with TiO_2 branches on electrospun SnO_2 nanofiber were developed for self-powered UV photodetector. Under UV irradiation, the self-powered UV photodetector exhibited responsivity of 0.6 A W^{-1}, high on/off ratio of 4550, rise time of 0.03 s and decay time of

0.01 s [539]. SnO_2 nanosheet films with branched TiO_2 nanoneedles on SnO_2 nanosheets, forming a heterojunction core–shell structure have been used to integrate UV photodetectors/sensors. These UV photodetectors showed responsivity of 0.6 A W^{-1}, high on/off ratio (440,563%), fast response for rise time 0.02 s and decay time 0.004 s [540]. A self-powered UV photodetector based on TiO_2 coated SnO_2 mesoporous spheres has been described in Ref. [541]. Under UV irradiation, this sensor displayed high on/off ratio of 11519, fast rise time of 0.007 s and decay time of 0.006 s.

Tin oxides are also largely present in biosensors. In Ref. [542], SnO_2 nanorod arrays have been tested as H_2O_2 biosensors. This sensor demonstrated sensitivity of 379 μA mM^{-1} cm^{-2}, low detection limit (0.2 μM) and high selectivity with apparent Michaelis–Menten constant estimated to be as small as 33.9 μM. Nanostructured SnO_2 thin films were presented as glucose sensors. These sensors exhibited higher response, fast rise time 8 s and suitable recovery time 53 s upon working at room temperature with a glucose concentration between 50-200 mg L^{-1} [543].

As mentioned previously, tin oxides have been doped or combined with other elements or metal oxide materials, including for biosensing. A mediator-free horseradish peroxidase-based H_2O_2 biosensor was constructed with Sb-doped SnO_2 nanowires as immobilization matrix for enzymes. The sensor showed sensitivity of 100 mA M^{-1} cm^{-2}, and detection limit of 0.8 μM at a signal-to-noise ratio of 3. The Michaelis–Menten constant was calculated to be 0.76 mM and the sensor demonstrated long-term stability [544]. Hydrogen peroxide biosensors based on Ni doped SnO_2 nanoparticles has been reported [545]. A horseradish peroxidase/Ni-SnO_2 nanocomposite has been studied exhibiting a linearity range from 1.0×10^{-7} to 3.0×10^{-4} M with detection limit of 43 nM. The apparent Michaelis–Menten constant of horseradish peroxidase on the nano-Ni–SnO_2 was estimated as 0.221 mM. Cr-doped SnO_2 nanoparticles based biosensors for

selective determination of riboflavin in pharmaceuticals has been described in [546]. This sensor responded linearly to riboflavin over a concentration range of 0.2×10^{-6} to 1.0×10^{-4} M with detection limit of 107 nM. Shen *et al.* [547] reported the synthesis of Au-SnO_2 hybrid nanospheres with enhanced photoelectrochemical biosensing performance. The biosensor displayed suitable analytical performance for detection of cysteine with a broad linear range (from 0.4 mM to 12 mM) and low detection limit (0.1 mM). In Ref. [548], ZnO/SnO_2 heterostructured nanomaterials were explored to build a biosensing platform for detecting H_2O_2 by immobilizing hemoglobin with chitosan. The biosensor sensitivity was 52.8 mA cm^{-2} M^{-1}, with linear range from 2.0×10^{-6} to 3.7×10^{-4} M. The detection limit of H_2O_2 was 4.6×10^{-7} M when signal-to-noise ratio was 3.

The incorporation of carbon-based materials in tin oxides for biosensing has also been investigated. Zhu *et al.* [549] reported graphene/SnO_2 composite nanosheets loaded with noble metal nanoparticles to be applied as biosensors for nonenzymatic glucose detection. The amperometric response has been shown to be linear for glucose concentrations ranging from 2 to 20 mM with sensitivity of 20.3 μA mM^{-1}. Multiwalled carbon nanotubes-SnO_2-Au composite was tested as glucose biosensor by absorbing glucose oxidase on the hybrid material. The glucose biosensor demonstrated linear range from 4.0 to 24.0 mM, high stability with its voltammetric response remaining stable after 50 cycles [550]. A sensitive amperometric acetylcholinesterase biosensor, based on SnO_2 nanoparticles, carboxylic graphene and nafion for the detection of methyl parathion and carbofuran has been developed in Ref. [551]. The biosensor showed favourable affinity to acetylthiocholine chloride with an apparent Michaelis-Menten constant of 131μM, detecting methyl parathion in a linear range from 10^{-13} to 10^{-10} M and from 10^{-10} to 10^{-8} M. This device detected carbofuran in a linear range from 10^{-12} to 10^{-10} M and from 10^{-10} to 10^{-8} M. The detection limits of methyl parathion and carbofuran were 5×10^{-14} M and

5×10^{-13} M, respectively. Another study demonstrated amperometric acetylcholinesterase biosensors based on a nanocomposite of multi-walled carbon nanotubes, SnO_2 nanoparticles and chitosan. These biosensors exhibited a wide linear range from 0.05 to 1.0×10^5 μg/L with detection limit for chlorpyrifos of 0.05 μg/L. Based on the inhibition of pesticides, using chlorpyrifos as model pesticide, the biosensor exhibited a wide range, low detection limit, good reproducibility, and high stability. Using cabbages, lettuces, leeks and pakchois, acceptable recovery of 98.7–105.2 % was reported [552]. In Ref. [553], a carboxylated multiwalled carbon nanotubes–SnO_2 nanoparticles–graphene–chitosan composite was demonstrated as an amperometric biosensor (Figure 22 (d)). Lysine oxidase enzyme was immobilized covalently on the surface of the composite. The biosensor exhibited wide linear range (9.9×10^{-7} M–1.6×10^{-4} M), low detection limit (1.5×10^{-7} M), high sensitivity (55.20 μA mM^{-1} cm^{-2}) and fast amperometric response (< 25 s).

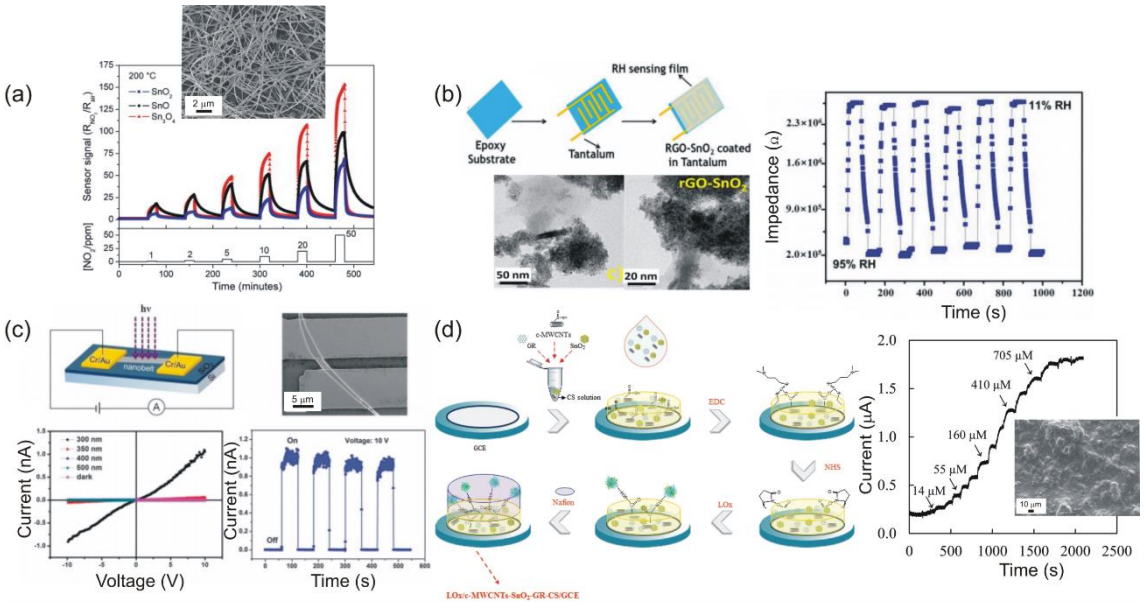

Figure 22. (a) SEM image of SnO_2 nanobelts. The graph showed the sensitivities of the gas sensor under exposure to NO_2, with concentrations ranging from 1 to 50 ppm of NO_2 [511]. (b) Schematic diagram of the rGO-SnO_2 humidity sensor [530], and the nanocomposite morphology. The graph shows the long-term stability of the rGO-SnO_2 sensor after being exposed to 95 % RH for 30 days. (c) Schematic illustration of a Sn-embedded SnO_2 nanobelt photodetector, and corresponding SEM image. The *I-V* curves of the photodetector exposed to light with different wavelengths and under dark conditions, with the time-dependent response of the photodetector [72]. (d) Production scheme of the carboxylated multiwalled carbon nanotubes–SnO_2 nanoparticles–graphene–chitosan composite biosensor together with its current-time response to successive addition of L-lysine into a stirred solution of 0.025 M [553]. Reproduced with permission of *MDPI* [530], *Royal Society of Chemistry* [72], and *Elsevier* (2018) [511] and [553].

2.6 Vanadium oxide

Vanadium oxide is a 3d transition metal compound which may display different valence states, ranging from +II to +V, and form a variety of oxides such as V_2O_5 (orthorhombic phase), V_2O_3 (rhombohedra phase), V_3O_7 (monoclinic phase), V_4O_9 (orthorhombic phase), V_6O_{13} (monoclinic phase) and also VO_2 [554-557].

The allotropic phases of VO_2 systems may include VO_2(R) (tetragonal/rutile phase, $P4_2/mnm$), VO_2(M) (monoclinic phase, $P2_1/c$), VO_2(B) (monoclinic phase, $C2/m$) and VO_2 (A) (tetragonal phase, $P4_2/ncm$) [558-561], however the most stable is VO_2(R)

phase. Crystal structure of these four VO_2 polymorphs, is based on bcc oxygen lattice, with a somewhat regular oxygen octahedra, and vanadium in octahedral sites . In VO_2(R) and VO_2(M), the oxygen octahedra is aligned along two perpendicular directions, while for VO_2(B) and VO_2 (A) the oxygen octahedra is aligned along just one direction [559]. Despite having the same chemical formula, the crystalline and electronic structures are very distinct, exhibiting different electrical and optical properties [560, 562]. On table 1, the crystallographic parameters of the different vanadium oxide phases are shown.

Table 1. Space group and lattice parameter of the different vanadium oxide phases [563-568].

Crystallographic phase	**Space group**	**Lattice parameter (Å)**		
		A	*B*	*c*
VO_2 Monoclinic	$P2_1/c$	5.753	4.753	5.383
VO_2 Monoclinic	C2/*m*	12.03	3.693	6.42
VO_2 Tetragonal	$P4_2/ncm$	8.440	8.440	7.680
VO_2 Tetragonal/Rutile	$P4_2/mnm$	4.554	4.554	2.856
V_2O_3 Rhombohedral	D3*d*	4.9517	14.005	2.8283
V_2O_5 Orthorhombic	P*mmn*	11.510	3.563	4.369
V_3O_7 Monoclinic	C2/*c*	18.626	3.622	13.719
V_4O_9 Orthorhombic	C*mcm*	10.356	8.174	16.559
V_6O_{13} Monoclinic	C*m*	11.900	3.680	10.200

VO_2(A) and VO_2(B) are thermodynamically metastable phases that present a layered structure similar to V_2O_5 [569]. VO_2 (A) was reported as an intermediate phase in the transformation $VO_2(B) \rightarrow VO_2(R)$ [569]. Moreover, when heated to temperatures around 68 °C, the VO_2(M) phase presents a Mott metal-insulator transition that is characterized by a change in crystal structure from semiconductor phase ($P2_1/c$) to metallic phase VO_2(R) ($P4_2/mnm$) [558, 569]. Figure 23 shows a schematic representation of the unit cell of each oxidation phases of vanadium oxides.

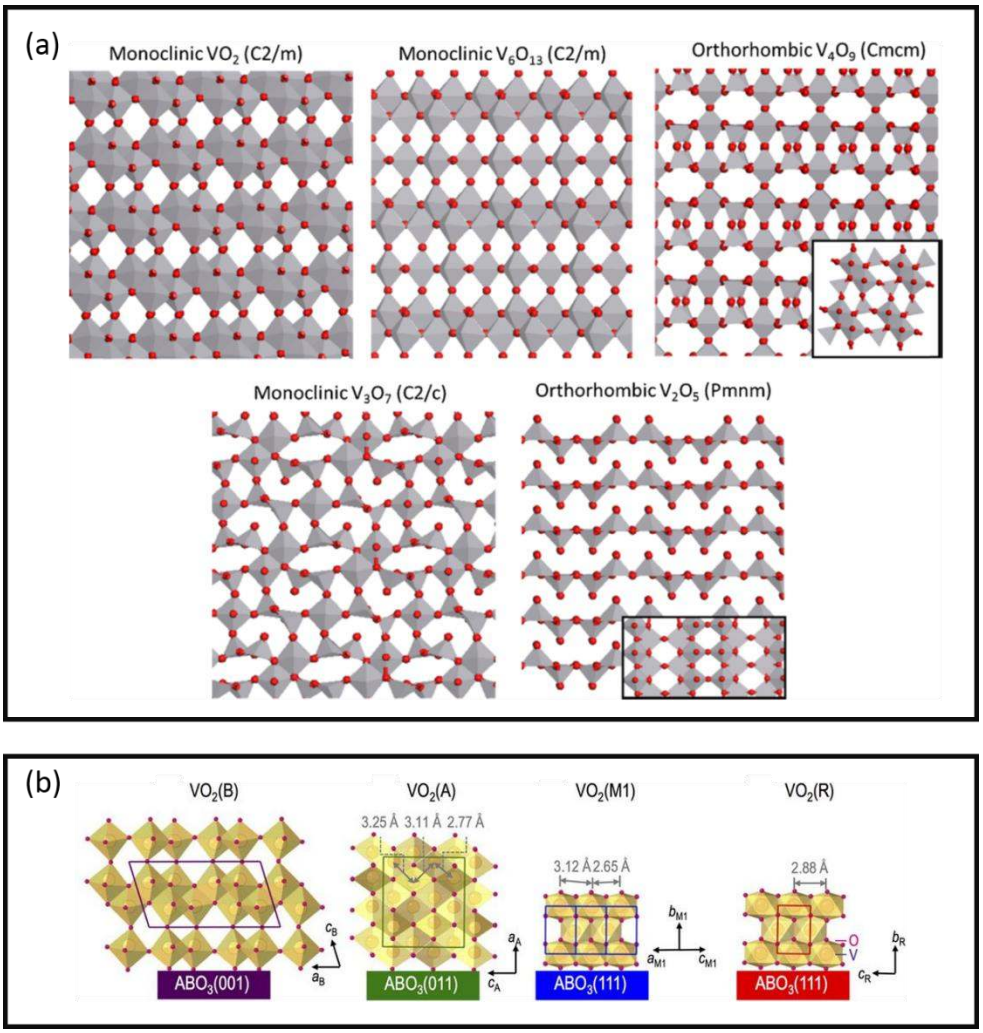

Figure 23. Schematic representation of (a) the *a*-axis of the lattice of V***n***O_{2n+1} for n = 2, 3, 4 and 6 [556] and (b) VO_2(B), VO_2(A), VO_2(M) and VO_2(R) phases [560]. Reproduced with permission of *John Wiley and Sons* [556] and *Springer Nature* (2018) [560].

Due to their electronic and structural properties this class of oxides can be used in a vast number of applications, from catalysis [570], environmental pollution control optoelectronics [571, 572], in smart thermochromic and electrochromic windows [556, 573, 574], optical switches [575, 576] and in energy storage [577, 578]. In terms of sensing applications, reports have shown that the most used phases are VO_2(R) and V_2O_5, due to their metal to insulator transition at relatively low temperature that may alter resistivity by three orders of magnitude [560].

Different nanostructures can be synthesized via hydrothermal/solvothermal method [571, 572, 579], chemical bath [555], chemical vapor deposition [580], thermal evaporation [570], electrodeposition [578, 581, 582] and electrospinning [583]. With these production methods, it is possible to obtain different vanadium oxide morphologies, such as spheres [572], nanotubes [584, 585], nanorods [571], nanobelts [579], nanowires [570]. On Figure 24, it is possible to observe some of the vanadium oxide nanostructures reported.

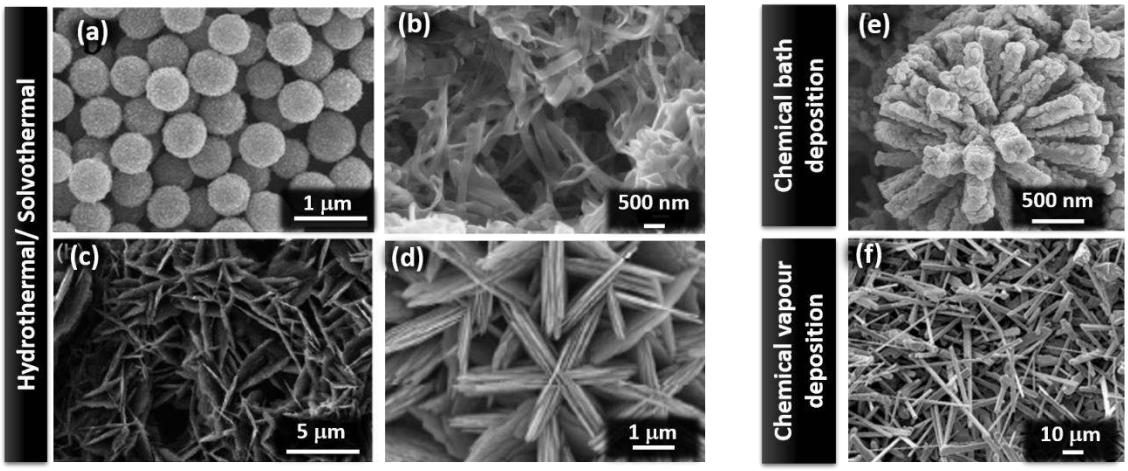

Figure 24. (a) V_2O_5 hollow spheres [572]; (b) V_2O_5 nanobelts [579]; (c) VO_2(M) nanoflowers [558]; (d) VO_2 carambola shaped nanostructure on graphene [586], reproduced with permission of Royal Society of Chemistry (2018); (e) V_2O_5 urchin-like structures [555], and (f) VO_2 nanorods [580]. Reproduced with permission of *Royal Society of Chemistry* [572] and [586], *Wiley and Sons* [579] and [558]; *Springer Nature* [555] and *Elsevier* (2018) [580].

Gas sensors based on nanostructured vanadium pentoxide, V_2O_5, are the most used for detection of combustible gases [572, 579]. Wu *et al.* [572] synthesized V_2O_5 hollow spheres and suggested that by using this type of nanostructures, gas sensing properties would by greatly improved due to their high ratio of volume to surface area. When V_2O_5 nanostructures are exposed to reducing gases, V^{5+} species are partially reduced to V^{4+}, originating formation of oxygen vacancies thus increasing conductivity of the sensor (this phenomena can be optically observed due to a material colour change

from yellow to dark blue) [572, 584]. Wu was able to detect trimethylamine (one of the toxic gases released by the decomposition of fish and other seafood) with detection limit of 10 ppb, response of 1.283 and maximum recovery time of 150 s at a working temperature of 370 °C [572]. Griogorieva *et al.* [571] produced V_2O_5 nanorods that showed stable response to trimethylamine (detecting 10 ppm with sensor response of 1 to 3 %), but weak response to carbon monoxide (only 0.3 % at 180 °C), with short response time of 32 s. For the detection of ethanol, Liu *et al.* [579] used V_2O_5 nanobelts synthesized via hydrothermal method. These sensors were tested in a temperature range between 150 and 400 °C, with an increasing concentration from 10 to 100 ppm of ethanol. The lowest detection limit was about 5 ppm, with response and recovery time of 30 to 50 s [579]. Also, Liu *et al.* [555] used V_2O_5 urchin-like structures and nanorods not only for detection of acetone, but also of isopropanol and ammonia, with detection range of 10 to 1000 ppm and recovery time of 200 to 500 s.

Another interesting approach was presented by Liang *et al.* [580] that investigated sensing properties of VO_2 decorated with gold nanoparticles to NO_2 gas. It was found that VO_2 nanowires decorated with the smallest Au nanoparticles exhibit sensitivity to NO_2 of 0.5 to 5 ppm. Liang attributed this response enhancement to a "spillover effect" and to changes in the depletion layer caused by the presence of Au nanoparticles [580]. The small particle size and high number of particles accelerate dissociation and adsorption of oxygen at VO_2 surface and thus improve the sensor response from 1.14 to 3.22. This report also showed that VO_2 decorated with Au was also sensitive to acetone, ethanol, isopropanol and NH_3, with response of 1.04, 1.08, 1.12 and 1.05, respectively [580].

Vanadium oxide nanostructures have been widely used in the detection of toxic and flammable gases, however the high working temperature necessary to achieve good sensitivity, still remains a major challenge. Schneider *et al.* [587] developed

nanostructured V_2O_5 films for detection of hydrogen, methane and propane, with a good response (0.2) in the presence of 5 to 300 ppm of gas at 200 ºC (Figure 25 (a)).

Some authors have reported the use of vanadium oxide as humidity sensor. Yin *et al.* [558] reported on the hydrothermal synthesis of VO_2(B) nanoflowers and their heat-transformation into VO_2(M), as well as their humidity sensing characteristics. Both sensors presented fast response and recovery time, with good stability and reproducibility. It was found that VO_2(M) nanostructures were more sensitive at high RH while VO_2(B) nanostructures presented higher sensitivity at low RH values [558].

In semiconductor nanomaterials, oxygen vacancies and oxygen ions adsorbed at the surface are active sites, thus water vapour is ionized to OH^- and H^+ [558, 588]. Subsequently, another H_2O molecule is adsorbed to the H^+ bond between two neighbouring OH^- groups. In the presence of high humidity levels, H_2O layers are formed at VO_2(M) surface that may be dissociated into H_3O^+. This will cause the depletion layer to decrease, promoting an increase in surface conductivity. In metallic VO_2(B) phase, with a lower resistance, the dominant charge carriers are electrons, e^-. For high humidity values and due to the polarity of H_2O molecules, some of these e^- are electrostatically attached to positively charged H^+ forming hydrogen bonds [26]. The density of free electrons at VO_2(B) surface decreases, increasing materials' resistance with humidity increase [558].

To improve the sensors' response to RH variation , some authors have reported on the use of some additive or the formation of hybrid composites, such as VO_2 – carbon nanotubes composites [589]. Doping with other semiconductor materials induces additional atomic defects modifying sensing properties [583]. Araújo *et al.* [583] doped TiO_2/WO_3 composites with different percentages of V_2O_5 that demonstrated a change in impedance of an order of magnitude when detecting RH ranging from 40 to 100 %.

Moreover, Evans *et al.* [589] produced humidity sensors based on VO_2 – carbon nanotubes composites. These nanocomposites presented high response to water vapour, with sensitivity between 2.7 and 3.6, when increasing the RH to 50 %. Devices resistance was reduced by incorporation of carbon nanotubes, CNTs, suggesting that these significantly contribute to the increased composites' conductivity [589] (Figure 25 (b)).

The use of vanadium oxides in UV sensing is not common, nevertheless some reports show that this semiconductor presents a good responsivity to UV radiation. Zhai *et. al.* [590] reported on the photoconductive of centimeter-long V_2O_5 nanowires produced by hydrothermal method. These nanowires presented responsivity of ~482 A W^{-1} and EQE ~132800% at 450 nm and 1.0 V. Wu *et al.* [591] demonstrated responsivity of a single microwire to UV radiation. Photoconductor made of a single nano/microwire can yield much higher sensitivity and responsivity than the bulk material. The VO_2 microwire photodetector presented responsivity of 7069 A W^{-1} and response time of ≈ 126 ms (Figure 25 (c)).

One interesting approach is using the V_2O_5 nanostructures as photochromic UV detectors. Miyazaki *et al.* [592] produced a V_2O_5 based composite that exhibit photochromic properties when irradiated with UV light. These showed multichromism, changing from yellow to green and to pale blue with good reversible photochromic properties when placed in the dark. Miyazaki assumed that UV irradiation is responsible for V_2O_5 reducing from +5 to +4 states and associated colour change. Optical band gap increased with UV irradiation due to increase in carrier concentration (Figure 25 (d)).

Other studies reported doping of vanadium oxides with other metal oxides to increase responsivity, response and recovery time of UV sensors. Vanadium oxide doping exhibited an enhancement in luminescence and in photo-sensing properties. These properties arise from formation of defect states within the bandgap, which traps and de-

traps electrons. Srivastava *et al.* [593] reported substitution of some vanadium atoms in ZnO, which lead to an increase in UV sensitivity and responsivity, which was attributed to trapping and de-trapping of electrons at V^{4+} and V^{5+}-related defect states. Whereas the V^{5+} state is empty, the V^{4+} state has an extra available electron that when illuminated by UV irradiation will move to the conduction band and increase photocurrent. This study also showed that sensor responsivity increased for 1.76 % of vanadium content to 120 μA W^{-1} when compared to undoped material (4 μA).

The use of vanadium oxide semiconductor in biosensing applications is rather rare. Nevertheless, being a biocompatibility material, V_2O_5 have attracted much attention for the fabrication of bio-electrodes, due to their high catalytic properties and also to their high electron transfer [594]. Suresh *et al.* [595] doped V_2O_5 with Ni for determination of dopamine (an electroactive neurotransmitter vital in the central nervous system) at nanomolar level. The doped nanoparticles showed a good response to dopamine in concentrations ranging from 6.6 to 96.4 μM, with sensitivity of 132 nA μM^{-1} and limit of detection of 28 nM. Suresh suggested that Ni-$V^{5+}{}_2O_5$ causes oxidation of dopamine and is then electrochemically reduced to Ni-$V^{4+}{}_2O_5$. and after donation of an electron to the carbon electrode is regenerated to Ni-$V^{5+}{}_2O_5$.

Most of existing reports are related with the use of V_2O_5 nanocomposites. Yang *et al.* [596] produced an electrochemiluminescence (ECL) aptasensor for the detection of mucin 1 (a biomarker associated to breast and pancreatic cancer) using V_2O_5 nanospheres as peroxidade mimics. V_2O_5 was synthesized and added to ABEI (*N*-(4-aminobuthyl)-*N*-(ethylisoluminol)), functionalized with silver nanoparticles, thus forming a nanocomposite that was applied to the sensor electrode. The produced sensors' signal increased by about 2.7 times. Yang suggested that V_2O_5 nanospheres are responsible for loading a large number of luminuphores with an enhanced ECL signal. This approach

displayed detection range of 10 fg mL^{-1} to 10 ng mL^{-1}, with a limit of detection down to 3.33 fg mL^{-1} [596].

Other composites using V_2O_5 nanostructures and carbon nanotubes were reported. These nanocomposites were used to improve sensing properties. Xiaobing *et al*. [597] reported the development of carbon nanotubes/V_2O_5/chitosan nanocomposite for detection of ciprofloxacin (an antibiotic widely used in health and agricultural industries, which the residues may cause skin infections and respiratory infections). This sensor combines the biocompatibility of V_2O_5, the efficient electron transfer of carbon nanotubes and the effective fil-forming strength presented by chitosan. Moreover, it presented good selectivity and low limit of ciprofloxacin detection (0.5 ng mL^{-1}) on milk, with a recovery rate of 94.5-97.87% (Figure 25 (e)) [597].

Sun *et al.* [598] also used this nanocomposite (nanotubes/V_2O_5/chitosan) for fabrication of electrodes for immobilization of single-stranded DNA. The experiments performed by Sun suggested that the synergistic effect of V_2O_5/Carbon nanotubes leads to increased amount of single-stranded DNA being adsorbed onto the electrode's surface, thus increasing the electrochemical response. The biosensor produced by Sun *et al.* was able to detect concentrations in the range of 1.0×10^{-11} to 1.0×10^{-6} mol L^{-1}, with detection limit of 1.76×10^{-12} mol L^{-1}.

Another biosensor based on these types of nanocomposites electrodes was reported by Alagappan *et al.* [594] for detection of methylglyoxal, which is responsible for complications in diabetic patients. This bioelectrode was able to measure concentrations of methyglyxal in par-boiled rice ranging from 0.1 to 100 µM, with sensitivity of 1130.86 µA cm^{-2}, limit of detection of 2 nM and response time <18 s. Vanadium oxide has an isoelectric point of 3 which allows electrostatic attraction of the glutathione cofactor, that has a high isoelectric point (5.93). In the absence of

methyglyxal, glutathione will oxidize to hemithioacetal at -2.74 mV, while in the presence of 0.1 µM of methyglyxal the the required potential is -32.29 mV [594].

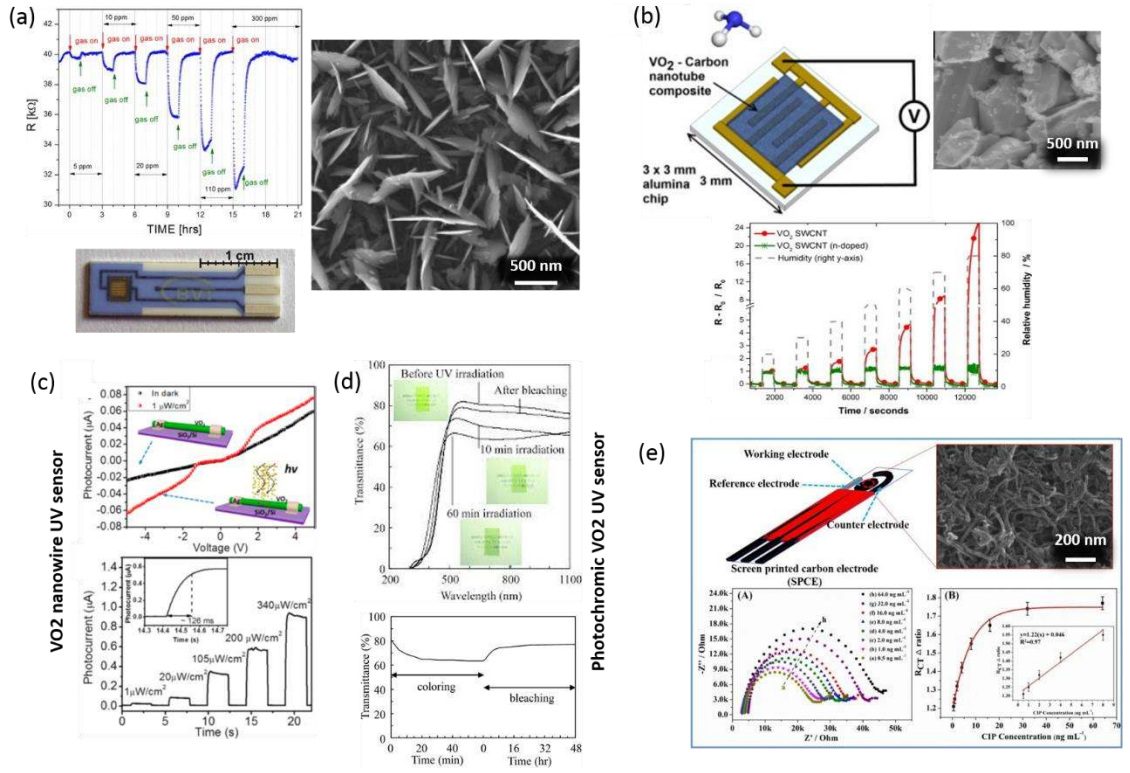

Figure 25. (a) V_2O_5 nanostructured film for hydrogen gas sensing application [587]; (b) VO_2-carbon nanotube composite for humidity sensor [589]; (c) VO_2 microwire UV photodetectors and the correspondent photocurrent at 4 V under different UV illumination intensities (the inset show the response time) [591]; (d) UV-VIS spectra of the V_2O_5 nanostructured photodetector when irradiated with UV light and their time dependence of the transmittance when coloring and bleaching [592]; (e) Schematic, SEM image and Nyquist plots of the carbon nanotube/V_2O_5 electrodes used in biosensing application [597]. Reproduced with permission of *Elsevier* (2018) [587], [589] and [597]; *ACS publishing "Copyright (2018) American Chemical Society"* [591]; and *Royal Society of Chemistry* (2018) [592].

3. Overview of the metal oxide sensors performance

This section describes the comparison between all the different metal oxides discussed above, organized by sensor device type. Table 2 summarizes different metal

oxide nanostructures employed as gas sensors. Metal oxides have been largely integrated in gas sensors over the years and several types of gases, including NO_2, H_2 to C_2H_5OH and NH_3, have been evaluated at different concentrations. The temperature at which sensing experiments are carried out, is also imperative. As can be seen from Table 2, the used temperatures are widely diverse and even if some sensors work at room temperature (RT), which enables low cost devices and improves long-term stability, most of the nanostructures investigated show working/operating temperatures from 200 to 500 ºC. This range of temperatures is too high from a practical use point-of-view and leads to energy waste and emissions increase, which enhances danger of explosion when dealing with flammable gases.

In terms of metal oxides used, ZnO and TiO_2 are largely employed as gas sensors due to their high chemical stability, simple and cost effective production, easy surface oxygen adsorption, amongst others factors [233, 599]. Nevertheless, operation temperatures of both sensors are still high which limits their integration in real-time gas monitoring devices. The response/recovery times, especially for ZnO nanostructures, need deeper investigation for reaching fast responses, which may include surface modification, additive doping or light activation. WO_3 is considered a promising material for gas sensors having extensive application for environment and safety monitoring. WO_3 is an abundant material and can be synthesized by low-cost wet-chemical routes. However, in terms of gas sensing, this material has a drawback of intersecting sensitivity, which limits distinction of two gases in a mixture [600]. Nevertheless, sensitivity of WO_3 to several gases has been tested and in some cases low detection limits (in the order of ppb) were achieved, especially for NO_2 (Table 2). The operation temperature is also lower (< 300 ºC for the presented nanostructured sensors) when compared to ZnO and TiO_2, presenting fast response/recovery times.

Copper oxide-based gas sensors have been reported over the years, especially to form *p-n-* heterojunctions. Copper oxides have *p*-type characters, besides being eco-friendly, non-toxic and compatible with wet-chemical synthesis routes. However, Cu_2O phase is unstable and easily converts to CuO. This thermal instability can influence the gas sensors behaviour, especially since Cu_2O demonstrates gas sensing activity at ~200 °C [400]. From Table 2, it is possible to observe that the operation temperature of copper oxide-based nanostructured devices is also lower than 300 ºC and that the response/recovery times are expressively different depending on the nanostructure or composite/mixture used. SnO is also thermally unstable and converts to SnO_2 when heated, which limits its utilization as gas sensors. On the other hand, SnO_2 is widely used in gas sensors [499] for detection of different gases, like ethanol, H_2, O_2, CO, NO, NO_2 and NH_3, due to its fast-response speed, high chemical stability, selectivity and low cost. Moreover, the presented nanostructured sensors work at temperatures < 300 ºC, with low detection limits (ppm) and fast response/recovery times. Vanadium oxides have recently been considered for gas sensing. V_2O_5 has been reported for combustible gases detection due to its good chemical and thermal stability. Nevertheless, the operation temperature, response/recovery times and detection limits of these sensors vary expressively depending on nanostructure used and vanadium oxide phase.

Table 2. Summary of overall performance of nanostructured metal oxides-based gas sensors.

Metal oxide nanostructure	Gas	Temperature (º C)	Detection limit	Response time (s)	Recovery time (s)	RH %	Ref.
ZnO nanowires, nanobelts and tetrapodes	H_2S and NO	RT	200 ppb H_2S 1 ppm NO	-	-	-	[146]
ZnO cloudy-like nanoparticles, isotropic nanoparticles	CO, C_3H_8, and NH_3	340, 400, and 500	100 ppm CO 100 ppm C_3H_8 19 ppm NH_3	-	-	50	[150]
ZnO nanobelts	NO_2	300 – 350	0.51 ppm	-	-	-	[151]
ZnO nanorods	NO_2	300 – 450	1 ppm	180	-	-	[152]
Au-doped ZnO nanostructures	NO_2	300 and 550	0.5 ppm	450	587_300 ºC 1020_550 ºC	-	[154]
ZnO nanorod arrays with NiO nanosheets Nanoheterojunctions	C_2H_5OH	200	100 ppm	55	70	-	[155]
TiO_2 nanowires	NO_2	RT	100 ppm	10	19	-	[233]
TiO_2 spongy layers	C_2H_5OH	350	44 ppm	10	-	40	[235]
Cr-doped TiO_2 films	CO NO_2	500	1000 ppm CO, 2 ppm NO_2	-	-	30 and 50 for NO_2	[236]
Au-doped TiO_2 films	CO H_2	300	5 ppm CO 8.5 ppm H_2	15 CO 480 H_2	10 CO 9.6 H_2	dry	[237]
TiO_2-SnO_2 nanostructures	H_2	400	-	60-120	300-420	-	[238]
Lamellar-nanostructured WO_3 particles	NO_2	200	50-1000 ppb	-	-	-	[303]
Porous WO_3 nanocrystalline	NO_2	300	50- 550 ppb	180	60	-	[304]
Three-dimensional hierarchical WO_3 nanostructures	NO_2	120_800 ppm	40-800 ppb	120_800 ppm	41_800 ppm	-	[305]
WO_3 nanotubes	NO_2	300	1-5 ppm	15-40	70-100	-	[306]
WO_3 nanowire-like structures	NH_3	250	9.7-1500 ppm	7	8	-	[307]
Pt-WO_3 hybrid nanorods	C_2H_5OH and CH_3OH	220	1, 5, 20, 100 and 200 ppm	9	-	-	[312]
Pd-WO_3/reduced graphene oxide Hierarchical nanostructures	H_2	100	20 ppm	60	-	-	[321]
Cu_2O nanowires	H_2	200	1000 ppm	-	600	dry	[411]
CuO 3D flower-nanostructures	C_2H_5OH	260	10-1000 ppm	5	15	-	[415]
CuO flower-like nanostructures	H_2S	RT	100 ppb - 20 ppm	240-480	900-3300	dry	[417]
CuO/ZnO nanorod heterojunction	C_2H_5OH	300	1 ppm	7	9	-	[422]
CuO-MnO_2 nanocomposite	NH_3	-	100 ppm	120	600	-	[424]
Cu_2O/CuO sub-microspheres	H_2S	95	50 ppb	-	76	-	[425]
Porous Cu_2O/CuO cubes	C_3H_6O	150	500 ppm	1	25	-	[426]

Nanosheets-assembled SnO_2 hollow spheres	C_2H_5OH	350	500 ppb	-	5	-	[503]
Porous SnO_2 nanoflowers	C_2H_5OH	240	100 ppm	2	15	dry	[504]
Hierarchical SnO_2 based ultrathin nanosheets	C_2H_5OH	-	100 ppm	1	2	-	[497]
Square-shaped SnO_2 nanowires	C_3H_6O	290	20 ppm	7	10	-	[505]
SnO disk-like structures	NO_2	200	100 ppb	-	-	-	[510]
Sb-doped SnO_2 nanowires	C_2H_5OH	300	10 ppm	1	5	-	[512]
Hierarchical SnO_2/rGO nanostructure	H_2S	100	10 ppm	7	-	-	[514]
WO_3-SnO_2 nanofibers	C_2H_5OH	-	10 ppm	18.5	282	-	[516]
SnO_2-decorated NiO nanostructures	C_7H_8	250	1.2-10 ppb	-	-	15-90//10 ppm	[521]
V_2O_5 hollow spheres	Trimethylamine	370	10 ppb	-	150	-	[572]
V_2O_5 nanorods	Trimethylamine	175	10 ppm	32	330	-	[571]
V_2O_5 nanobelts	C_2H_5OH	200	5 ppm	30	50	-	[579]
V_2O_5 urchin-like and rod structures	C_3H_6O	150	10 - 1000 ppm	-	200 and 500	30	[555]
VO_2 decorated with gold nanoparticles	NO_2	25-100	0.5 - 5 ppm	-	-	-	[580]
Nanostructured V_2O_5 film	H_2, CH_4, and C_3H_8	200	5 - 300 ppm	-	-	-	[587]

Nanostructured metal oxides-based humidity sensors that can detect humidity changes in a vast range of values, between 0 and 100% RH, have been reported for all the discussed metal oxide materials (see Table 3). ZnO presents a good detection range, however it has the disadvantage of being hydrophobic, which limits sensitivity improvement. On the other hand, TiO_2 often presents superior humidity sensitivity due to its hydrophilic properties, which arise from surface defects. This material presents fast response times but longer recovery times. Moreover, the use of TiO_2 may lead to low long-term stability. WO_3 is also an interesting alternative for humidity sensors due to its high sensitivity, which is generally attributed to structural defects. The use of copper, tin and vanadium oxides as a humidity sensor is not so common, nevertheless they all present fast response and recovery time and good long-term stability.

Table 3. Summary of overall performance of nanostructured metal oxides-based humidity sensors.

Metal oxide nanostructure	Detection range (%RH)	Response time (s)	Recovery time (s)	Hysteresis (%)	Ref.
ZnO	15 - 95	7	14	1.8	[157]
ZnO nanoparticles	0 - 80	5	-	8.6	[158]
ZnO/SnO_2	11 - 95	50	100	2	[160]
ZnO/TiO_2	11 - 95	774.9	19.7	-	[161]
TiO_2 nanosheets	11 - 95	3	50	4.6	[239]
TiO_2/graphene	12 - 90	121	68 – 128	<0.39	[240]
TiO_2/conducting polymer	30 - 90	30	45	2	[241]
TiO_2:LiCl	5 - 95	0.75	1	-	[243]
WO_3:Li:K	1 - 95	15	10	3	[324]
WO_3 on nanoporous silicon	11 - 95	104	94	5.3	[327]
WO_3/Poly(2,5-dimethoxyaniline)	23 - 84	27	136	5	[328]
WO_3: ZnO	15 - 95	65	360	1.09	[329]
CuO nanowires	52 - 90	-	-	-	[430]
Cu_2O porous film	Up to 58	151	145	4.38	[431]
CuO:ZnO	10 - 90	76	296	2.30	[437]
SnO_2 nanoparticles	5 - 95	32	25	-	[522]
SnO_2 ordered nanostructures	5 - 96	32	42	< 5	[523]
SnO_2 nanofiber	Up to 85	1	1	-	[524]
Ion doped SnO_2 nanofiber	11 - 95	5	6	-	[525]
VO_2	Up to 92 %	5 – 8	2 – 3	7	[558]
$TiO_2/WO_3/V_2O_5$	40 - 100	-	-	-	[583]

Table 4 shows that ZnO, WO_3 and SnO_2 are largely employed as UV sensors/photodetectors, while other metal oxides, such as CuO/Cu_2O, are used to produce *p*- *n*- heterojunctions. On the other hand, the use of TiO_2 and vanadium oxides in such devices is not widespread, nevertheless some studies have reported their behaviour as photoactive layers for UV sensors. The photocurrents, I_{on}/I_{off}, responsivity and response/recovery times vary expressively for each sensor, largely depending on the metal oxide and even nanostructure used. Moreover, sensor behaviour is widely influenced by substrate, UV lamp and the environment where the measurements are carried out. Nevertheless, comparing metal oxides, it can be seen that ZnO shows the highest values of photocurrent and I_{on}/I_{off}, and for that reason it is largely investigated for UV sensor applications. ZnO 1D nanostructures are especially interesting due to large

surface to volume ratio, which increases the photoresponse. WO_3 and SnO_2 also display acceptable I_{on}/I_{off} values, which make them interesting to be integrated in UV sensors. Moreover, the presented WO_3 nanostructures revealed fast response/recovery times. Vanadium oxides and TiO_2, on the other hand, show lower photocurrent and I_{on}/I_{off}.

Table 4. Summary of overall performance of nanostructured metal oxides-based UV photodetectors.

Metal oxide nanostructure	Photocurrent	Dark current	On/off ratio (I_{on}/I_{off})	R (A W^{-1})	Response time (s)	Recovery time (s)	Ref.
ZnO nanowire	12.22 mA (rigid substrate) 14.1 mA (flexible substrate) (3 V)	-	8.2×10^3 1.2×10^4	-	-	-	[171]
ZnO nanorod arrays (glass substrate)	5 mA (5 V)	90 µA	55	4×10^{-4}	60	-	[71]
ZnO nanorod arrays (cellulose substrate)	10.36 µA (10 V)	0.76 µA	13.63	1.19×10^{-6}			[13]
ZnO ultraporous nanoparticle networks	1.2 mA (5 V)	3.61 nA	3.4×10^5	-	~250	~150	[172]
ZnO nanorods	-	-	1.09×10^4	55.5	3.1	1.25	[164]
TiO_2 nanorod arrays	249.68 µA (2.5 V)	-	-	13	-	-	[247]
TiO_2 nanorod flower-like structure (cellulose substrate)	3.78 µA (10 V)	0.15 µA	25.2	$3.3\ 10^{-7}$	-	-	[246]
WO_3 nanosheets	2.5×10^{-5} A	-	2×10^3	293	0.04	~0.08	[331]
WO_3 nanowires	0.1 nA (1 V)	17.2 nA	172	-	~70	~140	[333]
WO_3 nanobelts	12 nA (5 V)	12 Pa	1×10^3	2.6×10^5	-	-	[334]
3D WO_3 nanoshale	4.5 µA (20 V)	-	-	5.1	6.3	0.5	[335]
WO_3 nanodiscs/rGO	~1.1 µA (20 V)	-	-	6.4	0.013	0.016	[330]
CuO/Si nanowire array heterojunction	0.96 µA (0 V)	-	-	3.89×10^{-4}	6×10^{-5}	8×10^{-5}	[439]
CuO nanowire/ZnO branched nanowires heterojuntion	~1.7 mA (1 V)	~0.7 mA	2.43	0.123	-	-	[440]
Cu_2O film/ZnO nanowire	~0.5 µA (2 V)	-	-	~50	-	-	[441]
SnO_2 nanowire	2.1 µA (1 V)	19.4 nA	108	-	-	-	[533]

SnO_2 nanowire arrays	130 μA (12 V)	77 ∟A	1.69	-	-	-	[532]
SnO_2 hollow nanospheres	0.01 A	-	-	2680	38	137	[534]
SnO_2 nanobelts-Sn nanodots	1.1 nA (10 V)	4×10^{-4} nA	2.75×10^3	56	<0.3	<0.3	[72]
CuO/SnO_2 *p-n* nanoscale heterojunctions	-	-	-	10.3	-	-	[536]
TiO_2 branches on electrospun SnO_2 nanofibers	-	-	4550	0.6	0.03	0.01	[539]
V_2O_5 centimeter-long nanowires	25.8 nA (1 V)	12.5 nA	2.06	~482	-	-	[590]
VO_2 microwire	-	-	-	7069	0.126	-	[591]

By analysing Table 5, it is possible to observe that ZnO and WO_3 nanostructures are largely employed in biosensing applications. On the other hand, vanadium oxides are mostly combined with other nanostructures, such as graphene or carbon nanotubes, to form composites, and thus enhance their sensitivity. Zinc oxide is mostly used for detection of glucose, as its high IEP promotes glucose oxidase adhesion. Copper oxides are also highly investigated for glucose detection, presenting high sensitivities and low detection limits. WO_3 nanostructured biosensors can detect very low concentrations of analyte and presents high sensitivity to different analytes. Also, WO_3 presents chromogenic properties, which enable its use in colorimetric sensors thus allowing production of low-cost disposable biosensors, using cellulose as substrate. Although TiO_2 can be used in biosensing applications, the sensitivity presented by this type of nanostructures is very low, showing a very low detection limit. SnO_2 nanostructures are used in biosensing when doped or combined with other elements, presenting high sensitivity and low detection limit.

Table 5. Summary of overall performance of nanostructured metal oxides-based biosensors.

Metal oxide nanostructures	Analyte	Analyte concentration	Detection limit	Sensitivity	Ref.
ZnO nanowires	Glucose	0.03 to 1.52 mM	9 µM	17 µA/ cm^2mM	[176]
ZnO nanocombs	Glucose	0.02 to 4.5 mM	0,02 mM	15.33 µA/cm^2mM	[177]
ZnO nanorods	SSEA-4 antibodies	2 mM	Optical detection	-	[178]
ZnO nanosheetes	Cytochrome *c*	1 to 1000 µM	0.1 µM	-	[185]
ZnO	cTnT	1 to 100 ng/mL	0.1 ng/L	-	[182]
ZnO nanoparticles	cTnI	1 ng/mL – 10 µg/mL	2.191 ng/mL	15.8 nA(g/mL)$^{-1}$	[183]
TiO_2 nanotubes arrays	immunoglobulin	115 mg/mL	14 ng/mL		[223]
TiO_2 nanotubes	Glucose oxidase	0.1 – 6 mM	-	0.954 µA/cm^2mM	[251]
Carbon-doped TiO_2 nanotubes arrays	5-hydroxytryptamine and ascorbic acid	5 to 150 µM	4.1×10^{-8} M	-	[255]
graphene/TiO_2 nano rods/chitosan	Transgenic soybean sequence of MON89788	1.0×10^{-12} to 1.0×10^{-6} mol L^{-1}	7.21×10^{-13} mol/L	-	[256]
Graphene nanosheets/TiO_2	Glucose oxidase	0 to 8 mM	-	6.2 µA/cm^2 mM	[257]
TiO_2 nanoparticles	Laccase	0.075 to 150 µM	0.75 µM	2.6 µA/cm^2µM	[258]
WO_3 nanoparticles	c*c*NiR	5 to 50 µM	5 µM	2143 mA/cm^2mM	[338]
WO_3 nanoparticles	cytochrome	3×10^{-7} to 3×10^{-4} M	2.4×10^{-7} M	63.51 mA/cm^2M	[339]
WO_3 nanowires	hemoglobin	1 to 4200 µM	0.28 µM	-	[340]
WO_3 nanoparticles	dopamine	0.1 to 600 µM	24 nM	-	[341]
WO_3 nanoparticles	L-dopa	0.1 to 1 µM	120 nM	-	[342]
WO_3 nanoparticles/carbon nanotubes	hemoglobin	60 to 1280 µM	0.07 µM	-	[343]
WO_3 nanoparticles	Geobacter Sulfurreducens cells	15 g/L	Optical detection		[262]
Graphene/WO_3	peroxidase	150 µM	238 nM	1.306 mA/cm^2mM	[345]
WO_3-reduced graphene	cysteine	0.1 to 100 µM	25 nM	-	[347]
Cu_2O nanocubes/graphene nanosheets	glucose	0.3 to 3.3 mM	3.3 µM	-	[442]
Cu_2O shuriken-like nanostructures	glucose	0.01 µM to 11.0 mM	0.035 µM	0.933 mA/cm^2mM	[444]
Cu_2O/carbon quantum dots	glucose	0.02 to 4.3 mM	8.4 µM	-	[447]
CuO	glucose	1.0 to 170 mM	0.91 mM	246 mA/cm^2mM	[446]
CuO nanotubes	glucose	5 µM to 3.0 mM	0.1 µM	1.89 mA/cm^2mM	[448]
CuO nanoparticles	glucose	0.05−18.45 mM	~0.5 µM	2762.5 µA/cm^2mM	[449]
CuO nanoparticles	glucose	0.1 to 6.5 mM	0.5 µM	2419.8 µA/cm^2mM	[450]

CuO nanoparticles	Uric acid	0.05 mM to 1.0 mM	0.14 mM	2.7 mA/cm^2 mM	[445]
ZnO – CuO	cholosterol	0.12 to 12.93 mM	-	680 µA/cm^2 mM	[451]
ZnO – CuO	glucose	up to 8.45 mM	0.40 µM	2961.7 µA/cm^{2}mM	[443]
SnO_2 nanorods	H_2O_2	50 to 200 mg/L	0.2 µM	379 µA/cm^{2}mM	[542]
SnO_2:Sb nanowires	H_2O_2	-	0.8 µM	100 mA/cm^{2}M	[544]
ZnO/SnO_2 heterostructured	H_2O_2	2.0×10^{-6} to 3.7×10^{-4} M	0.46 µM	52.8 mA/cm^{2}M	[548]
Graphene/SnO2 nanosheets	Glucose	2 to 20 mM	-	20.3 µA/cm^{2}mM	[549]
Carbon nanotubes/SnO_2/graphene/chitosan	Lysine oxidase enzyme	0.99 to 160 µM	0.15 µM	55.20 µA/cm^{2}mM	[553]
V_2O_5:Ni	dopamine	6.6 to 96.4 µM	28 nM	132 nA/cm^{2}µM	[595]
V_2O_5 fuctionalized with Ag	Mucin1	10 fg/mL to 10 ng/mL	3.33 fg/mL	-	[596]
Chitosan/V_2O_5/carbon nanotubes	DNA	1.0×10^{-11} to 1.0×10^{-6} M	1.76×10^{-12} M	-	[598]
Chitosan/V_2O_5/carbon nanotubes	methyglyxal	0.1 to 100 µM	2 nM	1130.86 µA/cm^{2}M	[594]

4. Field-effect transistor structures for sensing applications

4.1. Advantages and challenges of sensing with (oxide nanostructure) field-effect transistors

While the oxide nanostructures exposed in the previous sections enable by themselves remarkable sensing performance, potential for miniaturization, parallel sensing, faster response time, improved selectivity and sensitivity and seamless integration with electronic manufacturing processes can be greatly enhanced when sensing is based on field-effect transistors (FETs) [601, 602]. In fact, and considering that oxide nanostructures can be grown on or transferred to FETs at low temperatures, the FET sensing approach seems to be perfectly tailored for the so-called system-on-foil concepts, combining the advantages of both “More Moore” (small size, high speed) and “More than Moore” (multifunctional) paths [603].

The great advantage of nanostructures compared to thin films of bulk materials for sensing was already extensively demonstrated throughout this review paper and naturally

these advantages are also extended to FET structures. Nanowires have been the selected nanostructure for most of the FET sensors reported so far. From a device point of view, two main reasons can be pointed out for this: first, they enable the confinement of charge transport essentially along one direction of the nanostructure, assuring improved electrical properties [604]; second, due to their 1D shape nanowires are easier to integrate between two electrodes (source and drain) [603].

Fabrication of FET sensors involves more processing steps than conventional conductometric sensors, requiring integration of an extra terminal (gate), electrically insulated from the oxide semiconductor nanostructure by a gate dielectric. As in conventional nanowire FETs, different device structures can be conceived for FET sensors, such as back-gate, top-gate, horizontal or vertical surrounding-gate [605]. The back-gate nanowire FET, depicted in Figure 26, is the most widely explored FET structure for sensing. While it potentiates an inefficient gate control of the drain-to-source current (I_{DS}) across the nanowire due to non-uniform electrostatic contact of a nanowire with a planar dielectric, this structure has at least two great advantages for sensing applications: first, its straightforward fabrication. In fact, considering the simpler approach, the FET sensors can be fabricated by drop-casting a solution containing dispersed nanostructures in a solvent on a highly-doped Si substrate (gate) having a thermally grown SiO_2 layer. Then, source-drain electrodes can be defined on the edges of a single nanowire following a pick-and-place approach, *e.g.,* using photolithography and e-beam evaporation; second, a back-gate configuration enables the nanowire surface to be readily exposed to the surrounding ambient, which is crucial to explore most of the sensing mechanisms.

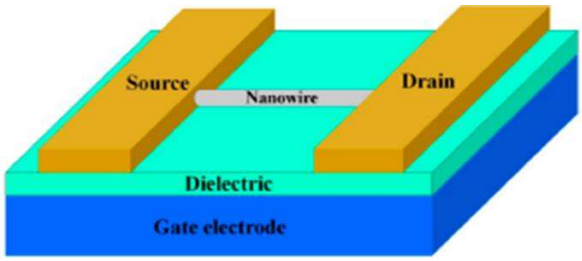

Figure 26. Schematic cross section of a back-gate nanowire FET. Reproduced with permission of *MDPI* (2018) [602].

This last argument brings a very interesting comparison to nanowire FETs used for electronic applications, which is particularly relevant when considering oxide nanostructures as the heart of these sensors: while on "electronic FETs" intense research has been carried out to block the interaction between oxide nanostructure surface and the surrounding environment, as it is well known that this can greatly affect device performance [606], in sensing FETs the nanowire's surface is intentionally left to interact with the ambient. Nevertheless, one should naturally understand that for both types of nanowire FETs the control of existing surface defect states by routes as doping, annealing or ozone treatments is a crucial requirement to establish stable and reliable platforms to work with [607, 608].

Many successful attempts to use FETs sensors based on oxide nanostructures have been reported during the last decades. While a detailed review on this topic would constitute an extensive document on its own and is thus out of the scope of the present review article, oxide nanostructure-based FETs are too relevant to be left out of any comprehensive review on oxide sensors. As such the next subsection presents major considerations on what has been perhaps the most active research area regarding sensing with oxide nanowire FETs: gas sensors. The reason for narrowing the discussion to a single type of sensors is that most of the concepts exposed can be the eadily applied to other types, where sensing also relies on interactions at the oxide nanostructure surface, given that those interactions will eventually affect carrier concentration which is one key

aspect governing the properties measured on a FET. Based on this concept, significantly improved sensing performance when FET structures are used have been shown for humidity, UV and biosensors [92, 609, 610].

4.2. Gas sensing with oxide nanowire field-effect transistors

FETs for gas sensing have been studied for more than four decades. Back in 1975, Lundstrom *et al.* demonstrated hydrogen sensing on a Si-based metal oxide semiconductor FET (MOSFET), demonstrating that the threshold voltage (V_T) of the device was a function of hydrogen partial pressure [611]. At this point it is worth noticing that MOSFET gas sensors reported by many other researchers since this initial report work under a different principle compared to the oxide nanowire-based FET sensors under discussion in this section. While MOSFET gas sensors rely on catalytic interaction between a metal gate and gas molecules, which results in a measurable change of I_{DS} within the Si channel of a conventional MOSFET, oxide nanowire-based FET sensors rely on the direct interaction between the oxide semiconductor and the gas. This interaction (adsorption or desorption of gas molecules) leads to multiple measurable changes on device characteristics, such as I_{DS}, V_T, mobility (μ) and subthreshold swing (S) [602, 612, 613]. These effects are a consequence of variation of the carrier concentration within the nanowire as the gas-nanowire interactions occur. Considering an *n*-type oxide nanowire (*e.g.*, SnO_2, ZnO, In_2O_3), oxidizing and reducing gas environments will result in decreased and increased carrier concentration, respectively. While this is also seen on two-terminal oxide nanowire-based conductometric gas sensors, the gate-to-source voltage (V_{GS}) in FET gas sensors can significantly enhance these effects, *i.e.*, taking the device to operate with a specific V_{GS} can result in very large sensor sensitivity. This arises as a consequence of the free carrier concentration modulation by V_{GS}, which in turn affects the rate and extent of oxidation/reduction reactions taking place at the oxide

nanowire surface [614, 615]. By operating the FET sensor at its subthreshold regime these effects are maximized, given that channel carriers are substantially depleted and thus, conductance changes caused by gas adsorption become much more significant [612].

The effect of V_{GS} on the carrier concentration also brings another advantage to FET-based gas sensors, which is the ability to operate at considerably lower temperatures than conductometric gas sensors: the latter are typically operated at 200-500 °C to decrease response and recovery times, given that gas adsorption/desorption are thermally-activated processes. As these response/recovery times are carrier concentration dependent, FET-based gas sensors can even operate at room temperature, as demonstrated with several *n*-type oxide semiconductor nanowires [612]. For instance, while the reported limits of NO_2 detection for individual In_2O_3 nanowire resistor sensors are ≈ 500 ppb at an operating temperature of 400 °C, In_2O_3 nanowire FET sensors exhibit limits of detection of 20 ppb at room temperature [615, 616], which is even lower than the 53 ppb required for monitoring of air quality standards [613, 615]. This brings significant advantages, such as low power consumption, longer device lifetime and reduced explosion hazards [612, 614].

Despite the proven advantage of V_{GS} control for sensing performance, other methods have also been used to enhance nanowire FET gas sensors. The most striking examples are nanoparticle decoration of the nanowire, local heating and light irradiation.

Pd, Pt, Ag, Au, ZnO and NiO nanoparticles have been used to modify the surface of oxide nanowires, resulting in improved sensitivity of FET sensors [617]. Two examples are shown in the figure below, one for NiO-functionalized SnO_2 nanowires used for CO detection [618] and another for Pd-coated SnO_2 nanowires used for H_2 detection [619]. The proposed mechanisms for these significant improvements are based on the created heterojunctions or Schottky barrier-type junctions (nanowire-nanoparticle), resulting in

the formation of depletion regions or even purely chemical catalytic effect when considering nanoparticles of noble metals [612].

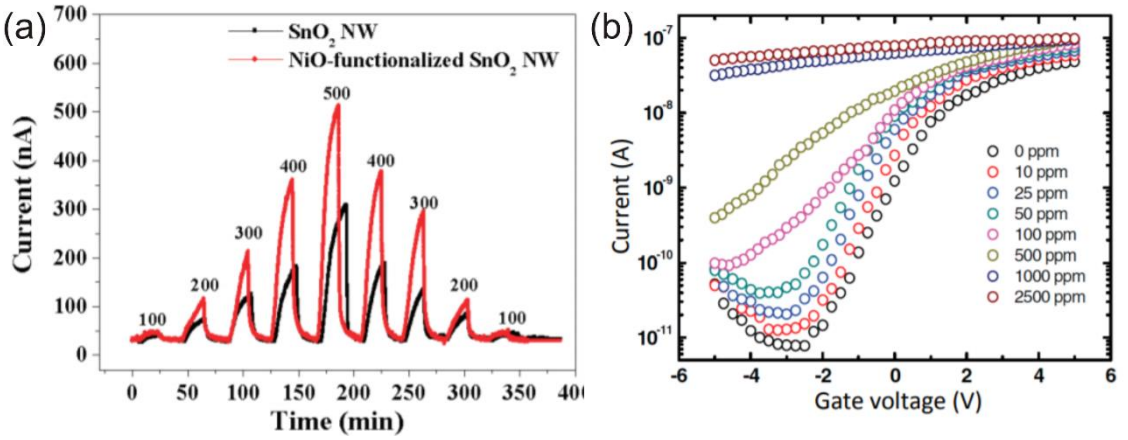

Figure 27. Enhancements on FET gas sensor sensitivity by functionalization of SnO_2 nanowires: (a) response curve for pure and NiO-functionalized SnO_2 nanowire-based sensor to CO, for a concentration of detected gas between 100 and 500 ppm, and operation temperature of 250 °C; (b) transfer characteristics of Pd-functionalized SnO_2 nanowire channel under different H_2 partial pressures, for operation temperature of 100 °C. Reproduced with permission of *ACS publishing* "Copyright (2018) American Chemical Society" [618] and *Wiley* [619].

A good example on how gas selectivity can be enhanced using the combined effect of V_{GS} and local heating was given by Dattoli *et al.* [620] with SnO_2 nanowire FET sensors and volatile organic compound analytes. By treating temperature- and gate-dependent analyte response variations as an identifying "fingerprint", an average recognition rate of 98 % was achieved using a statistical pattern recognition procedure. This value dropped to 76.7 % for measurements with gate in the grounded state.

The effect of light irradiation can also be quite relevant to achieve faster FET gas sensors. For instance, this was demonstrated already in 2002 for SnO_2 nanobelt FETs, by illumination with UV light with energy near the SnO_2 bandgap. Law *et al.* [621] concluded that the UV-generated carriers accelerated desorption velocity of NO_2 on the device . Similar effects were reported when using In_2O_3 nanowires [615].

An extensive list of oxide nanowire FET sensors based on SnO_2, ZnO, In_2O_3, Ga_2O_3 or Fe_2O_3 using the advantages of FET structures for sensing mentioned above have been demonstrated for detection of several gas molecules, such as NO_2, NH_3, CO, H_2, H_2S, CH_4 and O_2. In some cases, limits of detection in ppb range and response/recovery times of few seconds, were possible to achieve thus enabling real-time monitoring,. Detailed reviews on this can be found for instance in [612, 614, 622].

A last note should be considered regarding the feasibility of bringing these oxide nanowire FET sensors to large-scale manufacturing. The pick-and-place methodology used to prepare most of the nano-FET structures reported in literature is indeed a serious limitation, requiring selection of a single wire for deposition/patterning of source-drain electrodes. A process enabling direct growth of oxide semiconductor nanowires with controlled density on a receiver substrate, without requiring any transfer methods, would surely be desirable to overcome this limitation. A good example on how to achieve this was reported by Zhang *et al.* [615]. The authors used Si/SiO_2 substrates with tuned catalytic particle density to grow In_2O_3 nanowires by laser ablation. With this a network with multiple wires was obtained, which could then be contacted using standard photolithography and metal deposition, as shown in the figure below. Besides the simplified fabrication process and compatibility with large-scale manufacturing, these multiwire gas sensors also offer improved sensitivity to NO_2 and selectivity between NO_2 and NH_3 than single wire devices (Figures 28c and d). Selectivity reached 5 ppb, as compared to 20 ppb of single wire FETs, which was tentatively attributed to the formation of nanowire/nanowire junctions within the network, with associated depletion layers. Regarding selectively, it was associated with the possibility of having conductance changes in opposite directions upon exposure to NH_3 owing to a specific doping level distribution within the network.

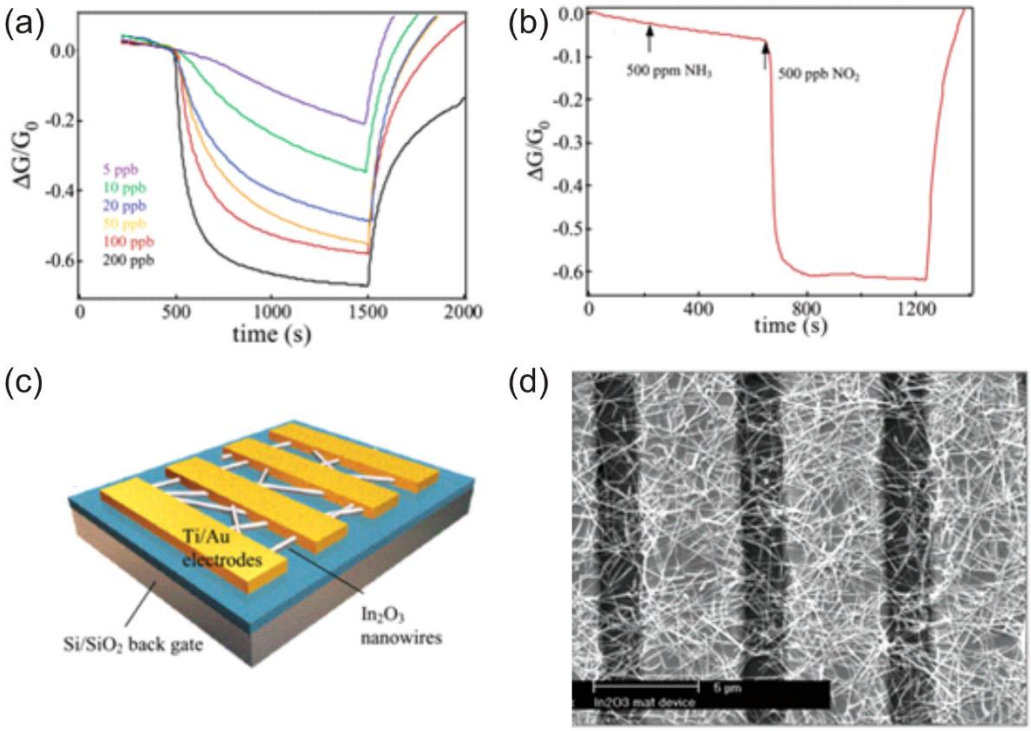

Figure 28. Multiwire In_2O_3 FET gas sensor: (a) schematic of device structure; (b) top-view scanning electron microscope image of the device; (c) sensing cycles corresponding to NO_2 concentrations between 5 and 200 ppb; (d) selective sensing to NH_3 and NO_2. Reproduced with permission of *ACS publishing "Copyright (2018) American Chemical Society"* [615].

Nonetheless, for integration in low-temperature and even flexible substrates, reliable transfer or direct growth methods of oxide nanowires that are compatible with the low thermal budgets need to be implemented. This is still one of the major bottlenecks inhibiting advances of flexible oxide nanoelectronics [603].

5. Conclusions and future perspectives

This review presented and summarized the latest advances in sensing technologies, focusing in four types of sensors, *i.e.* gas, humidity, UV and biosensors. This work was centered in semiconductor metal oxides at the nanoscale, which potentiates sensors performance due to nanomaterials intrinsic properties such as, high surface-to-volume ratios and high surface reaction activity. The selected metal oxides have in common the fact that these are earth abundant, low-cost, nontoxic and compatible with wet-chemical

synthesis routes. The sensing mechanisms of the presented sensors and the general properties of the selected metal oxides have been discussed in detail. It has been demonstrated that distinct nanostructures, such as nanowires, nanotubes, core-shell nanostructures, nanosheets, nanofibers, nanocubes, nanospheres, amongst others, are the path for novel and enhanced sensor materials. The main limitations of the current sensors have been addressed, and several approaches to increase materials' sensitivity and general sensor behaviour have been discussed, which included the effect of doping and combination with other metal oxides to produce nanocomposites or carbon-based materials. A last section on FET-based sensing showed that the extra gate electrode of these structures compared to two-terminal sensors enables significant improvements on sensor performance, namely on sensitivity, selectivity and response/recovery time. However, large scale manufacturing of oxide nanostructure FET sensors on flexible substrates still requires major advances on reliable routes to obtain controlled density of high-quality networks of nanostructures on those substrates.

In terms of future perspectives, the scientific community has been focused on the development of innovative synthesis strategies capable of specifically tuning the metal oxide structures at the nanoscale, as well as their intrinsic properties. For example, this could be observed in the evolution of UV sensors with single 1D nanostructures that originated high performance devices. These nanostructures are expected to diminish defect density and thus facilitate transport of carriers in the nanostructures, which enables high external quantum efficiency and fast response time.

Miniaturization of sensors maintaining or increasing sensor sensitivity and selectivity is also one of the major concerns of researchers nowadays, as well the production of flexible and low-priced systems. The use of inexpensive, lightweight, abundant, recyclable, and environmentally friendly substrates, such as polymer and paper-based

materials, is a reliable way to produce the next generation sensing devices expected to be highly adaptable, disposable, eco-friendly, sustainable and recyclable smart products. Moreover, these substrates allow large-scale production of devices and can be easily associated to printing methods.

In the near future, it is expected flexible sensing devices capable of being incorporated into opto-electronic smart devices such as solar cells, in a way that all these technologies can emerge into a broad range of low-cost and disposable consumer products to our everyday life. The flexibility and conformability of this new generation of sensors will allow them to become part of the Internet of Things (IoT) revolution, providing well-being, satisfaction and comfort to the final users.

Acknowledgments

This work was supported by FEDER funds, through the COMPETE 2020 Program, and national funds, through the Fundação para Ciência e Tecnologia (FCT), under the projects POCI-01-0145-FEDER-007688 (Reference UID/CTM/50025). The authors also acknowledge funding from the European Commission through the projects 1D-NEON (H2020-NMP-2015, grant 685758-21D) and BET-EU (H2020-TWINN-2015, grant 692373), as well as from the European Research Council through the Starting Grant given to P. Barquinha (TREND, grant 716510). The work was also partially funded by the Nanomark collaborative project between INCM (Imprensa Nacional - Casa da Moeda) and CENIMAT/i3N. D. Nunes and A. Pimentel acknowledge funding from FCT through the grants SFRH/BPD/84215/2012 and SFRH/BPD/76992/2011, respectively.

6. References

[1] Li J-Y, Xu Q, Li G, Yin Y-X, Wan L-J and Guo Y-G 2017 Research progress regarding Si-based anode materials towards practical application in high energy density Li-ion batteries *Materials Chemistry Frontiers* **1** 1691-708

[2] Nunes D, Vilarigues M, Correia J B and Carvalho P A 2012 Nickel–carbon nanocomposites: Synthesis, structural changes and strengthening mechanisms *Acta Materialia* **60** 737-47

[3] Khan I, Saeed K and Khan I 2017 Nanoparticles: Properties, applications and toxicities *Arabian Journal of Chemistry*

[4] Zhang Q, Zhang K, Xu D, Yang G, Huang H, Nie F, Liu C and Yang S 2014 CuO nanostructures: Synthesis, characterization, growth mechanisms, fundamental properties, and applications *Progress in Materials Science* **60** 208-337

[5] Vaseem M, Umar A and Hahn Y-B 2010 ZnO nanoparticles: growth, properties, and applications *Metal oxide nanostructures and their applications* **5** 1-36

[6] Roduner E 2006 Size matters: why nanomaterials are different *Chemical Society Reviews* **35** 583-92

[7] Pitkethly M J 2004 Nanomaterials – the driving force *Materials Today* **7** 20-9

[8] Yu R, Lin Q, Leung S-F and Fan Z 2012 Nanomaterials and nanostructures for efficient light absorption and photovoltaics *Nano Energy* **1** 57-72

[9] Nunes D, Pimentel A, Santos L, Barquinha P, Fortunato E and Martins R 2017 Photocatalytic TiO2 Nanorod Spheres and Arrays Compatible with Flexible Applications *Catalysts* **7** 60

[10] Nunes D, Pimentel A, Pinto J V, Calmeiro T R, Nandy S, Barquinha P, Pereira L, Carvalho P A, Fortunato E and Martins R 2016 Photocatalytic behavior of TiO2 films synthesized by microwave irradiation *Catalysis Today* **278, Part 2** 262-70

[11] Nunes D, Pimentel A, Barquinha P, Carvalho P A, Fortunato E and Martins R 2014 Cu2O polyhedral nanowires produced by microwave irradiation *J. Mater. Chem. C* **2** 6097-103

[12] Wu H B, Chen J S, Hng H H and Wen Lou X 2012 Nanostructured metal oxide-based materials as advanced anodes for lithium-ion batteries *Nanoscale* **4** 2526-42

[13] Pimentel A, Samouco A, Nunes D, Araújo A, Martins R and Fortunato E 2017 Ultra-Fast Microwave Synthesis of ZnO Nanorods on Cellulose Substrates for UV Sensor Applications *Materials* **10** 1308

[14] Pimentel A, Rodrigues J, Duarte P, Nunes D, Costa F M, Monteiro T, Martins R and Fortunato E 2015 Effect of solvents on ZnO nanostructures synthesized by solvothermal method assisted by microwave radiation: a photocatalytic study *Journal of Materials Science* **50** 5777-87

[15] Kolmakov A and Moskovits M 2004 Chemical sensing and catalysis by one-dimensional metal-oxide nanostructures *Annu. Rev. Mater. Res.* **34** 151-80

[16] Devan R S, Patil R A, Lin J-H and Ma Y-R 2012 One-Dimensional Metal-Oxide Nanostructures: Recent Developments in Synthesis, Characterization, and Applications *Advanced Functional Materials* **22** 3326-70

[17] Yu X, Marks T J and Facchetti A 2016 Metal oxides for optoelectronic applications *Nat Mater* **15** 383-96

[18] Fernández-García M and Rodriguez J A 2011 *Encyclopedia of Inorganic and Bioinorganic Chemistry*: John Wiley & Sons, Ltd)

[19] Guo T, Yao M-S, Lin Y-H and Nan C-W 2015 A comprehensive review on synthesis methods for transition-metal oxide nanostructures *CrystEngComm* **17** 3551-85

[20] Walia S, Balendhran S, Nili H, Zhuiykov S, Rosengarten G, Wang Q H, Bhaskaran M, Sriram S, Strano M S and Kalantar-zadeh K 2013 Transition metal oxides – Thermoelectric properties *Progress in Materials Science* **58** 1443-89

[21] Wang C, Yin L, Zhang L, Xiang D and Gao R 2010 Metal Oxide Gas Sensors: Sensitivity and Influencing Factors *Sensors* **10** 2088

[22] Phanichphant S 2014 Semiconductor Metal Oxides as Hydrogen Gas Sensors *Procedia Engineering* **87** 795-802

[23] Lin J, Heo Y-U, Nattestad A, Sun Z, Wang L, Kim J H and Dou S X 2014 3D hierarchical rutile TiO 2 and metal-free organic sensitizer producing dye-sensitized solar cells 8.6% conversion efficiency *Scientific reports* **4** 5769

[24] Kardarian K, Nunes D, Sberna P M, Ginsburg A, Keller D A, Pinto J V, Deuermeier J, Anderson A Y, Zaban A and Martins R 2016 Effect of Mg doping on Cu 2 O thin films and their behavior on the TiO 2/Cu 2 O heterojunction solar cells *Solar Energy Materials and Solar Cells* **147** 27-36

[25] Pavan M, Rühle S, Ginsburg A, Keller D A, Barad H-N, Sberna P M, Nunes D, Martins R, Anderson A Y and Zaban A 2015 TiO 2/Cu 2 O all-oxide heterojunction solar cells produced by spray pyrolysis *Solar Energy Materials and Solar Cells* **132** 549-56

[26] Fukai Y, Kondo Y, Mori S and Suzuki E 2007 Highly efficient dye-sensitized SnO2 solar cells having sufficient electron diffusion length *Electrochemistry Communications* **9** 1439-43

[27] Dinh N N, Oanh N T T, Long P D, Bernard M C and Hugot-Le Goff A 2003 Electrochromic properties of TiO2 anatase thin films prepared by a dipping sol–gel method *Thin Solid Films* **423** 70-6

[28] Santos L, Wojcik P, Pinto J V, Elangovan E, Viegas J, Pereira L, Martins R and Fortunato E 2015 Structure and Morphologic Influence of WO3 Nanoparticles on the Electrochromic Performance of Dual-Phase a-WO3/WO3 Inkjet Printed Films *Advanced Electronic Materials* **1** 1400002-n/a

[29] Santos L, Neto J, Crespo A, Baião P, Barquinha P, Pereira L, Martins R and Fortunato E 2015 *Electroplating of Nanostructures*: InTech)

[30] Park M S, Wang G X, Kang Y M, Wexler D, Dou S X and Liu H K 2007 Preparation and electrochemical properties of SnO2 nanowires for application in lithium-ion batteries *Angewandte Chemie* **119** 764-7

[31] Liu Y and Yang Y 2016 Recent Progress of TiO2-Based Anodes for Li Ion Batteries *Journal of Nanomaterials* **2016** 15

[32] Wang X, Cao X, Bourgeois L, Guan H, Chen S, Zhong Y, Tang D M, Li H, Zhai T and Li L 2012 N-Doped Graphene-SnO2 Sandwich Paper for High-Performance Lithium-Ion Batteries *Advanced Functional Materials* **22** 2682-90

[33] Subalakshmi P and Sivashanmugam A 2017 CuO nano hexagons, an efficient energy storage material for Li- ion battery application *Journal of Alloys and Compounds* **690** 523-31

[34] Nakata K and Fujishima A 2012 TiO2 photocatalysis: Design and applications *Journal of Photochemistry and Photobiology C: Photochemistry Reviews* **13** 169-89

[35] Schneider J, Matsuoka M, Takeuchi M, Zhang J, Horiuchi Y, Anpo M and Bahnemann D W 2014 Understanding TiO2 Photocatalysis: Mechanisms and Materials *Chemical Reviews* **114** 9919-86

[36] Jin X, Xu J, Wang X, Xie Z, Liu Z, Liang B, Chen D and Shen G 2014 Flexible TiO2/cellulose acetate hybrid film as a recyclable photocatalyst *RSC Advances* **4** 12640-8

[37] Sunada K, Kikuchi Y, Hashimoto K and Fujishima A 1998 Bactericidal and Detoxification Effects of TiO2 Thin Film Photocatalysts *Environmental Science & Technology* **32** 726-8

[38] Vukoje I, Kovač T, Džunuzović J, Džunuzović E, Lončarević D, Ahrenkiel S P and Nedeljković J M 2016 Photocatalytic Ability of Visible-Light-Responsive TiO2 Nanoparticles *The Journal of Physical Chemistry C* **120** 18560-9

[39] Bai J and Zhou B 2014 Titanium Dioxide Nanomaterials for Sensor Applications *Chemical Reviews* **114** 10131-76

[40] Bernacka-Wojcik I, Senadeera R, Wojcik P J, Silva L B, Doria G, Baptista P, Aguas H, Fortunato E and Martins R 2010 Inkjet printed and "doctor blade" TiO2 photodetectors for DNA biosensors *Biosensors and Bioelectronics* **25** 1229-34

[41] Zhang J, Liu J, Peng Q, Wang X and Li Y 2006 Nearly monodisperse Cu2O and CuO nanospheres: preparation and applications for sensitive gas sensors *Chemistry of materials* **18** 867-71

[42] Raible I, Burghard M, Schlecht U, Yasuda A and Vossmeyer T 2005 V2O5 nanofibres: novel gas sensors with extremely high sensitivity and selectivity to amines *Sensors and Actuators B: Chemical* **106** 730-5

[43] Ansari A A, Alhoshan M, Alsalhi M and Aldwayyan A 2010 *Biosensors*: InTech)

[44] Tiemann M 2007 Porous Metal Oxides as Gas Sensors *Chemistry – A European Journal* **13** 8376-88

[45] Chen Z and Lu C 2005 Humidity sensors: a review of materials and mechanisms *Sensor letters* **3** 274-95

[46] Liu Z, Li F, Li S, Hu C, Wang W, Wang F, Lin F and Wang H 2015 Fabrication of UV photodetector on TiO2/diamond film *Scientific reports* **5**

[47] Solanki P R, Kaushik A, Agrawal V V and Malhotra B D 2011 Nanostructured metal oxide-based biosensors *Npg Asia Materials* **3** 17

[48] Liu A 2008 Towards development of chemosensors and biosensors with metal-oxide-based nanowires or nanotubes *Biosensors and Bioelectronics* **24** 167-77

[49] Dey A 2018 Semiconductor metal oxide gas sensors: A review *Materials Science and Engineering: B* **229** 206-17

[50] Huang J and Wan Q 2009 Gas sensors based on semiconducting metal oxide one-dimensional nanostructures *Sensors* **9** 9903-24

[51] Afzal A, Cioffi N, Sabbatini L and Torsi L 2012 NOx sensors based on semiconducting metal oxide nanostructures: progress and perspectives *Sensors and Actuators B: Chemical* **171** 25-42

[52] Liu X, Cheng S, Liu H, Hu S, Zhang D and Ning H 2012 A Survey on Gas Sensing Technology *Sensors* **12** 9635

[53] Mishra S, Ghanshyam C, Ram N, Bajpai R P and Bedi R K 2004 Detection mechanism of metal oxide gas sensor under UV radiation *Sensors and Actuators B: Chemical* **97** 387-90

[54] Wan Q, Li Q, Chen Y, Wang T-H, He X, Li J and Lin C 2004 Fabrication and ethanol sensing characteristics of ZnO nanowire gas sensors *Applied Physics Letters* **84** 3654-6

[55] Wan X, Wang J, Zhu L and Tang J 2014 Gas sensing properties of Cu2O and its particle size and morphology-dependent gas-detection sensitivity *Journal of Materials Chemistry A* **2** 13641-7

[56] Tang H, Prasad K, Sanjines R and Levy F 1995 TiO2 anatase thin films as gas sensors *Sensors and Actuators-B-Chemical Biochemical Sensors* **26** 71-5

[57] Li X-L, Lou T-J, Sun X-M and Li Y-D 2004 Highly sensitive WO3 hollow-sphere gas sensors *Inorganic chemistry* **43** 5442-9

[58] Seal S and Shukla S 2002 Nanocrystalline SnO gas sensors in view of surface reactions and modifications *JOM* **54** 35-8

[59] Raj A D, Pazhanivel T, Kumar P S, Mangalaraj D, Nataraj D and Ponpandian N 2010 Self assembled V2O5 nanorods for gas sensors *Current Applied Physics* **10** 531-7

[60] Staerz A, Berthold C, Russ T, Wicker S, Weimar U and Barsan N 2016 The oxidizing effect of humidity on WO3 based sensors *Sensors and Actuators B: Chemical* **237** 54-8

[61] Zhang J, Qin Z, Zeng D and Xie C 2017 Metal-oxide-semiconductor based gas sensors: screening, preparation, and integration *Physical Chemistry Chemical Physics* **19** 6313-29

[62] Wetchakun K, Samerjai T, Tamaekong N, Liewhiran C, Siriwong C, Kruefu V, Wisitsoraat A, Tuantranont A and Phanichphant S 2011 Semiconducting metal oxides as sensors for environmentally hazardous gases *Sensors and Actuators B: Chemical* **160** 580-91

[63] Steele J J, Taschuk M T and Brett M J 2008 Nanostructured Metal Oxide Thin Films for Humidity Sensors *IEEE Sensors Journal* **8** 1422-9

[64] Su P-G and Huang L-N 2007 Humidity sensors based on TiO2 nanoparticles/polypyrrole composite thin films *Sensors and Actuators B: Chemical* **123** 501-7

[65] Farahani H, Wagiran R and Hamidon M N 2014 Humidity sensors principle, mechanism, and fabrication technologies: a comprehensive review *Sensors* **14** 7881-939

[66] Yang M-Z, Dai C-L and Wu C-C 2014 Sol-Gel Zinc Oxide Humidity Sensors Integrated with a Ring Oscillator Circuit On-a-Chip *Sensors* **14** 20360

[67] Chen Z, Xiaohong W, Xuanlin K and Sixing X 2016 High performance flexible ultraviolet photodetectors based on TiO 2 /graphene hybrid for irradiation monitoring applications *Journal of Micromechanics and Microengineering* **26** 075003

[68] Tian W, Lu H and Li L 2015 Nanoscale ultraviolet photodetectors based on onedimensional metal oxide nanostructures *Nano Research* **8** 382-405

[69] Alsultany F H, Hassan Z and Ahmed N M 2016 A high-sensitivity, fast-response, rapid-recovery UV photodetector fabricated based on catalyst-free growth of ZnO nanowire networks on glass substrate *Optical Materials* **60** 30-7

[70] Fu Y and Cao W 2006 Preparation of transparent TiO2 nanocrystalline film for UV sensor *Chinese Science Bulletin* **51** 1657-61

[71] Pimentel A, Ferreira S, Nunes D, Calmeiro T, Martins R and Fortunato E 2016 Microwave Synthesized ZnO Nanorod Arrays for UV Sensors: A Seed Layer Annealing Temperature Study *Materials* **9** 299

[72] Huang Y, Lin J, Li L, Xu L, Wang W, Zhang J, Xu X, Zou J and Tang C 2015 High performance UV light photodetectors based on Sn-nanodot-embedded SnO2 nanobelts *Journal of Materials Chemistry C* **3** 5253-8

[73] Liu K, Sakurai M and Aono M 2010 ZnO-Based Ultraviolet Photodetectors *Sensors* **10** 8604

[74] Mohanty S P and Kougianos E 2006 Biosensors: a tutorial review *IEEE Potentials* **25** 35-40

[75] Martins T D, Ribeiro A C C, de Camargo H S, da Costa Filho P A, Cavalcante H P M and Dias D L 2013 *State of the Art in Biosensors-General Aspects*: InTech)

[76] Hasanzadeh M, Shadjou N and de la Guardia M 2015 Iron and iron-oxide magnetic nanoparticles as signal-amplification elements in electrochemical biosensing *TrAC Trends in Analytical Chemistry* **72** 1-9

[77] Arya S K, Wong C C, Jeon Y J, Bansal T and Park M K 2015 Advances in Complementary-Metal–Oxide–Semiconductor-Based Integrated Biosensor Arrays *Chemical Reviews* **115** 5116-58

[78] Mehrotra P 2016 Biosensors and their applications – A review *Journal of Oral Biology and Craniofacial Research* **6** 153-9

[79] Vigneshvar S, Sudhakumari C C, Senthilkumaran B and Prakash H 2016 Recent Advances in Biosensor Technology for Potential Applications – An Overview *Frontiers in Bioengineering and Biotechnology* **4**

[80] Van P T H, Dai D D, Van Duy N, Hoa N D and Van Hieu N 2016 Ultrasensitive NO2 gas sensors using tungsten oxide nanowires with multiple junctions self-assembled on discrete catalyst islands via on-chip fabrication *Sensors and Actuators B: Chemical* **227** 198-203

[81] Alenezi M R, Henley S J and Silva S R P 2015 On-chip Fabrication of High Performance Nanostructured ZnO UV Detectors *Scientific Reports* **5** 8516

[82] Sun Y-F, Liu S-B, Meng F-L, Liu J-Y, Jin Z, Kong L-T and Liu J-H 2012 Metal Oxide Nanostructures and Their Gas Sensing Properties: A Review *Sensors* **12** 2610

[83] Shankar P and Rayappan J B B 2015 Gas sensing mechanism of metal oxides: The role of ambient atmosphere, type of semiconductor and gases-A review *Sci. Lett. J* **4** 126

[84] Nag P and Sujatha Devi P 2015 SnO2 Based Ceramics for Hydrogen Sensors: Current Status and Perspectives *Transactions of the Indian Ceramic Society* **74** 129-47

[85] Hua Z, Li Y, Zeng Y and Wu Y 2018 A theoretical investigation of the power-law response of metal oxide semiconductor gas sensors I: Schottky barrier control *Sensors and Actuators B: Chemical* **255** 1911-9

[86] Geistlinger H 1993 Electron theory of thin-film gas sensors *Sensors and Actuators B: Chemical* **17** 47-60

[87] Morrison S R 1987 Mechanism of semiconductor gas sensor operation *Sensors and Actuators* **11** 283-7

[88] Hung C M, Le D T T and Van Hieu N 2017 On-chip growth of semiconductor metal oxide nanowires for gas sensors: A review *Journal of Science: Advanced Materials and Devices* **2** 263-85

[89] Comini E, Faglia G and Sberveglieri G 2008 *Solid State Gas Sensing*: Springer US)

[90] Morimoto T, Nagao M and Tokuda F 1969 Relation between the amounts of chemisorbed and physisorbed water on metal oxides *The Journal of Physical Chemistry* **73** 243-8

[91] Boyle J F and Jones K A 1977 The effects of CO, water vapor and surface temperature on the conductivity of a SnO2 gas sensor *Journal of Electronic Materials* **6** 717-33

[92] Kuang Q, Lao C, Wang Z L, Xie Z and Zheng L 2007 High-Sensitivity Humidity Sensor Based on a Single SnO2 Nanowire *Journal of the American Chemical Society* **129** 6070-1

[93] Qian J, Peng Z, Shen Z, Zhao Z, Zhang G and Fu X 2016 Positive impedance humidity sensors via single-component materials *Scientific Reports* **6** 25574

[94] Yang H, Ye Q, Zeng R, Zhang J, Yue L, Xu M, Qiu Z-J and Wu D 2017 Stable and Fast-Response Capacitive Humidity Sensors Based on a ZnO Nanopowder/PVP-RGO Multilayer *Sensors (Basel, Switzerland)* **17** 2415

[95] Wang Z, Gu Y, Qi J, Lu S, Li P, Lin P and Zhang Y 2015 Size dependence and UV irradiation tuning of the surface potential in single conical ZnO nanowires *RSC Advances* **5** 42075-80

[96] Soci C, Zhang A, Xiang B, Dayeh S A, Aplin D, Park J, Bao X, Lo Y-H and Wang D 2007 ZnO nanowire UV photodetectors with high internal gain *Nano letters* **7** 1003-9

[97] Kind H, Yan H, Messer B, Law M and Yang P 2002 Nanowire Ultraviolet Photodetectors and Optical Switches *Advanced Materials* **14** 158-60

[98] Tian W, Zhang C, Zhai T, Li S-L, Wang X, Liu J, Jie X, Liu D, Liao M, Koide Y, Golberg D and Bando Y 2014 Flexible Ultraviolet Photodetectors with Broad Photoresponse Based on Branched ZnS-ZnO Heterostructure Nanofilms *Advanced Materials* **26** 3088-93

[99] Fang X, Bando Y, Liao M, Zhai T, Gautam U K, Li L, Koide Y and Golberg D 2010 An Efficient Way to Assemble ZnS Nanobelts as Ultraviolet-Light Sensors with Enhanced Photocurrent and Stability *Advanced Functional Materials* **20** 500-8

[100] Grieshaber D, MacKenzie R, Vörös J and Reimhult E 2008 Electrochemical Biosensors - Sensor Principles and Architectures *Sensors (Basel, Switzerland)* **8** 1400-58

[101] Li B and Logan B E 2004 Bacterial adhesion to glass and metal-oxide surfaces *Colloids and Surfaces B: Biointerfaces* **36** 81-90

[102] Vicente A T, Araújo A, Gaspar D, Santos L, Marques A C, Mendes M J, Pereira L, Fortunato E and Martins R 2017 *Nanostructured Solar Cells*: InTech)

[103] Yanagisawa K and Ovenstone J 1999 Crystallization of Anatase from Amorphous Titania Using the Hydrothermal Technique: Effects of Starting Material and Temperature *The Journal of Physical Chemistry B* **103** 7781-7

[104] Vicente A, Araujo A, Mendes M J, Nunes D, Oliveira M J, Sanchez-Sobrado O, Ferreira M P, Aguas H, Fortunato E and Martins R 2018 Multifunctional cellulose-paper for light harvesting and smart sensing applications *Journal of Materials Chemistry C* **6** 3143-81

[105] Coleman V A and Jagadish C 2006 *Zinc Oxide Bulk, Thin Films and Nanostructures,* (Oxford: Elsevier Science Ltd) pp 1-20

[106] Baruah S and Dutta J 2009 Hydrothermal growth of ZnO nanostructures *Science and Technology of Advanced Materials* **10** 013001

[107] Kumar R, Umar A, Kumar G, Nalwa H S, Kumar A and Akhtar M S 2017 Zinc oxide nanostructure-based dye-sensitized solar cells *Journal of Materials Science* **52** 4743-95

[108] Wen B, Huang Y and Boland J J 2008 Controllable Growth of ZnO Nanostructures by a Simple Solvothermal Process *The Journal of Physical Chemistry C* **112** 106-11

[109] Alenezi M R, Alshammari A S, Jayawardena K D G I, Beliatis M J, Henley S J and Silva S R P 2013 Role of the Exposed Polar Facets in the Performance of Thermally and UV Activated ZnO Nanostructured Gas Sensors *The Journal of Physical Chemistry C* **117** 17850-8

[110] Tong Y, Liu Y, Dong L, Zhao D, Zhang J, Lu Y, Shen D and Fan X 2006 Growth of ZnO Nanostructures with Different Morphologies by Using Hydrothermal Technique *The Journal of Physical Chemistry B* **110** 20263-7

[111] Chang J and Waclawik E R 2012 Facet-controlled self-assembly of ZnO nanocrystals by non-hydrolytic aminolysis and their photodegradation activities *CrystEngComm* **14** 4041-8

[112] Zeng J H, Jin B B and Wang Y F 2009 Facet enhanced photocatalytic effect with uniform single-crystalline zinc oxide nanodisks *Chemical Physics Letters* **472** 90-5

[113] Manthina V and Agrios A G 2016 Single-pot ZnO nanostructure synthesis by chemical bath deposition and their applications *Nano-Structures & Nano-Objects* **7** 1-11

[114] Shaikh S K, Inamdar S I, Ganbavle V V and Rajpure K Y 2016 Chemical bath deposited ZnO thin film based UV photoconductive detector *Journal of Alloys and Compounds* **664** 242-9

[115] Chaaya A A, Bechelany M, Balme S and Miele P 2014 ZnO 1D nanostructures designed by combining atomic layer deposition and electrospinning for UV sensor applications *Journal of Materials Chemistry A* **2** 20650-8

[116] Preda N, Evanghelidis A, Enculescu M, Florica C and Enculescu I 2015 Zinc oxide electroless deposition on electrospun PMMA fiber mats *Materials Letters* **138** 238-42

[117] Di Mauro A, Fragalà M E, Privitera V and Impellizzeri G 2017 ZnO for application in photocatalysis: From thin films to nanostructures *Materials Science in Semiconductor Processing* **69** 44-51

[118] Skompska M and Zarębska K 2014 Electrodeposition of ZnO Nanorod Arrays on Transparent Conducting Substrates–a Review *Electrochimica Acta* **127** 467-88

[119] CATAÑO F A, ALLENDE L W and GÓMEZ H 2015 ELECTRODEPOSITION OF ZnO NANOROD ARRAYS FOR APPLICATION IN PEROVSKITE BASED SOLAR CELLS *Journal of the Chilean Chemical Society* **60** 2940-3

[120] Rodrigues J, Mata D, Pimentel A, Nunes D, Martins R, Fortunato E, Neves A J, Monteiro T and Costa F M 2015 One-step synthesis of ZnO decorated CNT buckypaper composites and their optical and electrical properties *Materials Science and Engineering: B* **195** 38-44

[121] Rodrigues J, Cerqueira A F R, Sousa M G, Santos N F, Pimentel A, Fortunato E, da Cunha A F, Monteiro T and Costa F M 2016 Exploring the potential of laser assisted flow deposition grown ZnO for photovoltaic applications *Materials Chemistry and Physics* **177** 322-9

[122] Pimentel A, Nunes D, Duarte P, Rodrigues J, Costa F M, Monteiro T, Martins R and Fortunato E 2014 Synthesis of Long ZnO Nanorods under Microwave Irradiation or Conventional Heating *The Journal of Physical Chemistry C* **118** 14629-39

[123] Yang J, Lin Y, Meng Y and Liu Y 2012 A two-step route to synthesize highly oriented ZnO nanotube arrays *Ceramics International* **38** 4555-9

[124] Zhu L, Li J, Ye Z, He H, Chen X and Zhao B 2008 Photoluminescence of Ga-doped ZnO nanorods prepared by chemical vapor deposition *Optical Materials* **31** 237-40

[125] Bai S, Chen S, Zhao Y, Guo T, Luo R, Li D and Chen A 2014 Gas sensing properties of Cd-doped ZnO nanofibers synthesized by the electrospinning method *Journal of Materials Chemistry A* **2** 16697-706

[126] Mahpeykar S M, Koohsorkhi J and Ghafoori-fard H 2012 Ultra-fast microwave-assisted hydrothermal synthesis of long vertically aligned ZnO nanowires for dye-sensitized solar cell application *Nanotechnology* **23** 165602

[127] Jia Y, Yu X-Y, Luo T, Zhang M-Y, Liu J-H and Huang X-J 2013 PEG aggregation templated porous ZnO nanostructure: room temperature solution synthesis, pore formation mechanism, and their photoluminescence properties *CrystEngComm* **15** 3647-53

[128] Xu F, Lu Y, Xie Y and Liu Y 2009 Controllable morphology evolution of electrodeposited ZnO nano/micro-scale structures in aqueous solution *Materials & Design* **30** 1704-11

[129] Khajavi M R, Blackwood D J, Cabanero G and Tena-Zaera R 2012 New insight into growth mechanism of ZnO nanowires electrodeposited from nitrate-based solutions *Electrochimica Acta* **69** 181-9

[130] Shi R, Yang P, Wang J, Zhang A, Zhu Y, Cao Y and Ma Q 2012 Growth of flower-like ZnO via surfactant-free hydrothermal synthesis on ITO substrate at low temperature *CrystEngComm* **14** 5996-6003

[131] Pimentel A, Fortunato E, Gonçalves A, Marques A, Águas H, Pereira L, Ferreira I and Martins R 2005 Polycrystalline intrinsic zinc oxide to be used in transparent electronic devices *Thin Solid Films* **487** 212-5

[132] Fortunato E M C, Barquinha P M C, Pimentel A C M B G, Gonçalves A M F, Marques A J S, Pereira L M N and Martins R F P 2005 Fully Transparent ZnO

Thin-Film Transistor Produced at Room Temperature *Advanced Materials* **17** 590-4

[133] Byeong-Yun O, Young-Hwan K, Hee-Jun L, Byoung-Yong K, Hong-Gyu P, Jin-Woo H, Gi-Seok H, Tae-Won K, Kwang-Young K and Dae-Shik S 2011 High-performance ZnO thin-film transistor fabricated by atomic layer deposition *Semiconductor Science and Technology* **26** 085007

[134] Zong X and Zhu R 2017 Zinc oxide nanorod field effect transistor for long-time cellular force measurement *Scientific Reports* **7** 43661

[135] Pauporté T 2018 *The Future of Semiconductor Oxides in Next-Generation Solar Cells*: Elsevier) pp 3-43

[136] Fang J, Fan H, Tian H and Dong G 2015 Morphology control of ZnO nanostructures for high efficient dye-sensitized solar cells *Materials Characterization* **108** 51-7

[137] Duan J, Xiong Q, Wang H, Zhang J and Hu J 2017 ZnO nanostructures for efficient perovskite solar cells *Journal of Materials Science: Materials in Electronics* **28** 60-6

[138] Wang Z L and Song J 2006 Piezoelectric nanogenerators based on zinc oxide nanowire arrays *Science* **312** 242-6

[139] Nour E S, Nur O and Willander M 2017 Zinc oxide piezoelectric nano-generators for low frequency applications *Semiconductor Science and Technology* **32** 064005

[140] Opoku C, Dahiya A S, Oshman C, Cayrel F, Poulin-Vittrant G, Alquier D and Camara N 2015 Fabrication of ZnO Nanowire Based Piezoelectric Generators and Related Structures *Physics Procedia* **70** 858-62

[141] Guo M Y, Fung M K, Fang F, Chen X Y, Ng A M C, Djurišić A B and Chan W K 2011 ZnO and TiO2 1D nanostructures for photocatalytic applications *Journal of Alloys and Compounds* **509** 1328-32

[142] Man M T, Kim J-H, Jeong M S, Do A-T T and Lee H S 2017 Oriented ZnO nanostructures and their application in photocatalysis *Journal of Luminescence* **185** 17-22

[143] Pimentel A, Araújo A, Coelho B, Nunes D, Oliveira M, Mendes M, Águas H, Martins R and Fortunato E 2017 3D ZnO/Ag Surface-Enhanced Raman Scattering on Disposable and Flexible Cardboard Platforms *Materials* **10** 1351

[144] Andreia A, Ana P, Maria João O, Manuel J M, Ricardo F, Elvira F, Hugo Á and Rodrigo M 2017 Direct growth of plasmonic nanorod forests on paper substrates for low-cost flexible 3D SERS platforms *Flexible and Printed Electronics* **2** 014001

[145] Asif M, Danielsson B and Willander M 2015 ZnO Nanostructure-Based Intracellular Sensor *Sensors* **15** 11787

[146] Gupta S K, Joshi A and Kaur M 2010 Development of gas sensors using ZnO nanostructures *Journal of Chemical Sciences* **122** 57-62

[147] Basyooni M A, Shaban M and El Sayed A M 2017 Enhanced Gas Sensing Properties of Spin-coated Na-doped ZnO Nanostructured Films *Scientific Reports* **7** 41716

[148] Iversen K J and Spencer M J S 2013 Effect of ZnO Nanostructure Morphology on the Sensing of H2S Gas *The Journal of Physical Chemistry C* **117** 26106-18

[149] Spencer M J S and Yarovsky I 2010 ZnO Nanostructures for Gas Sensing: Interaction of NO2, NO, O, and N with the ZnO($10\bar{1}0$) Surface *The Journal of Physical Chemistry C* **114** 10881-93

[150] Jońca J, Ryzhikov A, Kahn M L, Fajerwerg K, Chaudret B, Chapelle A, Menini P and Fau P 2014 Shape-controlled ZnO Nanostructures for Gas Sensing Applications *Procedia Engineering* **87** 907-10

[151] Sadek A Z, Choopun S, Wlodarski W, Ippolito S J and Kalantar-zadeh K 2007 Characterization of ZnO Nanobelt-Based Gas Sensor for H₂, NO₂, and Hydrocarbon Sensing *IEEE Sensors Journal* **7** 919-24

[152] Cho P-S, Kim K-W and Lee J-H 2006 NO2 sensing characteristics of ZnO nanorods prepared by hydrothermal method *Journal of Electroceramics* **17** 975-8

[153] Galstyan V, Comini E, Baratto C, Faglia G and Sberveglieri G 2015 Nanostructured ZnO chemical gas sensors *Ceramics International* **41** 14239-44

[154] Dilonardo E, Penza M, Alvisi M, Di Franco C, Palmisano F, Torsi L and Cioffi N 2016 Evaluation of gas-sensing properties of ZnO nanostructures electrochemically doped with Au nanophases *Beilstein Journal of Nanotechnology* **7** 22-31

[155] Li D, Zhang Y, Liu D, Yao S, Liu F, Wang B, Sun P, Gao Y, Chuai X and Lu G 2016 Hierarchical core/shell ZnO/NiO nanoheterojunctions synthesized by ultrasonic spray pyrolysis and their gas-sensing performance *CrystEngComm* **18** 8101-7

[156] Wang C, Cui X, Liu J, Zhou X, Cheng X, Sun P, Hu X, Li X, Zheng J and Lu G 2016 Design of Superior Ethanol Gas Sensor Based on Al-Doped NiO Nanorod-Flowers *ACS Sensors* **1** 131-6

[157] Ghanem S, Telia A, Boukaous C and Aida M S 2015 Humidity sensor characteristics based on ZnO nanostructure grown by sol-gel method *International Journal of Nanotechnology* **12** 697-707

[158] Herrán J, Fernández I, Ochoteco E, Cabañero G and Grande H 2014 The role of water vapour in ZnO nanostructures for humidity sensing at room temperature *Sensors and Actuators B: Chemical* **198** 239-42

[159] 2015 High-performance self-powered/active humidity sensing of Fe-doped ZnO nanoarray nanogenerator *Sensors and Actuators B: Chemical* **213** 382

[160] Yuan Q, Li N, Tu J, Li X, Wang R, Zhang T and Shao C 2010 Preparation and humidity sensitive property of mesoporous ZnO–SiO2 composite *Sensors and Actuators B: Chemical* **149** 413-9

[161] Gu L, Zheng K, Zhou Y, Li J, Mo X, Patzke G R and Chen G 2011 Humidity sensors based on ZnO/TiO2 core/shell nanorod arrays with enhanced sensitivity *Sensors and Actuators B: Chemical* **159** 1-7

[162] Montesperelli G, Pumo A, Traversa E, Gusmano, Bearzotti A, Montenero A and Gnappi G 1995 Sol—gel processed TiO2-based thin films as innovative humidity sensors *Sensors and Actuators B: Chemical* **25** 705-9

[163] Kim H K, Dattatraya Sathaye S, Hwang Y K, Jhung S H, Hwang J S, Kwon S H, Park S-E and Chang J 2005 *Humidity Sensing Properties of Nanoporous TiO2-SnO2 Ceramic Sensors* vol 26

[164] Park T, Lee K E, Kim N, Oh Y, Yoo J-K and Um M-K 2017 Aspect ratio-controlled ZnO nanorods for highly sensitive wireless ultraviolet sensor applications *Journal of Materials Chemistry C* **5** 12256-63

[165] Dong M, Wang Y, Li Z, Weng Z and Yu N 2018 Simple Fabrication of Homogeneous ZnO Core/Shell Nanorod Arrays for Ultraviolet Photodetectors *Journal of Nanoscience and Nanotechnology* **18** 5686-91

[166] Makhlouf H, Karam C, Lamouchi A, Tingry S, Miele P, Habchi R, Chtourou R and Bechelany M 2018 Analysis of ultraviolet photo-response of ZnO nanostructures prepared by electrodeposition and atomic layer deposition *Applied Surface Science* **444** 253-9

[167] Shewale P S, Lee S H and Yu Y S 2018 UV sensitive pulsed laser deposited ZnO thin films: Influence of growth temperature *Journal of Alloys and Compounds* **744** 849-58

[168] Yi N, Zhiming Z, Feng T and Xiaosheng F 2018 Novel Transparent and Self-Powered UV Photodetector Based on Crossed ZnO Nanofiber Array Homojunction *Small* **14** 1703754

[169] Dalvand R, Mahmud S and Shabannia R 2018 Fabrication of UV photodetector using needle-shaped ZnO nanostructure arrays prepared on porous silicon substrate by a facile low-temperature method *Journal of Materials Science: Materials in Electronics* **29** 4999-5008

[170] Kenanakis G, Vernardou D, Koudoumas E, Kiriakidis G and Katsarakis N 2007 Ozone sensing properties of ZnO nanostructures grown by the aqueous chemical growth technique *Sensors and Actuators B: Chemical* **124** 187-91

[171] Suo B, Weiwei W, Yong Q, Nuanyang C, J. B D and Xudong W 2011 High-Performance Integrated ZnO Nanowire UV Sensors on Rigid and Flexible Substrates *Advanced Functional Materials* **21** 4464-9

[172] Noushin N, Renheng B, Fan W, Lan F and Antonio T 2015 Ultraporous Electron-Depleted ZnO Nanoparticle Networks for Highly Sensitive Portable Visible-Blind UV Photodetectors *Advanced Materials* **27** 4336-43

[173] AlZoubi T, Qutaish H, Al-Shawwa E a and Hamzawy S 2018 Enhanced UV-light detection based on ZnO nanowires/graphene oxide hybrid using cost-effective low temperature hydrothermal process *Optical Materials* **77** 226-32

[174] Duan L, He F, Tian Y, Sun B, Fan J, Yu X, Ni L, Zhang Y, Chen Y and Zhang W 2017 Fabrication of Self-Powered Fast-Response Ultraviolet Photodetectors Based on Graphene/ZnO:Al Nanorod-Array-Film Structure with Stable Schottky Barrier *ACS Applied Materials & Interfaces* **9** 8161-8

[175] Liu H, Sun Q, Xing J, Zheng Z, Zhang Z, Lü Z and Zhao K 2015 Fast and Enhanced Broadband Photoresponse of a ZnO Nanowire Array/Reduced Graphene Oxide Film Hybrid Photodetector from the Visible to the Near-Infrared Range *ACS Applied Materials & Interfaces* **7** 6645-51

[176] Gallay P, Tosi E, Madrid R, Tirado M and Comedi D 2016 Glucose biosensor based on functionalized ZnO nanowire/graphite films dispersed on a Pt electrode *Nanotechnology* **27** 425501

[177] Wang J X, Sun X W, Wei A, Lei Y, Cai X P, Li C M and Dong Z L 2006 Zinc oxide nanocomb biosensor for glucose detection *Applied Physics Letters* **88** 233106

[178] Viter R, Jekabsons K, Kalnina Z, Poletaev N, Hsu S H and Riekstina U 2016 Bioanalytical system for detection of cancer cells with photoluminescent ZnO nanorods *Nanotechnology* **27** 465101

[179] Shanmugam N R, Muthukumar S and Prasad S 2017 A review on ZnO-based electrical biosensors for cardiac biomarker detection *Future Science OA* **3** FSO196

[180] Mohammed A M, Ibraheem I J, Obaid A S and Bououdina M 2017 Nanostructured ZnO-based biosensor: DNA immobilization and hybridization *Sensing and Bio-Sensing Research* **15** 46-52

[181] Wahab H A, Salama A A, El Saeid A A, Willander M, Nur O and Battisha I K 2018 Zinc oxide nano-rods based glucose biosensor devices fabrication *Results in Physics* **9** 809-14

[182] Shanmugam N R, Muthukumar S and Prasad S 2016 Ultrasensitive and low-volume point-of-care diagnostics on flexible strips – a study with cardiac troponin biomarkers *Scientific Reports* **6** 33423

[183] Tan C M, Arshad M K M, Fathil M F M, Adzhri R, N M N N M, Ruslinda A R, Ibau C and Hashim U 2016 Interdigitated Electrodes integrated with zinc oxide nanoparticles for Cardiac Troponin I biomarker detection. In: *2016 IEEE International Conference on Semiconductor Electronics (ICSE),* pp 220-3

[184] Bhat S S, Qurashi A and Khanday F A 2017 ZnO nanostructures based biosensors for cancer and infectious disease applications: Perspectives, prospects and promises *TrAC Trends in Analytical Chemistry* **86** 1-13

[185] Rui Q, Komori K, Tian Y, Liu H, Luo Y and Sakai Y 2010 Electrochemical biosensor for the detection of H2O2 from living cancer cells based on ZnO nanosheets *Analytica Chimica Acta* **670** 57-62

[186] Negahdary M, Rezaei-Zarchi S, Rousta N and Samei Pour S 2012 Direct Electron Transfer of Cytochrome c on ZnO Nanoparticles Modified Carbon Paste Electrode *ISRN Biophysics* **2012** 6

[187] Rathee D, Arya S and Kumar M 2011 Analysis of TiO2 for microelectronic applications: effect of deposition methods on their electrical properties *Frontiers of Optoelectronics in China* **4** 349-58

[188] Di Paola A, Bellardita M and Palmisano L 2013 Brookite, the least known TiO2 photocatalyst *Catalysts* **3** 36-73

[189] Zhang H, Finnegan M and Banfield J F 2001 Preparing Single-Phase Nanocrystalline Anatase from Amorphous Titania with Particle Sizes Tailored by Temperature *Nano Letters* **1** 81-5

[190] Allen N S, Mahdjoub N, Vishnyakov V, Kelly P J and Kriek R J The effect of crystalline phase (anatase, brookite and rutile) and size on the photocatalytic activity of calcined polymorphic titanium dioxide (TiO2) *Polymer Degradation and Stability*

[191] Rocquefelte X, Goubin F, Koo H-J, Whangbo M-H and Jobic S 2004 Investigation of the Origin of the Empirical Relationship between Refractive Index and Density on the Basis of First Principles Calculations for the Refractive Indices of Various TiO2 Phases *Inorganic Chemistry* **43** 2246-51

[192] Pimentel A, Nunes D, Pereira S, Martins R and Fortunato E 2016 *Semiconductor Photocatalysis - Materials, Mechanisms and Applications,* ed W Cao (Rijeka: InTech) p Ch. 03

[193] Reyes-Coronado D, Rodríguez-Gattorno G, Espinosa-Pesqueira M, Cab C, De Coss R and Oskam G 2008 Phase-pure TiO2 nanoparticles: anatase, brookite and rutile *Nanotechnology* **19** 145605

[194] Khan M M, Ansari S A, Pradhan D, Ansari M O, Han D H, Lee J and Cho M H 2014 Band gap engineered TiO2 nanoparticles for visible light induced

photoelectrochemical and photocatalytic studies *Journal of Materials Chemistry A* **2** 637-44

[195] George S, Pokhrel S, Ji Z, Henderson B L, Xia T, Li L, Zink J I, Nel A E and Mädler L 2011 Role of Fe Doping in Tuning the Band Gap of TiO2 for the Photo-Oxidation-Induced Cytotoxicity Paradigm *Journal of the American Chemical Society* **133** 11270-8

[196] Umebayashi T, Yamaki T, Itoh H and Asai K 2002 Band gap narrowing of titanium dioxide by sulfur doping *Applied Physics Letters* **81** 454-6

[197] Dueñas S, Castán H, García H, Andrés E S, Toledano-Luque M, Mártil I, González-Díaz G, Kukli K, Uustare T and Aarik J 2005 A comparative study of the electrical properties of TiO 2 films grown by high-pressure reactive sputtering and atomic layer deposition *Semiconductor Science and Technology* **20** 1044

[198] Wypych A, Bobowska I, Tracz M, Opasinska A, Kadlubowski S, Krzywania-Kaliszewska A, Grobelny J and Wojciechowski P 2014 Dielectric Properties and Characterisation of Titanium Dioxide Obtained by Different Chemistry Methods *Journal of Nanomaterials* **2014** 9

[199] Maziarz W, Kusior A and Trenczek-Zajac A 2016 Nanostructured TiO2-based gas sensors with enhanced sensitivity to reducing gases *Beilstein journal of nanotechnology* **7** 1718

[200] Mo S-D and Ching W Y 1995 Electronic and optical properties of three phases of titanium dioxide: Rutile, anatase, and brookite *Physical Review B* **51** 13023-32

[201] Antonelli D M and Ying J Y 1995 Synthesis of hexagonally packed mesoporous TiO2 by a modified sol–gel method *Angewandte Chemie International Edition in English* **34** 2014-7

[202] Xiang L and Zhao X 2017 Wet-Chemical Preparation of TiO(2)-Based Composites with Different Morphologies and Photocatalytic Properties *Nanomaterials* **7** 310

[203] Verma R, Gangwar J and Srivastava A K 2017 Multiphase TiO 2 nanostructures: a review of efficient synthesis, growth mechanism, probing capabilities, and applications in bio-safety and health *RSC Advances* **7** 44199-224

[204] Wu J-M, Shih H C, Wu W-T, Tseng Y-K and Chen I C 2005 Thermal evaporation growth and the luminescence property of TiO2 nanowires *Journal of Crystal Growth* **281** 384-90

[205] Boyadzhiev S, Georgieva V and Rassovska M 2010 Characterization of reactive sputtered TiO2 thin films for gas sensor applications. In: *Journal of Physics: Conference Series*: IOP Publishing) p 012040

[206] Jiang L C and Zhang W D 2009 Electrodeposition of TiO2 nanoparticles on multiwalled carbon nanotube arrays for hydrogen peroxide sensing *Electroanalysis* **21** 988-93

[207] Lee D, Rho Y, Allen F I, Minor A M, Ko S H and Grigoropoulos C P 2013 Synthesis of hierarchical TiO2 nanowires with densely-packed and omnidirectional branches *Nanoscale* **5** 11147-52

[208] Yu J, Wang Y and Xiao W 2013 Enhanced photoelectrocatalytic performance of SnO2/TiO2 rutile composite films *Journal of Materials Chemistry A* **1** 10727-35

[209] Zhao X, Liu M and Zhu Y 2007 Fabrication of porous TiO2 film via hydrothermal method and its photocatalytic performances *Thin Solid Films* **515** 7127-34

[210] Chen Q, Qian Y, Chen Z, Wu W, Chen Z, Zhou G and Zhang Y 1995 Hydrothermal epitaxy of highly oriented TiO2 thin films on silicon *Applied Physics Letters* **66** 1608-10

[211] Li G, Wang G and Hong J 1999 Synthesis and characterization of rutile TiO 2 nanowhiskers *Journal of materials research* **14** 3346-54

[212] Zhang X, Wang Y, Liu B, Sang Y and Liu H 2017 Heterostructures construction on TiO2 nanobelts: A powerful tool for building high-performance photocatalysts *Applied Catalysis B: Environmental* **202** 620-41

[213] Yang H G and Zeng H C 2004 Preparation of Hollow Anatase TiO2 Nanospheres via Ostwald Ripening *The Journal of Physical Chemistry B* **108** 3492-5

[214] Ovenstone J and Yanagisawa K 1999 Effect of Hydrothermal Treatment of Amorphous Titania on the Phase Change from Anatase to Rutile during Calcination *Chemistry of Materials* **11** 2770-4

[215] Panigrahi S, Jana S, Calmeiro T, Nunes D, Martins R and Fortunato E 2017 Imaging the Anomalous Charge Distribution Inside CsPbBr3 Perovskite Quantum Dots Sensitized Solar Cells *ACS Nano* **11** 10214-21

[216] Mor G K, Shankar K, Paulose M, Varghese O K and Grimes C A 2006 Use of highly-ordered TiO2 nanotube arrays in dye-sensitized solar cells *Nano letters* **6** 215-8

[217] Guan K 2005 Relationship between photocatalytic activity, hydrophilicity and self-cleaning effect of TiO2/SiO2 films *Surface and Coatings Technology* **191** 155-60

[218] Bozzi A, Yuranova T and Kiwi J 2005 Self-cleaning of wool-polyamide and polyester textiles by TiO2-rutile modification under daylight irradiation at ambient temperature *Journal of Photochemistry and Photobiology A: Chemistry* **172** 27-34

[219] Ni M, Leung M K, Leung D Y and Sumathy K 2007 A review and recent developments in photocatalytic water-splitting using TiO2 for hydrogen production *Renewable and Sustainable Energy Reviews* **11** 401-25

[220] Yu J, Low J, Xiao W, Zhou P and Jaroniec M 2014 Enhanced photocatalytic CO2-reduction activity of anatase TiO2 by coexposed {001} and {101} facets *Journal of the American Chemical Society* **136** 8839-42

[221] Liu L, Zhao H, Andino J M and Li Y 2012 Photocatalytic CO2 reduction with H2O on TiO2 nanocrystals: Comparison of anatase, rutile, and brookite polymorphs and exploration of surface chemistry *Acs Catalysis* **2** 1817-28

[222] Ferroni M, Guidi V, Martinelli G, Faglia G, Nelli P and Sberveglieri G 1996 Characterization of a nanosized TiO2 gas sensor *Nanostructured materials* **7** 709-18

[223] Mun K-S, Alvarez S D, Choi W-Y and Sailor M J 2010 A stable, label-free optical interferometric biosensor based on TiO2 nanotube arrays *ACS Nano* **4** 2070-6

[224] Cao C, Hu C, Wang X, Wang S, Tian Y and Zhang H 2011 UV sensor based on TiO2 nanorod arrays on FTO thin film *Sensors and Actuators B: Chemical* **156** 114-9

[225] Luttrell T, Halpegamage S, Tao J, Kramer A, Sutter E and Batzill M 2014 Why is anatase a better photocatalyst than rutile? - Model studies on epitaxial TiO(2) films *Scientific Reports* **4** 4043

[226] Kyu R D, Seok C W, Hoon A S, Harim J and Hak K J 2013 One-step Synthesis of Vertically Aligned Anatase Thornbush-like TiO2 Nanowire Arrays on Transparent Conducting Oxides for Solid-State Dye-Sensitized Solar Cells *ChemSusChem* **6** 1384-91

[227] Luttrell T, Halpegamage S, Tao J, Kramer A, Sutter E and Batzill M 2014 Why is anatase a better photocatalyst than rutile? - Model studies on epitaxial TiO2 films *Scientific Reports* **4** 4043

[228] Nakajima H, Mori T, Shen Q and Toyoda T 2005 Photoluminescence study of mixtures of anatase and rutile TiO2 nanoparticles: Influence of charge transfer between the nanoparticles on their photoluminescence excitation bands *Chemical Physics Letters* **409** 81-4

[229] Wang Y, Li L, Huang X, Li Q and Li G 2015 New insights into fluorinated TiO2 (brookite, anatase and rutile) nanoparticles as efficient photocatalytic redox catalysts *RSC Advances* **5** 34302-13

[230] Xie T, Sullivan N, Steffens K, Wen B, Liu G, Debnath R, Davydov A, Gomez R and Motayed A 2015 UV-assisted room-temperature chemiresistive NO2 sensor based on TiO2 thin film *Journal of Alloys and Compounds* **653** 255-9

[231] Galstyan V 2017 Porous TiO2-Based Gas Sensors for Cyber Chemical Systems to Provide Security and Medical Diagnosis *Sensors* **17** 2947

[232] Liu C, Lu H, Zhang J, Gao J, Zhu G, Yang Z, Yin F and Wang C 2018 Crystal facet-dependent p-type and n-type sensing responses of TiO2 nanocrystals *Sensors and Actuators B: Chemical* **263** 557-67

[233] Zhu Z, Lin S-J, Wu C-H and Wu R-J 2018 Synthesis of TiO2 nanowires for rapid NO2 detection *Sensors and Actuators A: Physical* **272** 288-94

[234] Seo M-H, Yuasa M, Kida T, Huh J-S, Shimanoe K and Yamazoe N 2009 Gas sensing characteristics and porosity control of nanostructured films composed of TiO2 nanotubes *Sensors and Actuators B: Chemical* **137** 513-20

[235] Alberti A, Renna L, Sanzaro S, Smecca E, Mannino G, Bongiorno C, Galati C, Gervasi L, Santangelo A and La Magna A 2018 Innovative spongy TiO2 layers

for gas detection at low working temperature *Sensors and Actuators B: Chemical* **259** 658-67

[236] Ruiz A M, Sakai G, Cornet A, Shimanoe K, Morante J R and Yamazoe N 2003 Cr-doped TiO2 gas sensor for exhaust NO2 monitoring *Sensors and Actuators B: Chemical* **93** 509-18

[237] Dario B, Michael P, Carlo C, Paul M and 2Alessandro M 2008 Gold Nanoparticle-Doped TiO2 Semiconductor Thin Films: Gas Sensing Properties *Advanced Functional Materials* **18** 3843-9

[238] Carney C M, Yoo S and Akbar S A 2005 TiO2–SnO2 nanostructures and their H2 sensing behavior *Sensors and Actuators B: Chemical* **108** 29-33

[239] Gong M, Li Y, Guo Y, Lv X and Dou X 2018 2D TiO2 nanosheets for ultrasensitive humidity sensing application benefited by abundant surface oxygen vacancy defects *Sensors and Actuators B: Chemical* **262** 350-8

[240] Lin W-D, Liao C-T, Chang T-C, Chen S-H and Wu R-J 2015 Humidity sensing properties of novel graphene/TiO2 composites by sol–gel process *Sensors and Actuators B: Chemical* **209** 555-61

[241] Su P-G and Wang C-P 2008 Flexible humidity sensor based on TiO2 nanoparticles-polypyrrole-poly-[3-(methacrylamino)propyl] trimethyl ammonium chloride composite materials *Sensors and Actuators B: Chemical* **129** 538-43

[242] Ali Hooshiar Z and Somayye M 2011 Silver Doped Titanium Dioxide Humidity Sensor *IOP Conference Series: Materials Science and Engineering* **17** 012015

[243] Buvailo A I, Xing Y, Hines J, Dollahon N and Borguet E 2011 TiO2/LiCl-Based Nanostructured Thin Film for Humidity Sensor Applications *ACS Applied Materials & Interfaces* **3** 528-33

[244] Monroy E, Omnès F and Calle F 2003 Wide-bandgap semiconductor ultraviolet photodetectors *Semiconductor Science and Technology* **18** R33

[245] Yu X, Zhao Z, Zhang J, Guo W, Qiu J, Li D, Li Z, Mou X, Li L and Li A 2016 Rutile Nanorod/Anatase Nanowire Junction Array as Both Sensor and Power Supplier for High-Performance, Self-Powered, Wireless UV Photodetector *Small* **12** 2759-67

[246] Nunes D, Pimentel A, Araujo A, Calmeiro T, Panigrahi S, Pinto J, Barquinha P, Gama M, Fortunato E and Martins R Enhanced UV Flexible Photodetectors and Photocatalysts Based on TiO 2 Nanoplatforms *Topics in Catalysis* 1-16

[247] Zou J, Zhang Q, Huang K and Marzari N 2010 Ultraviolet Photodetectors Based on Anodic TiO2 Nanotube Arrays *The Journal of Physical Chemistry C* **114** 10725-9

[248] Jie X, Huiyun W, Er-Jia G and Fang Y 2011 Highly sensitive fast-response UV photodetectors based on epitaxial TiO 2 films *Journal of Physics D: Applied Physics* **44** 375104

[249] Yanru X, Lin W, Qinghao L, Yanxue C, Shishen Y, Jun J, Guolei L and Liangmo M 2014 High-performance self-powered UV photodetectors based on TiO 2 nano-branched arrays *Nanotechnology* **25** 075202

[250] Zu X, Wang H, Yi G, Zhang Z, Jiang X, Gong J and Luo H 2015 Self-powered UV photodetector based on heterostructured TiO2 nanowire arrays and polyaniline nanoflower arrays *Synthetic Metals* **200** 58-65

[251] Wang J, Xu G, Zhang X, Lv J, Zhang X, Zheng Z and Wu Y 2015 Electrochemical performance and biosensor application of TiO2 nanotube arrays with mesoporous structures constructed by chemical etching *Dalton Transactions* **44** 7662-72

[252] Noothongkaew S, Han J K, Lee Y B, Thumthan O and An K-S 2017 Au NPs decorated TiO2 nanotubes array candidate for UV photodetectors *Progress in Natural Science: Materials International* **27** 641-6

[253] Chen D, Wei L, Meng L, Wang D, Chen Y, Tian Y, Yan S, Mei L and Jiao J 2018 High-Performance Self-Powered UV Detector Based on SnO2-TiO2 Nanomace Arrays *Nanoscale Research Letters* **13** 92

[254] Viticoli M, Curulli A, Cusma A, Kaciulis S, Nunziante S, Pandolfi L, Valentini F and Padeletti G 2006 Third-generation biosensors based on TiO2 nanostructured films *Materials Science and Engineering: C* **26** 947-51

[255] Hu L, Huo K, Chen R, Gao B, Fu J and Chu P K 2011 Recyclable and High-Sensitivity Electrochemical Biosensing Platform Composed of Carbon-Doped TiO2 Nanotube Arrays *Analytical Chemistry* **83** 8138-44

[256] Hongwei G, Min S, Chao L and Shubai W 2012 Electrochemical DNA Biosensor Based on Graphene and TiO2 Nanorods Composite Film for the Detection of Transgenic Soybean Gene Sequence of MON89788 *Electroanalysis* **24** 2283-90

[257] Jang H D, Kim S K, Chang H, Roh K-M, Choi J-W and Huang J 2012 A glucose biosensor based on TiO2–Graphene composite *Biosensors and Bioelectronics* **38** 184-8

[258] Romero-Arcos M, Garnica-Romo M G, Martinez-Flores H E, Vázquez-Marrufo G, Ramírez-Bon R, González-Hernández J and Barbosa-Cánovas G V 2016 Enzyme Immobilization by Amperometric Biosensors with TiO2 Nanoparticles Used to Detect Phenol Compounds *Food Engineering Reviews* **8** 235-50

[259] Coronado J M, Fresno F, Hernández-Alonso M D and Portela R 2013 *Design of Advanced Photocatalytic Materials for Energy and Environmental Applications*: Springer London)

[260] Ramana C V, Utsunomiya S, Ewing R C, Julien C M and Becker U 2006 Structural Stability and Phase Transitions in WO3 Thin Films *The Journal of Physical Chemistry B* **110** 10430-5

[261] Wang L, Huang M, Chen Z, Yang Z, Qiu M, Wang K and Zhang W 2016 pH-controlled assembly of three-dimensional tungsten oxide hierarchical nanostructures for catalytic oxidation of cyclohexene to adipic acid *CrystEngComm* **18** 8688-95

[262] Marques A C, Santos L, Costa M N, Dantas J M, Duarte P, Gonçalves A, Martins R, Salgueiro C A and Fortunato E 2015 Office Paper Platform for Bioelectrochromic Detection of Electrochemically Active Bacteria using Tungsten Trioxide Nanoprobes *Scientific Reports* **5** 9910

[263] Li P, Li X, Zhao Z, Wang M, Fox T, Zhang Q and Zhou Y 2016 Correlations among structure, composition and electrochemical performances of WO3 anode materials for lithium ion batteries *Electrochimica Acta* **192** 148-57

[264] Yang J, Li W, Li J, Sun D and Chen Q 2012 Hydrothermal synthesis and photoelectrochemical properties of vertically aligned tungsten trioxide (hydrate) plate-like arrays fabricated directly on FTO substrates *Journal of Materials Chemistry* **22** 17744-52

[265] Fang Z, Jiao S, Wang B, Yin W, Liu S, Gao R, Liu Z, Pang G and Feng S 2017 Synthesis of reduced cubic phase WO3−x nanosheet by direct reduction of H2WO4·H2O *Materials Today Energy* **6** 146-53

[266] Pokhrel S, Birkenstock J, Dianat A, Zimmermann J, Schowalter M, Rosenauer A, Ciacchi L C and Madler L 2015 In situ high temperature X-ray diffraction, transmission electron microscopy and theoretical modeling for the formation of WO3 crystallites *CrystEngComm* **17** 6985-98

[267] Vogt T, Woodward P M and Hunter B A 1999 The High-Temperature Phases of WO3 *Journal of Solid State Chemistry* **144** 209-15

[268] Solonin Y M, Khyzhun O Y and Graivoronskaya E A 2001 Nonstoichiometric Tungsten Oxide Based on Hexagonal WO3 *Crystal Growth & Design* **1** 473-7

[269] Sungpanich J, Thongtem T and Thongtem S 2014 Photocatalysis of WO3 Nanoplates Synthesized by Conventional-Hydrothermal and Microwave-Hydrothermal Methods and of Commercial WO3 Nanorods *Journal of Nanomaterials* **2014** 8

[270] Luo J Y, Gong L, Tan H D, Deng S Z, Xu N S, Zeng Q G and Wang Y 2012 Study of the catalyst poisoning and reactivation of Pt nanoparticles on the surface of WO3 nanowire in gasochromic coloration *Sensors and Actuators B: Chemical* **171-172** 1117-24

[271] Yu Y, Zeng W and Zhang H 2016 Hydrothermal synthesis of assembled WO3·H2O nanoflowers with enhanced gas sensing performance *Materials Letters* **171** 162-5

[272] Tong H, Xu Y, Cheng X, Zhang X, Gao S, Zhao H and Huo L 2016 One-pot solvothermal synthesis of hierarchical WO3 hollow microspheres with superior lithium ion battery anode performance *Electrochimica Acta* **210** 147-54

[273] Vasudevan V, Thangavel S, Nallamuthu G, Kirubakaran K, Ramasubramanian P A and Venugopal G 2018 Enhanced Photocatalytic Properties of Nanostructured WO3 Semiconductor-Photocatalyst Prepared via Hydrothermal Method *Journal of Nanoscience and Nanotechnology* **18** 3320-8

[274] Nayak A K and Pradhan D 2018 Microwave-Assisted Greener Synthesis of Defect-Rich Tungsten Oxide Nanowires with Enhanced Photocatalytic and

Photoelectrochemical Performance *The Journal of Physical Chemistry C* **122** 3183-93

[275] Seung-Myung R and Chunghee N Adsorption Characteristics of Methylene Blue on WO3 Nanorods Prepared by Microwave-Assisted Hydrothermal Methods *physica status solidi (a)* **0** 1700996

[276] Yun G, Arunachalam M, Kim H-S, Ahn K-S and Kang S H 2018 Role of WO3 Layers Electrodeposited on SnO2 Inverse Opal Skeletons in Photoelectrochemical Water Splitting *The Journal of Physical Chemistry C* **122** 9729-

[277] Raudoniene J, Laurikenas A, Kaba M M, Sahin G, Morkan A U, Brazinskiene D, Asadauskas S, Seidu R, Kareiva A and Garskaite E 2018 Textured WO3 and WO3:Mo films deposited from chemical solution on stainless steel *Thin Solid Films* **653** 179-87

[278] Cai Z, Liu B, Zou X and Cheng H-M 2018 Chemical Vapor Deposition Growth and Applications of Two-Dimensional Materials and Their Heterostructures *Chemical Reviews*

[279] Zhang J, Lu H, Yan C, Yang Z, Zhu G, Gao J, Yin F and Wang C 2018 Fabrication of conductive graphene oxide-WO3 composite nanofibers by electrospinning and their enhanced acetone gas sensing properties *Sensors and Actuators B: Chemical* **264** 128-38

[280] Kai S, Fengmei G, Weiyou Y, Enyan W, Zhenxia W and Huilin H 2018 WO3 Mesoporous Nanobelts towards Efficient Photoelectrocatalysts for Water Splitting *ChemElectroChem* **5** 322-7

[281] Deliang C, Xianxiang H, Hejing W, Yu W, Hailong W, Xinjian L, Rui Z, Hongxia L, Hongliang X, Shaokang G, Jing S and Lian G 2010 The enhanced alcohol-sensing response of ultrathin WO 3 nanoplates *Nanotechnology* **21** 035501

[282] Xu M, Zeng W, Yang F and Chen L 2015 Controllability of assemblage from WO3·H2O nanoplates to nanoflowers with the assistance of oxalic acid *Journal of Materials Science: Materials in Electronics* **26** 6676-82

[283] Kunquan H, Maohai X and Huasheng W 2006 Tungsten oxide nanowires synthesized by a catalyst-free method at low temperature *Nanotechnology* **17** 4830

[284] Huanjun C, Ningsheng X, Shaozhi D, Dongyu L, Zhenglin L, Jun Z and Jun C 2007 Gasochromic effect and relative mechanism of WO 3 nanowire films *Nanotechnology* **18** 205701

[285] Jerry Y, Liu Y, Hao W, Mahnaz S, Matthew Richard F, Jia L, Jin Y, Zhi Fu L, Wojtek W, Nunzio M, Yong Xiang L, Gengmin Z, Kourosh K-z and Peter To L 2013 Hydrothermally formed functional niobium oxide doped tungsten nanorods *Nanotechnology* **24** 495501

[286] Chih-Hao L, Min Hsiung H, Chi-Yun K and Ing-Chi L 2014 Preparation of WO 3 nanorods by a hydrothermal method for electrochromic device *Japanese Journal of Applied Physics* **53** 06JG8

[287] Hu W, Zhao Y, Liu Z, Dunnill C W, Gregory D H and Zhu Y 2008 Nanostructural Evolution: From One-Dimensional Tungsten Oxide Nanowires to Three-Dimensional Ferberite Flowers *Chemistry of Materials* **20** 5657-65

[288] Wang C, Feng C, Wang M, Li X, Cheng P, Zhang H, Sun Y, Sun P and Lu G 2015 One-pot synthesis of hierarchical WO3 hollow nanospheres and their gas sensing properties *RSC Advances* **5** 29698-703

[289] Li Y, McMaster W A, Wei H, Chen D and Caruso R A 2018 Enhanced Electrochromic Properties of WO3 Nanotree-like Structures Synthesized via a Two-Step Solvothermal Process Showing Promise for Electrochromic Window Application *ACS Applied Nano Materials*

[290] He X, Li X, Bi Z, Chen Y, Xu X and Gao X 2018 Dual-functional electrochromic and energy-storage electrodes based on tungsten trioxide nanostructures *Journal of Solid State Electrochemistry*

[291] Shen L, Luo G, Zheng J and Xu C 2018 Effect of pH on the electrochromic and photoluminescent properties of Eu doped WO3 film *Electrochimica Acta* **278** 263-70

[292] Lee-Sie E A, Ming T A W, Xing C, Shlomo M and See L P 2018 Recent Advances in Flexible Electrochromic Devices: Prerequisites, Challenges, and Prospects *Energy Technology* **6** 33-45

[293] Wojcik P J, Santos L, Pereira L, Martins R and Fortunato E 2015 Tailoring nanoscale properties of tungsten oxide for inkjet printed electrochromic devices *Nanoscale* **7** 1696-708

[294] Wojcik P J, Cruz A S, Santos L, Pereira L, Martins R and Fortunato E 2012 Microstructure control of dual-phase inkjet-printed a-WO3/TiO2/WOX films for high-performance electrochromic applications *Journal of Materials Chemistry* **22** 13268-78

[295] Pedro B, Sónia P, Luís P, Pawel W, Paul G, Rodrigo M and Elvira F 2015 Flexible and Transparent WO3 Transistor with Electrical and Optical Modulation *Advanced Electronic Materials* **1** 1500030

[296] Zhang J, Fu X, Hao H and Gan W 2018 Facile synthesis 3D flower-like Ag@WO3 nanostructures and applications in solar-light photocatalysis *Journal of Alloys and Compounds* **757** 134-41

[297] Sajjad A K L, Sajjad S, Iqbal A and Ryma N-u-A 2018 ZnO/WO3 nanostructure as an efficient visible light catalyst *Ceramics International* **44** 9364-71

[298] Poongodi S, Kumar P S, Mangalaraj D, Ponpandian N, Meena P, Masuda Y and Lee C 2017 Electrodeposition of WO3 nanostructured thin films for electrochromic and H2S gas sensor applications *Journal of Alloys and Compounds* **719** 71-81

[299] Ponnusamy R, Gangan A, Chakraborty B and Rout C S 2018 Tuning the pure monoclinic phase of WO3 and WO3-Ag nanostructures for non-enzymatic glucose sensing application with theoretical insight from electronic structure simulations *Journal of Applied Physics* **123** 024701

[300] Ponnusamy R, Chakraborty B and Rout C S 2018 Pd-Doped WO3 Nanostructures as Potential Glucose Sensor with Insight from Electronic Structure Simulations *The Journal of Physical Chemistry B* **122** 2737-46

[301] Sone B T, Nkosi S S, Nkosi M M, Coetsee-Hugo E, Swart H C and Maaza M 2018 Self-assembled micro-/nanostructured WO3 thin films by aqueous chemical growth and their applications in H2 and CO2 sensing *AIP Conference Proceedings* **1962** 040003

[302] Wang C, Sun R, Li X, Sun Y, Sun P, Liu F and Lu G 2014 Hierarchical flower-like WO3 nanostructures and their gas sensing properties *Sensors and Actuators B: Chemical* **204** 224-30

[303] Kida T, Nishiyama A, Yuasa M, Shimanoe K and Yamazoe N 2009 Highly sensitive NO2 sensors using lamellar-structured WO3 particles prepared by an acidification method *Sensors and Actuators B: Chemical* **135** 568-74

[304] Wang S-H, Chou T-C and Liu C-C 2003 Nano-crystalline tungsten oxide NO2 sensor *Sensors and Actuators B: Chemical* **94** 343-51

[305] Wang C, Li X, Feng C, Sun Y and Lu G 2015 Nanosheets assembled hierarchical flower-like WO3 nanostructures: Synthesis, characterization, and their gas sensing properties *Sensors and Actuators B: Chemical* **210** 75-81

[306] An S, Park S, Ko H and Lee C 2014 Fabrication of WO3 nanotube sensors and their gas sensing properties *Ceramics International* **40** 1423-9

[307] Hieu N V, Quang V V, Hoa N D and Kim D 2011 Preparing large-scale WO3 nanowire-like structure for high sensitivity NH3 gas sensor through a simple route *Current Applied Physics* **11** 657-61

[308] Zhang H, Liu Z, Yang J, Guo W, Zhu L and Zheng W 2014 Temperature and acidity effects on WO3 nanostructures and gas-sensing properties of WO3 nanoplates *Materials Research Bulletin* **57** 260-7

[309] Boudiba A, Zhang C, Bittencourt C, Umek P, Olivier M-G, Snyders R and Debliquy M 2012 SO2 Gas Sensors based on WO3 Nanostructures with Different Morphologies *Procedia Engineering* **47** 1033-6

[310] Ionescu R, Hoel A, Granqvist C G, Llobet E and Heszler P 2005 Low-level detection of ethanol and H2S with temperature-modulated WO3 nanoparticle gas sensors *Sensors and Actuators B: Chemical* **104** 132-9

[311] Xiang Q, Meng G F, Zhao H B, Zhang Y, Li H, Ma W J and Xu J Q 2010 Au Nanoparticle Modified WO3 Nanorods with Their Enhanced Properties for

Photocatalysis and Gas Sensing *The Journal of Physical Chemistry C* **114** 2049-55

[312] Liu X, Zhang J, Yang T, Guo X, Wu S and Wang S 2011 Synthesis of Pt nanoparticles functionalized WO3 nanorods and their gas sensing properties *Sensors and Actuators B: Chemical* **156** 918-23

[313] Li F, Ruan S, Zhang N, Yin Y, Guo S, Chen Y, Zhang H and Li C 2018 Synthesis and characterization of Cr-doped WO3 nanofibers for conductometric sensors with high xylene sensitivity *Sensors and Actuators B: Chemical* **265** 355-64

[314] Chen L and Tsang S C 2003 Ag doped WO3-based powder sensor for the detection of NO gas in air *Sensors and Actuators B: Chemical* **89** 68-75

[315] Qi J, Chen K, Xing Y, Fan H, Zhao H, Yang J, Li L, Yan B, Zhou J, Guo L and Yang S 2018 Application of 3D hierarchical monoclinic-type structural Sb-doped WO3 towards NO2 gas detection at low temperature *Nanoscale* **10** 7440-50

[316] Yu W, Sun Y, Zhang T, Zhang K, Wang S, Chen X and Dai N 2015 CuO/WO3 Hybrid Nanocubes for High-Responsivity and Fast-Recovery H2S Sensors Operated at Low Temperature *Particle & Particle Systems Characterization* **33** 15-20

[317] Chaudhari G N, Bende A M, Bodade A B, Patil S S and Sapkal V S 2006 Structural and gas sensing properties of nanocrystalline TiO2:WO3-based hydrogen sensors *Sensors and Actuators B: Chemical* **115** 297-302

[318] Kumar A, Sanger A, Kumar A and Chandra R 2017 Porous silicon filled with Pd/WO3-ZnO composite thin film for enhanced H2 gas-sensing performance *RSC Advances* **7** 39666-75

[319] Bai S, Li D, Han D, Luo R, Chen A and Chung C L 2010 Preparation, characterization of WO3–SnO2 nanocomposites and their sensing properties for NO2 *Sensors and Actuators B: Chemical* **150** 749-55

[320] An X, Yu J C, Wang Y, Hu Y, Yu X and Zhang G 2012 WO3 nanorods/graphene nanocomposites for high-efficiency visible-light-driven photocatalysis and NO2 gas sensing *Journal of Materials Chemistry* **22** 8525-31

[321] Esfandiar A, Irajizad A, Akhavan O, Ghasemi S and Gholami M R 2014 Pd–WO3/reduced graphene oxide hierarchical nanostructures as efficient hydrogen gas sensors *International Journal of Hydrogen Energy* **39** 8169-79

[322] Ling M and Leach C 2004 *The Effect of Relative Humidity on the NO2 Sensitivity of a SnO2/WO3 Heterojunction Gas Sensor* vol 102

[323] Piloto C, Shafiei M, Khan H, Gupta B, Tesfamichael T and Motta N 2018 Sensing performance of reduced graphene oxide-Fe doped WO3 hybrids to NO2 and humidity at room temperature *Applied Surface Science* **434** 126-33

[324] Wang Z, Fan X, Li C, Men G, Han D and Gu F 2018 Humidity-Sensing Performance of 3DOM WO3 with Controllable Structural Modification *ACS Applied Materials & Interfaces* **10** 3776-83

[325] Ramkumar S and Rajarajan G 2017 A comparative study of humidity sensing and photocatalytic applications of pure and nickel (Ni)-doped WO3 thin films *Applied Physics A* **123** 401

[326] Zou Z, Qiu Y, Xu J, Guo P and Luo Y 2017 High performance photoelectric responses of nanocrystalline WO3 film to humidity irradiated by UV light *Journal of Materials Science: Materials in Electronics* **28** 15618-24

[327] Dong Y F, Li L Y, Jiang W F, Wang H Y and Li X J 2009 Capacitive humidity-sensing properties of electron-beam-evaporated nanophased WO3 film on silicon

nanoporous pillar array *Physica E: Low-dimensional Systems and Nanostructures* **41** 711-4

[328] Patil D, Seo Y-K, Hwang Y K, Chang J-S and Patil P 2008 Humidity sensitive poly(2,5-dimethoxyaniline)/WO3 composites *Sensors and Actuators B: Chemical* **132** 116-24

[329] Shakya V and Kumar Pandey N 2018 Structural and Moisture Sensing Properties of WO3-ZnO Nanocomposites Synthesized by a Soft Chemical Route *Materials Today: Proceedings* **5** 9082-8

[330] Dali S, Mingpeng Y, Jie L and Shayla S 2013 An ultraviolet photodetector fabricated from WO 3 nanodiscs/reduced graphene oxide composite material *Nanotechnology* **24** 295701

[331] Liu J, Zhong M, Li J, Pan A and Zhu X 2015 Few-layer WO3 nanosheets for high-performance UV-photodetectors *Materials Letters* **148** 184-7

[332] Li L, Zhang Y, Fang X, Zhai T, Liao M, Sun X, Koide Y, Bando Y and Golberg D 2011 WO3 nanowires on carbon papers: electronic transport, improved ultraviolet-light photodetectors and excellent field emitters *Journal of Materials Chemistry* **21** 6525-30

[333] Huang K, Zhang Q, Yang F and He D 2010 Ultraviolet photoconductance of a single hexagonal WO3 nanowire *Nano Research* **3** 281-7

[334] He Z, Liu Q, Hou H, Gao F, Tang B and Yang W 2015 Tailored Electrospinning of WO3 Nanobelts as Efficient Ultraviolet Photodetectors with Photo-Dark Current Ratios up to 1000 *ACS Applied Materials & Interfaces* **7** 10878-85

[335] Shao D, Yu M, Lian J and Sawyer S 2014 Optoelectronic properties of three dimensional WO3 nanoshale and its application for UV sensing *Optical Materials* **36** 1002-5

[336] Cook B, Liu Q, Butler J, Smith K, Shi K, Ewing D, Casper M, Stramel A, Elliot A and Wu J 2018 Heat-Assisted Inkjet Printing of Tungsten Oxide for High-Performance Ultraviolet Photodetectors *ACS Applied Materials & Interfaces* **10** 873-9

[337] Hai Z, Akbari M K, Xue C, Xu H, Hyde L and Zhuiykov S 2017 Wafer-scaled monolayer WO3 windows ultra-sensitive, extremely-fast and stable UV-A photodetection *Applied Surface Science* **405** 169-77

[338] Santos L, Silveira C M, Elangovan E, Neto J P, Nunes D, Pereira L, Martins R, Viegas J, Moura J J G, Todorovic S, Almeida M G and Fortunato E 2016 Synthesis of WO3 nanoparticles for biosensing applications *Sensors and Actuators B: Chemical* **223** 186-94

[339] Deng Z, Gong Y, Luo Y and Tian Y 2009 WO3 nanostructures facilitate electron transfer of enzyme: Application to detection of H2O2 with high selectivity *Biosensors and Bioelectronics* **24** 2465-9

[340] Liu H, Duan C, Yang C, Chen X, Shen W and Zhu Z 2015 A novel nitrite biosensor based on the direct electron transfer hemoglobin immobilized in the WO3 nanowires with high length–diameter ratio *Materials Science and Engineering: C* **53** 43-9

[341] Anithaa A C, Lavanya N, Asokan K and Sekar C 2015 WO3 nanoparticles based direct electrochemical dopamine sensor in the presence of ascorbic acid *Electrochimica Acta* **167** 294-302

[342] Hariharan V, Radhakrishnan S, Parthibavarman M, Dhilipkumar R and Sekar C 2011 Synthesis of polyethylene glycol (PEG) assisted tungsten oxide (WO3) nanoparticles for l-dopa bio-sensing applications *Talanta* **85** 2166-74

[343] Ghodsi J, Rafati A A and Shoja Y 2016 First report on hemoglobin electrostatic immobilization on WO 3 nanoparticles: application in the simultaneous determination of levodopa, uric acid, and folic acid *Analytical and bioanalytical chemistry* **408** 3899-909

[344] Righettoni M, Tricoli A and Pratsinis S E 2010 Si:WO3 Sensors for Highly Selective Detection of Acetone for Easy Diagnosis of Diabetes by Breath Analysis *Analytical Chemistry* **82** 3581-7

[345] Ma Y, Zhao M, Cai B, Wang W, Ye Z and Huang J 2014 3D graphene network@WO3 nanowire composites: a multifunctional colorimetric and electrochemical biosensing platform *Chemical Communications* **50** 11135-8

[346] Li Y, Hsu P-C and Chen S-M 2012 Multi-functionalized biosensor at WO3–TiO2 modified electrode for photoelectrocatalysis of norepinephrine and riboflavin *Sensors and Actuators B: Chemical* **174** 427-35

[347] Sun B, Zhang K, Chen L, Guo L and Ai S 2013 A novel photoelectrochemical sensor based on PPIX-functionalized WO3–rGO nanohybrid-decorated ITO electrode for detecting cysteine *Biosensors and Bioelectronics* **44** 48-51

[348] Santos L, Neto J P, Crespo A, Nunes D, Costa N, Fonseca I M, Barquinha P, Pereira L, Silva J, Martins R and Fortunato E 2014 WO3 Nanoparticle-Based Conformable pH Sensor *ACS Applied Materials & Interfaces* **6** 12226-34

[349] Nunes D, Santos L, Duarte P, Pimentel A, Pinto J V, Barquinha P, Carvalho P A, Fortunato E and Martins R 2014 Room Temperature Synthesis of Cu2O Nanospheres: Optical Properties and Thermal Behavior *Microscopy and Microanalysis* **21** 108-19

[350] K. M B, A. P, D. R, M. B, P. H, J. K P, Th. S, C. R, J. B, M. E, C. H, M. H, J. B, A. K, S. S, C. M and C. R 2012 Binary copper oxide semiconductors: From materials towards devices *physica status solidi (b)* **249** 1487-509

[351] Ng C H B and Fan W Y 2006 Shape Evolution of Cu2O Nanostructures via Kinetic and Thermodynamic Controlled Growth *The Journal of Physical Chemistry B* **110** 20801-7

[352] Heinemann M, Eifert B and Heiliger C 2013 Band structure and phase stability of the copper oxides Cu${}_{2}$O, CuO, and Cu${}_{4}$O${}_{3}$ *Physical Review B* **87** 115111

[353] Dhineshbabu N R, Rajendran V, Nithyavathy N and Vetumperumal R 2016 Study of structural and optical properties of cupric oxide nanoparticles *Applied Nanoscience* **6** 933-9

[354] Wang Y, Lany S, Ghanbaja J, Fagot-Revurat Y, Chen Y P, Soldera F, Horwat D, Mücklich F and Pierson J F 2016 Electronic structures of $\mathrm{C}{\mathrm{u}}_{2}\mathrm{O},\mathrm{C}{\mathrm{u}}_{4}{\mathrm{O}}_{3}$, and CuO: A joint experimental and theoretical study *Physical Review B* **94** 245418

[355] Barquinha P, Martins R, Pereira L and Fortunato E 2012 *Transparent Oxide Electronics: From Materials to Devices*: Wiley)

[356] Nolan M and Elliott S D 2006 The p-type conduction mechanism in Cu2O: a first principles study *Physical Chemistry Chemical Physics* **8** 5350-8

[357] Murali D S, Kumar S, Choudhary R J, Wadikar A D, Jain M K and Subrahmanyam A 2015 Synthesis of Cu2O from CuO thin films: Optical and electrical properties *AIP Advances* **5** 047143

[358] Chatterjee S and Pal A J 2016 Introducing Cu2O Thin Films as a Hole-Transport Layer in Efficient Planar Perovskite Solar Cell Structures *The Journal of Physical Chemistry C* **120** 1428-37

[359] Korzhavyi P A and Johansson B 2011 *Literature review on the properties of cuprous oxide Cu2O and the process of copper oxidation*: Swedish Nuclear Fuel and Waste Management Company)

[360] Cupric oxide (CuO) crystal structure, lattice parameters: Datasheet from Landolt-Börnstein - Group III Condensed Matter · Volume 41C: "Non-Tetrahedrally Bonded Elements and Binary Compounds I" in SpringerMaterials (https://dx.doi.org/10.1007/10681727_51). Springer-Verlag Berlin Heidelberg)

[361] Su D, Xie X, Dou S and Wang G 2014 CuO single crystal with exposed {001} facets - A highly efficient material for gas sensing and Li-ion battery applications *Scientific Reports* **4** 5753

[362] Döring G, Sternemann C, Kaprolat A, Mattila A, Hämäläinen K and Schülke W 2004 *Shake-up valence excitations in CuO by resonant inelastic x-ray scattering* vol 70

[363] Kuz'menko A, Van der Marel D, Van Bentum P, Tishchenko E, Presura C and Bush A 2001 Infrared spectroscopic study of CuO: Signatures of strong spin-phonon interaction and structural distortion *Physical Review B* **63** 094303

[364] Gattinoni C and Michaelides A 2015 Atomistic details of oxide surfaces and surface oxidation: the example of copper and its oxides *Surface Science Reports* **70** 424-47

[365] Kevin M, Ong W L, Lee G H and Ho G W 2011 Formation of hybrid structures: copper oxide nanocrystals templated on ultralong copper nanowires for open network sensing at room temperature *Nanotechnology* **22** 235701

[366] Jiang X, Herricks T and Xia Y 2002 CuO Nanowires Can Be Synthesized by Heating Copper Substrates in Air *Nano Letters* **2** 1333-8

[367] Karapetyan A, Reymers A, Giorgio S, Fauquet C, Sajti L, Nitsche S, Nersesyan M, Gevorgyan V and Marine W 2015 Cuprous oxide thin films prepared by thermal oxidation of copper layer. Morphological and optical properties *Journal of Luminescence* **159** 325-32

[368] Figueiredo V, Pinto J V, Deuermeier J, Barros R, Alves E, Martins R and Fortunato E 2013 p-Type <formula formulatype="inline"> <img src="/images/tex/20030.gif" alt="{\hbox {Cu}}_{x}{\hbox {O}}"> </formula> Thin-Film Transistors Produced by Thermal Oxidation *Display Technology, Journal of* **9** 735-40

[369] Figueiredo V, Elangovan E, Gonçalves G, Franco N, Alves E, Park S H K, Martins R and Fortunato E 2009 Electrical, structural and optical characterization of copper oxide thin films as a function of post annealing temperature *physica status solidi (a)* **206** 2143-8

[370] Figueiredo V, Elangovan E, Gonçalves G, Barquinha P, Pereira L, Franco N, Alves E, Martins R and Fortunato E 2008 Effect of post-annealing on the properties of copper oxide thin films obtained from the oxidation of evaporated metallic copper *Applied Surface Science* **254** 3949-54

[371] Nunes D, Calmeiro T R, Nandy S, Pinto J V, Pimentel A, Barquinha P, Carvalho P A, Walmsley J C, Fortunato E and Martins R 2016 Charging effects and surface potential variations of Cu-based nanowires *Thin Solid Films* **601** 45-53

[372] Korshunov A V and Il'in A P 2009 Oxidation of copper nanopowders on heating in air *Russian Journal of Applied Chemistry* **82** 1164-71

[373] Singh R, Science E S D and Division T 2000 *Low and High Dielectric Constant Materials: Materials Science, Processing, and Reliability Issues : Proceedings of the Fourth International Symposium : And, Thin Film Materials for Advanced Packaging Technologies : Proceedings of the Second International Symposium*: Electrochemical Society)

[374] Choopun S, Hongsith N and Wongrat E 2010 Metal-oxide nanowires by thermal oxidation reaction technique

INTECH

[375] Li Y, Liang J, Tao Z and Chen J 2008 CuO particles and plates: Synthesis and gas-sensor application *Materials Research Bulletin* **43** 2380-5

[376] Luévano-Hipólito E, Torres-Martínez L M, Sánchez-Martínez D and Alfaro Cruz M R 2017 Cu2O precipitation-assisted with ultrasound and microwave radiation for photocatalytic hydrogen production *International Journal of Hydrogen Energy* **42** 12997-3010

[377] Lim Y-F, Chua C S, Lee C J J and Chi D 2014 Sol-gel deposited Cu2O and CuO thin films for photocatalytic water splitting *Physical Chemistry Chemical Physics* **16** 25928-34

[378] Mallick P 2014 *Synthesis of Copper Oxide Nanocomposite (Cu2O/CuO) by Sol–gel Route* vol 84

[379] Panigrahi S, Nunes D, Calmeiro T, Kardarian K, Martins R and Fortunato E 2017 Oxide-Based Solar Cell: Impact of Layer Thicknesses on the Device Performance *ACS combinatorial science* **19** 113-20

[380] Hossain M A, Al-Gaashani R, Hamoudi H, Al Marri M J, Hussein I A, Belaidi A, Merzougui B A, Alharbi F H and Tabet N 2017 Controlled growth of Cu2O thin

films by electrodeposition approach *Materials Science in Semiconductor Processing* **63** 203-11

[381] Brandt I S, Tumelero M A, Pelegrini S, Zangari G and Pasa A A 2017 Electrodeposition of Cu2O: growth, properties, and applications *Journal of Solid State Electrochemistry* **21** 1999-2020

[382] Dolai S, Dey R, Das S, Hussain S, Bhar R and Pal A K 2017 Cupric oxide (CuO) thin films prepared by reactive d.c. magnetron sputtering technique for photovoltaic application *Journal of Alloys and Compounds* **724** 456-64

[383] Zhu H, Zhang J, Li C, Pan F, Wang T and Huang B 2009 Cu2O thin films deposited by reactive direct current magnetron sputtering *Thin Solid Films* **517** 5700-4

[384] Filipič G and Cvelbar U 2012 Copper oxide nanowires: a review of growth *Nanotechnology* **23** 194001

[385] Chen J T, Zhang F, Wang J, Zhang G A, Miao B B, Fan X Y, Yan D and Yan P X 2008 CuO nanowires synthesized by thermal oxidation route *Journal of Alloys and Compounds* **454** 268-73

[386] Kim Y-S, Hwang I-S, Kim S-J, Lee C-Y and Lee J-H 2008 CuO nanowire gas sensors for air quality control in automotive cabin *Sensors and Actuators B: Chemical* **135** 298-303

[387] Wei M and Huo J 2010 Preparation of Cu2O nanorods by a simple solvothermal method *Materials Chemistry and Physics* **121** 291-4

[388] Kumar K and Chowdhury A 2017 Facile synthesis of CuO nanorods obtained without any template and/or surfactant *Ceramics International* **43** 13943-7

[389] Zhang X, Wang G, Liu X and Wu H 2008 Synthesis and electrochemical properties of CuO nanobelts *Materials Chemistry and Physics* **112** 726-9

[390] Dan Z, Yang Y, Qin F, Wang H and Chang H 2018 Facile Fabrication of Cu2O Nanobelts in Ethanol on Nanoporous Cu and Their Photodegradation of Methyl Orange *Materials* **11** 446

[391] Mukherjee N, Show B, Maji S K, Madhu U, Bhar S K, Mitra B C, Khan G G and Mondal A 2011 CuO nano-whiskers: Electrodeposition, Raman analysis, photoluminescence study and photocatalytic activity *Materials Letters* **65** 3248-50

[392] Qu Y, Li X, Chen G, Zhang H and Chen Y 2008 Synthesis of Cu2O nano-whiskers by a novel wet-chemical route *Materials Letters* **62** 886-8

[393] Chang I C, Chen P-C, Tsai M-C, Chen T-T, Yang M-H, Chiu H-T and Lee C-Y 2013 Large-scale synthesis of uniform Cu2O nanocubes with tunable sizes by in-situ nucleation *CrystEngComm* **15** 2363-6

[394] Navale Y H, Navale S T, Galluzzi M, Stadler F J, Debnath A K, Ramgir N S, Gadkari S C, Gupta S K, Aswal D K and Patil V B 2017 Rapid synthesis strategy of CuO nanocubes for sensitive and selective detection of NO2 *Journal of Alloys and Compounds* **708** 456-63

[395] Cao Y, Fan J, Bai L, Yuan F and Chen Y 2009 Morphology Evolution of Cu2O from Octahedra to Hollow Structures *Crystal Growth & Design* **10** 232-6

[396] Feng L, Xuan Z, Bai Y, Zhao H, Li L, Chen Y, Yang X, Su C, Guo J and Chen X 2014 Preparation of octahedral CuO micro/nanocrystals and electrochemical performance as anode for lithium-ion battery *Journal of Alloys and Compounds* **600** 162-7

[397] Sun S, Zhang X, Song X, Liang S, Wang L and Yang Z 2012 Bottom-up assembly of hierarchical Cu2O nanospheres: controllable synthesis, formation mechanism and enhanced photochemical activities *CrystEngComm* **14** 3545-53

[398] Chen W, Li L, Peng Q and Li Y 2012 Polyol synthesis and chemical conversion of Cu2O nanospheres *Nano Res.* **5** 320-6

[399] Jiang L, You T, Yin P, Shang Y, Zhang D, Guo L and Yang S 2013 Surface-enhanced Raman scattering spectra of adsorbates on Cu2O nanospheres: charge-transfer and electromagnetic enhancement *Nanoscale* **5** 2784-9

[400] Zhang J, Liu J, Peng Q, Wang X and Li Y 2006 Nearly Monodisperse Cu2O and CuO Nanospheres: Preparation and Applications for Sensitive Gas Sensors *Chemistry of Materials* **18** 867-71

[401] H. Z, Q. Z, Y. Z, Y. W, L. Z and B. Y 2007 One-Pot Synthesis and Hierarchical Assembly of Hollow Cu2O Microspheres with Nanocrystals-Composed Porous Multishell and Their Gas-Sensing Properties *Advanced Functional Materials* **17** 2766-71

[402] Scuderi V, Amiard G, Boninelli S, Scalese S, Miritello M, Sberna P M, Impellizzeri G and Privitera V 2016 Photocatalytic activity of CuO and Cu2O nanowires *Materials Science in Semiconductor Processing* **42** 89-93

[403] Kumar S, Parlett C M A, Isaacs M A, Jowett D V, Douthwaite R E, Cockett M C R and Lee A F 2016 Facile synthesis of hierarchical Cu2O nanocubes as visible light photocatalysts *Applied Catalysis B: Environmental* **189** 226-32

[404] Rai B P 1988 *Cu2O solar cells: A review* vol 25

[405] Anandan S, Wen X and Yang S 2005 Room temperature growth of CuO nanorod arrays on copper and their application as a cathode in dye-sensitized solar cells *Materials Chemistry and Physics* **93** 35-40

[406] Bijani S, Gabás M, Martínez L, Ramos-Barrado J R, Morales J and Sánchez L 2007 Nanostructured Cu2O thin film electrodes prepared by electrodeposition for rechargeable lithium batteries *Thin Solid Films* **515** 5505-11

[407] Yi-Tao X, Ying G, Hong J, Xiao-Bin X, Bo Z, Peng-Li Z, Xian-Zhu F, Rong S and Ching-Ping W 2015 Enhanced Performance of Lithium-Ion Batteries with Copper Oxide Microspheres @ Graphene Oxide Micro/Nanocomposite Electrodes *Energy Technology* **3** 488-95

[408] Gao P and Liu D 2015 Facile synthesis of copper oxide nanostructures and their application in non-enzymatic hydrogen peroxide sensing *Sensors and Actuators B: Chemical* **208** 346-54

[409] Steinhauer S, Brunet E, Maier T, Mutinati G C, Köck A, Freudenberg O, Gspan C, Grogger W, Neuhold A and Resel R 2013 Gas sensing properties of novel CuO nanowire devices *Sensors and Actuators B: Chemical* **187** 50-7

[410] Zheng X, Ning H, Wenhui L, Yuzhou D, Shuyan G, Ying W, Xiaofeng W, Yingxia L and Yunfa C 2017 Facet-dependent gas sensing properties of Cu2O crystals *physica status solidi (a)* **214** 1600904

[411] Şişman O, Kılınç N and Öztürk Z Z 2015 H2 Sensing Properties of Cu2O Nanowires on Glass Substrate *Procedia Engineering* **120** 1170-4

[412] Tang N, Chen B, Xia Y, Chen D and Jiao X 2015 Facile synthesis of Cu2O nanocages and gas sensing performance towards gasoline *RSC Advances* **5** 54433-8

[413] H. J A, P. S and Guo K 2009 Methane gas sensor application of cuprous oxide synthesized by thermal oxidation *physica status solidi (a)* **206** 332-7

[414] Umar A, Alshahrani A A, Algarni H and Kumar R 2017 CuO nanosheets as potential scaffolds for gas sensing applications *Sensors and Actuators B: Chemical* **250** 24-31

[415] Yang C, Xiao F, Wang J and Su X 2015 3D flower- and 2D sheet-like CuO nanostructures: Microwave-assisted synthesis and application in gas sensors *Sensors and Actuators B: Chemical* **207** 177-85

[416] Taubert A, Stange F, Li Z, Junginger M, Günter C, Neumann M and Friedrich A 2012 CuO Nanoparticles from the Strongly Hydrated Ionic Liquid Precursor (ILP) Tetrabutylammonium Hydroxide: Evaluation of the Ethanol Sensing Activity *ACS Applied Materials & Interfaces* **4** 791-5

[417] Li Z, Wang J, Wang N, Yan S, Liu W, Fu Y Q and Wang Z 2017 Hydrothermal synthesis of hierarchically flower-like CuO nanostructures with porous nanosheets for excellent H2S sensing *Journal of Alloys and Compounds* **725** 1136-43

[418] Hsueh H, Chang S, Hung F, Weng W, Hsu C, Hsueh T, Lin S and Dai B 2011 Ethanol gas sensor of crabwise CuO nanowires prepared on glass substrate *Journal of The Electrochemical Society* **158** J106-J9

[419] Liu X, Zhang J, Kang Y, Wu S and Wang S 2012 Brochantite tabular microspindles and their conversion to wormlike CuO structures for gas sensing *CrystEngComm* **14** 620-5

[420] Choi Y-H, Kim D-H, Han H S, Shin S, Hong S-H and Hong K S 2014 Direct Printing Synthesis of Self-Organized Copper Oxide Hollow Spheres on a Substrate Using Copper(II) Complex Ink: Gas Sensing and Photoelectrochemical Properties *Langmuir* **30** 700-9

[421] Samarasekara P, Kumara N T R N and Yapa N U S 2006 Sputtered copper oxide (CuO) thin films for gas sensor devices *Journal of Physics: Condensed Matter* **18** 2417

[422] Zhang Y-B, Yin J, Li L, Zhang L-X and Bie L-J 2014 Enhanced ethanol gas-sensing properties of flower-like p-CuO/n-ZnO heterojunction nanorods *Sensors and Actuators B: Chemical* **202** 500-7

[423] Li D, Qin L, Zhao P, Zhang Y, Liu D, Liu F, Kang B, Wang Y, Song H, Zhang T and Lu G 2018 Preparation and gas-sensing performances of ZnO/CuO rough nanotubular arrays for low-working temperature H2S detection *Sensors and Actuators B: Chemical* **254** 834-41

[424] Bhuvaneshwari S, Papachan S and Gopalakrishnan N 2017 Free standing CuO-MnO2 nanocomposite for room temperature ammonia sensing *AIP Conference Proceedings* **1832** 050126

[425] Meng F-N, Di X-P, Dong H-W, Zhang Y, Zhu C-L, Li C and Chen Y-J 2013 Ppb H2S gas sensing characteristics of Cu2O/CuO sub-microspheres at low-temperature *Sensors and Actuators B: Chemical* **182** 197-204

[426] Zhou L-J, Zou Y-C, Zhao J, Wang P-P, Feng L-L, Sun L-W, Wang D-J and Li G-D 2013 Facile synthesis of highly stable and porous Cu2O/CuO cubes with enhanced gas sensing properties *Sensors and Actuators B: Chemical* **188** 533-9

[427] Liu Q, Cui Z, Zhang Q and Guo L 2014 Gold-catalytic green synthesis of Cu2O/Au/CuO hierarchical nanostructure and application for CO gas sensor *Chinese Science Bulletin* **59** 7-10

[428] Zhang D, Yin N, Jiang C and Xia B 2017 Characterization of CuO–reduced graphene oxide sandwiched nanostructure and its hydrogen sensing characteristics *Journal of Materials Science: Materials in Electronics* **28** 2763-8

[429] Deng S, Tjoa V, Fan H M, Tan H R, Sayle D C, Olivo M, Mhaisalkar S, Wei J and Sow C H 2012 Reduced Graphene Oxide Conjugated Cu2O Nanowire

Mesocrystals for High-Performance NO2 Gas Sensor *Journal of the American Chemical Society* **134** 4905-17

[430] Hsueh H T, Hsueh T J, Chang S J, Hung F Y, Tsai T Y, Weng W Y, Hsu C L and Dai B T 2011 CuO nanowire-based humidity sensors prepared on glass substrate *Sensors and Actuators B: Chemical* **156** 906-11

[431] Dhonge B P, Ray S S and Mwakikunga B 2017 Electronic to protonic conduction switching in Cu2O nanostructured porous films: the effect of humidity exposure *RSC Advances* **7** 21703-12

[432] Wang S B, Hsiao C H, Chang S J, Lam K T, Wen K H, Young S J, Hung S C and Huang B R 2012 CuO Nanowire-Based Humidity Sensor *IEEE Sensors Journal* **12** 1884-8

[433] Kh S K, Saleem M, Karieva Z M, Mateen A, Chani M T S and Zafar Q 2012 Humidity sensing properties of Cu 2 O-PEPC nanocomposite films *Journal of Semiconductors* **33** 073001

[434] Necmi S, Tülay S and Basri Ü 2000 The effect of humidity on electronic conductivity of an Au/CuO/Cu 2 O/Cu sandwich structure *Semiconductor Science and Technology* **15** 112

[435] Conghui Y, Yiting X, Yuanming D, Nina J, Ning H and Lizong D 2010 CuO based inorganic–organic hybrid nanowires: a new type of highly sensitive humidity sensor *Nanotechnology* **21** 415501

[436] Wang Z, Xiao Y, Cui X, Cheng P, Wang B, Gao Y, Li X, Yang T, Zhang T and Lu G 2014 Humidity-Sensing Properties of Urchinlike CuO Nanostructures Modified by Reduced Graphene Oxide *ACS Applied Materials & Interfaces* **6** 3888-95

[437] Pandey N, Tiwari K and Roy A 2011 Moisture Sensing Application of ${\rm Cu} _ {2}{\rm O} $ Doped ZnO Nanocomposites *IEEE Sensors Journal* **11** 2142-8

[438] Wang X and Cho H J 2018 p-CuO nanowire/n-ZnO nanosheet heterojunction-based near-UV sensor fabricated by electroplating and thermal oxidation process *Materials Letters* **223** 170-3

[439] Hong Q, Cao Y, Xu J, Lu H, He J and Sun J-L 2014 Self-Powered Ultrafast Broadband Photodetector Based on p–n Heterojunctions of CuO/Si Nanowire Array *ACS Applied Materials & Interfaces* **6** 20887-94

[440] Wang S-B, Hsiao C-H, Chang S-J, Jiao Z, Young S-J, Hung S-C and Huang B-R 2013 ZnO branched nanowires and the p-CuO/n-ZnO heterojunction nanostructured photodetector *IEEE transactions on nanotechnology* **12** 263-9

[441] Ok Y H, Lee K R, Jung B O, Kwon Y H and Cho H K 2014 All oxide ultraviolet photodetectors based on a p-Cu2O film/n-ZnO heterostructure nanowires *Thin Solid Films* **570** 282-7

[442] Liu M, Liu R and Chen W 2013 Graphene wrapped Cu2O nanocubes: Non-enzymatic electrochemical sensors for the detection of glucose and hydrogen peroxide with enhanced stability *Biosensors and Bioelectronics* **45** 206-12

[443] Ahmad R, Tripathy N, Ahn M-S, Bhat K S, Mahmoudi T, Wang Y, Yoo J-Y, Kwon D-W, Yang H-Y and Hahn Y-B 2017 Highly efficient non-enzymatic glucose sensor based on CuO modified vertically-grown ZnO nanorods on electrode *Scientific Reports* **7** 5715

[444] Khan R, Ahmad R, Rai P, Jang L-W, Yun J-H, Yu Y-T, Hahn Y-B and Lee I-H 2014 Glucose-assisted synthesis of Cu2O shuriken-like nanostructures and their application as nonenzymatic glucose biosensors *Sensors and Actuators B: Chemical* **203** 471-6

[445] Jindal K, Tomar M and Gupta V 2012 CuO thin film based uric acid biosensor with enhanced response characteristics *Biosensors and Bioelectronics* **38** 11-8

[446] Li Y, Wei Y, Shi G, Xian Y and Jin L 2010 Facile Synthesis of Leaf-Like CuO Nanoparticles and Their Application on Glucose Biosensor *Electroanalysis* **23** 497-502

[447] Li Y, Zhong Y, Zhang Y, Weng W and Li S 2015 Carbon quantum dots/octahedral Cu2O nanocomposites for non-enzymatic glucose and hydrogen peroxide amperometric sensor *Sensors and Actuators B: Chemical* **206** 735-43

[448] Xu L, Yang Q, Liu X, Liu J and Sun X 2014 One-dimensional copper oxide nanotube arrays: biosensors for glucose detection *RSC Advances* **4** 1449-55

[449] Ahmad R, Vaseem M, Tripathy N and Hahn Y-B 2013 Wide Linear-Range Detecting Nonenzymatic Glucose Biosensor Based on CuO Nanoparticles Inkjet-Printed on Electrodes *Analytical Chemistry* **85** 10448-54

[450] Molazemhosseini A, Magagnin L, Vena P and Liu C-C 2017 Single-use nonenzymatic glucose biosensor based on CuO nanoparticles ink printed on thin film gold electrode by micro-plotter technology *Journal of Electroanalytical Chemistry* **789** 50-7

[451] Batra N, Tomar M and Gupta V 2015 ZnO–CuO composite matrix based reagentless biosensor for detection of total cholesterol *Biosensors and Bioelectronics* **67** 263-71

[452] Akgul F A, Gumus C, Er A O, Farha A H, Akgul G, Ufuktepe Y and Liu Z 2013 Structural and electronic properties of SnO2 *Journal of Alloys and Compounds* **579** 50-6

[453] Shalan A E, Osama I, Rashad M M and Ibrahim I A 2014 An investigation on the properties of SnO2 nanoparticles synthesized using two different methods *Journal of Materials Science: Materials in Electronics* **25** 303-10

[454] Dieguez A, Romano-Rodrıguez A, Vila A and Morante J 2001 The complete Raman spectrum of nanometric SnO 2 particles *Journal of Applied Physics* **90** 1550-7

[455] Chen P-J and Jeng H-T 2015 Phase diagram of the layered oxide SnO: GW and electron-phonon studies *Scientific Reports* **5** 16359

[456] Zhou W and Umezawa N 2015 Band gap engineering of bulk and nanosheet SnO: an insight into the interlayer Sn-Sn lone pair interactions *Physical Chemistry Chemical Physics* **17** 17816-20

[457] Shin J H, Song J Y, Kim Y H and Park H M 2010 Low temperature and self-catalytic growth of tetragonal SnO nanobranch *Materials Letters* **64** 1120-2

[458] Javaid K, Xie Y F, Luo H, Wang M, Zhang H L, Gao J H, Zhuge F, Liang L Y and Cao H T 2016 The electrical properties of n-ZnO/p-SnO heterojunction diodes *Applied Physics Letters* **109** 123507

[459] Liang L Y, Liu Z M, Cao H T and Pan X Q 2010 Microstructural, optical, and electrical properties of SnO thin films prepared on quartz via a two-step method *ACS applied materials & interfaces* **2** 1060-5

[460] SnO Crystal Structure: Datasheet from "PAULING FILE Multinaries Edition – 2012" in SpringerMaterials (https://materials.springer.com/isp/crystallographic/docs/sd_0541683). Springer-Verlag Berlin Heidelberg & Material Phases Data System (MPDS), Switzerland & National Institute for Materials Science (NIMS), Japan)

[461] Diéguez A, Romano-Rodríguez A, Vilà A and Morante J R 2001 The complete Raman spectrum of nanometric SnO2 particles *Journal of Applied Physics* **90** 1550-7

[462] González G B 2012 Investigating the Defect Structures in Transparent Conducting Oxides Using X-ray and Neutron Scattering Techniques *Materials* **5** 818

[463] Giefers H, Koval S, Wortmann G, Sturhahn W, Alp E E and Hu M Y 2006 Phonon density of states of Sn in textured SnO under high pressure: Comparison of nuclear inelastic x-ray scattering spectra to a shell model *Physical Review B* **74** 094303

[464] Song P and Wen D 2009 Experimental Investigation of the Oxidation of Tin Nanoparticles *The Journal of Physical Chemistry C* **113** 13470-6

[465] Cheng Y, Huang J, Li J, Cao L and Qi H 2018 Hydrothermal synthesis of shape-controlled SnO as anode material for Li-ion batteries *IET Micro & Nano Letters* **13** 257-60

[466] Chiu H-C and Yeh C-S 2007 Hydrothermal Synthesis of SnO2 Nanoparticles and Their Gas-Sensing of Alcohol *The Journal of Physical Chemistry C* **111** 7256-9

[467] Du F, Guo Z and Li G 2005 Hydrothermal synthesis of SnO2 hollow microspheres *Materials Letters* **59** 2563-5

[468] Azam A, Habib S S, Salah N A and Ahmed F 2013 Microwave-assisted synthesis of SnO(2) nanorods for oxygen gas sensing at room temperature *International Journal of Nanomedicine* **8** 3875-82

[469] Salah N, AL-Shawafi W M, Alshahrie A, Habib S S and Azam A 2017 Microwave synthesis of 2D SnO nanosheets: effects of annealing temperatures on their thermoelectric properties *Journal of Materials Science: Materials in Electronics* **28** 3598-606

[470] Ibarguen C A, Mosquera A, Parra R, Castro M S and Rodríguez-Páez J E 2007 Synthesis of SnO2 nanoparticles through the controlled precipitation route *Materials Chemistry and Physics* **101** 433-40

[471] Rashad M M, Ibrahim I A, Osama I and Shalan A E 2014 Distinction between SnO2 nanoparticles synthesized using co-precipitation and solvothermal methods for the photovoltaic efficiency of dye-sensitized solar cells *Bulletin of Materials Science* **37** 903-9

[472] Marikkannan M, Vishnukanthan V, Vijayshankar A, Mayandi J and Pearce J M 2015 A novel synthesis of tin oxide thin films by the sol-gel process for optoelectronic applications *AIP Advances* **5** 027122

[473] Zhang J and Gao L 2004 Synthesis and characterization of nanocrystalline tin oxide by sol–gel method *Journal of solid state chemistry* **177** 1425-30

[474] Chatelon J P, Terrier C, Bernstein E, Berjoan R and Roger J A 1994 Morphology of SnO2 thin films obtaibed by the sol-gel technique *Thin Solid Films* **247** 162-8

[475] Fortunato E, Barros R, Barquinha P, Figueiredo V, Park S-H K, Hwang C-S and Martins R 2010 Transparent p-type SnOx thin film transistors produced by reactive rf magnetron sputtering followed by low temperature annealing *Applied Physics Letters* **97** 052105

[476] Gubbins M A, Casey V and Newcomb S B 2002 Nanostructural characterisation of SnO2 thin films prepared by reactive r.f. magnetron sputtering of tin *Thin Solid Films* **405** 270-5

[477] Nafiseh M, Mohammad R S, Elangovan E and Elvira F 2010 Characterization of SnO2:F thin films deposited by an economic spray pyrolysis technique *physica status solidi c* **7** 2277-81

[478] Patil G E, Kajale D D, Gaikwad V B and Jain G H 2012 Spray Pyrolysis Deposition of Nanostructured Tin Oxide Thin Films *ISRN Nanotechnology* **2012** 5

[479] Jun G, Florent H, Jeremy L and Xile H 2018 Densely Packed, Ultra Small SnO Nanoparticles for Enhanced Activity and Selectivity in Electrochemical CO2 Reduction *Angewandte Chemie International Edition* **57** 2943-7

[480] Patil G E, Kajale D D, Gaikwad V B and Jain G H 2012 Preparation and characterization of SnO2 nanoparticles by hydrothermal route *International Nano Letters* **2** 17

[481] Xi G and Ye J 2010 Ultrathin SnO2 Nanorods: Template- and Surfactant-Free Solution Phase Synthesis, Growth Mechanism, Optical, Gas-Sensing, and Surface Adsorption Properties *Inorganic Chemistry* **49** 2302-9

[482] Orlandi M O, Leite E R, Aguiar R, Bettini J and Longo E 2006 Growth of SnO nanobelts and dendrites by a self-catalytic VLS process *The Journal of Physical Chemistry B* **110** 6621-5

[483] Sun S H, Meng G W, Zhang G X, Gao T, Geng B Y, Zhang L D and Zuo J 2003 Raman scattering study of rutile SnO2 nanobelts synthesized by thermal evaporation of Sn powders *Chemical Physics Letters* **376** 103-7

[484] Ying Z, Wan Q, Song Z T and Feng S L 2005 Controlled synthesis of branched SnO2 nanowhiskers *Materials Letters* **59** 1670-2

[485] Jia Z-j, Zhu L-p, Liao G-h, Yu Y and Tang Y-w 2004 Preparation and characterization of SnO nanowhiskers *Solid State Communications* **132** 79-82

[486] Kolmakov A, Klenov D O, Lilach Y, Stemmer S and Moskovits M 2005 Enhanced Gas Sensing by Individual SnO2 Nanowires and Nanobelts Functionalized with Pd Catalyst Particles *Nano Letters* **5** 667-73

[487] Nam S-H and Boo J-H 2012 Rutile structured SnO2 nanowires synthesized with metal catalyst by thermal evaporation method *Journal of nanoscience and nanotechnology* **12** 1559-62

[488] Caraveo-Frescas J A and Alshareef H N 2013 Transparent p-type SnO nanowires with unprecedented hole mobility among oxide semiconductors *Applied Physics Letters* **103** 222103

[489] Iqbal M Z, Wang F, Zhao H, Rafique M Y, Wang J and Li Q 2012 Structural and electrochemical properties of SnO nanoflowers as an anode material for lithium ion batteries *Scripta Materialia* **67** 665-8

[490] Wu M, Zeng W and Li Y 2013 Hydrothermal synthesis of novel SnO2 nanoflowers and their gas-sensing properties *Materials Letters* **104** 34-6

[491] Gyger F, Hübner M, Feldmann C, Barsan N and Weimar U 2010 Nanoscale SnO2 Hollow Spheres and Their Application as a Gas-Sensing Material *Chemistry of Materials* **22** 4821-7

[492] Hossain M A, Yang G, Parameswaran M, Jennings J R and Wang Q 2010 Mesoporous SnO2 Spheres Synthesized by Electrochemical Anodization and Their Application in CdSe-Sensitized Solar Cells *The Journal of Physical Chemistry C* **114** 21878-84

[493] Zhu L, Yang H, Jin D and Zhu H 2007 Hydrothermal synthesis of SnO nanoflakes as anode materials for lithium-ion batteries *Inorganic Materials* **43** 1307-12

[494] Demir-Cakan R, Hu Y-S, Antonietti M, Maier J and Titirici M-M 2008 Facile One-Pot Synthesis of Mesoporous SnO2 Microspheres via Nanoparticles Assembly and Lithium Storage Properties *Chemistry of Materials* **20** 1227-9

[495] Son S Y, Hong S-A, Oh S Y, Lee Y-C, Lee G-W, Kang J W, Huh Y S and Kim I T 2018 Crab-Shell Biotemplated SnO2 Composite Anodes for Lithium-Ion Batteries *Journal of Nanoscience and Nanotechnology* **18** 6463-8

[496] Abanades S, Charvin P, Lemont F and Flamant G 2008 Novel two-step SnO2/SnO water-splitting cycle for solar thermochemical production of hydrogen *International Journal of Hydrogen Energy* **33** 6021-30

[497] Liu Y, Jiao Y, Zhang Z, Qu F, Umar A and Wu X 2014 Hierarchical SnO2 Nanostructures Made of Intermingled Ultrathin Nanosheets for Environmental Remediation, Smart Gas Sensor, and Supercapacitor Applications *ACS Applied Materials & Interfaces* **6** 2174-84

[498] Haspulat B, Sarıbel M and Kamış H 2017 Surfactant assisted hydrothermal synthesis of SnO nanoparticles with enhanced photocatalytic activity *Arabian Journal of Chemistry*

[499] Das S and Jayaraman V 2014 SnO2: A comprehensive review on structures and gas sensors *Progress in Materials Science* **66** 112-255

[500] Mei L, Chen Y and Ma J 2014 Gas Sensing of SnO2 Nanocrystals Revisited: Developing Ultra-Sensitive Sensors for Detecting the H2S Leakage of Biogas *Scientific Reports* **4** 6028

[501] Li C, Lv M, Zuo J and Huang X 2015 SnO(2) Highly Sensitive CO Gas Sensor Based on Quasi-Molecular-Imprinting Mechanism Design *Sensors (Basel, Switzerland)* **15** 3789-800

[502] Wu Q-H, Li J and Sun S-G 2010 Nano SnO2 gas sensors *Current Nanoscience* **6** 525-38

[503] Wang B, Sun L and Wang Y 2018 Template-free synthesis of nanosheets-assembled SnO2 hollow spheres for enhanced ethanol gas sensing *Materials Letters* **218** 290-4

[504] Huang J, Yu K, Gu C, Zhai M, Wu Y, Yang M and Liu J 2010 Preparation of porous flower-shaped SnO2 nanostructures and their gas-sensing property *Sensors and Actuators B: Chemical* **147** 467-74

[505] Lipeng Q, Jiaqiang X, Xiaowen D, Qingyi P, Zhixuan C, Qun X and Feng L 2008 The template-free synthesis of square-shaped SnO 2 nanowires: the temperature effect and acetone gas sensors *Nanotechnology* **19** 185705

[506] Chen Y J, Xue X Y, Wang Y G and Wang T H 2005 Synthesis and ethanol sensing characteristics of single crystalline SnO2 nanorods *Applied Physics Letters* **87** 233503

[507] Liu X, Ma T, Xu Y, Sun L, Zheng L, Schmidt O G and Zhang J 2018 Rolled-up SnO2 nanomembranes: A new platform for efficient gas sensors *Sensors and Actuators B: Chemical* **264** 92-9

[508] Kuang X, Liu T, Shi D, Wang W, Yang M, Hussain S, Peng X and Pan F 2016 Hydrothermal synthesis of hierarchical SnO2 nanostructures made of superfine nanorods for smart gas sensor *Applied Surface Science* **364** 371-7

[509] Young-Jin C, In-Sung H, Jae-Gwan P, Kyoung Jin C, Jae-Hwan P and Jong-Heun L 2008 Novel fabrication of an SnO 2 nanowire gas sensor with high sensitivity *Nanotechnology* **19** 095508

[510] Suman P H, Felix A A, Tuller H L, Varela J A and Orlandi M O 2013 Giant Chemo-Resistance of SnO disk-like structures *Sensors and Actuators B: Chemical* **186** 103-8

[511] Suman P H, Felix A A, Tuller H L, Varela J A and Orlandi M O 2015 Comparative gas sensor response of SnO2, SnO and Sn3O4 nanobelts to NO2 and potential interferents *Sensors and Actuators B: Chemical* **208** 122-7

[512] Wan Q and Wang T H 2005 Single-crystalline Sb-doped SnO2 nanowires: synthesis and gas sensor application *Chemical Communications* 3841-3

[513] Wei Y, Yi G, Xu Y, Zhou L, Wang X, Cao J, Sun G, Chen Z, Hari B and Zhang Z 2017 Synthesis, characterization, and gas-sensing properties of Ag/SnO2/rGO composite by a hydrothermal method *Journal of Materials Science: Materials in Electronics* **28** 17049-57

[514] Yin L, Chen D, Cui X, Ge L, Yang J, Yu L, Zhang B, Zhang R and Shao G 2014 Normal-pressure microwave rapid synthesis of hierarchical SnO2@rGO nanostructures with superhigh surface areas as high-quality gas-sensing and electrochemical active materials *Nanoscale* **6** 13690-700

[515] Su P-G and Yang L-Y 2016 NH3 gas sensor based on Pd/SnO2/RGO ternary composite operated at room-temperature *Sensors and Actuators B: Chemical* **223** 202-8

[516] Li F, Gao X, Wang R and Zhang T 2018 Design of WO3-SnO2 core-shell nanofibers and their enhanced gas sensing performance based on different work function *Applied Surface Science* **442** 30-7

[517] Liu J, Wang T, Wang B, Sun P, Yang Q, Liang X, Song H and Lu G 2017 Highly sensitive and low detection limit of ethanol gas sensor based on hollow ZnO/SnO2 spheres composite material *Sensors and Actuators B: Chemical* **245** 551-9

[518] Li L, Zhang C and Chen W 2015 Fabrication of SnO2-SnO nanocomposites with p-n heterojunctions for the low-temperature sensing of NO2 gas *Nanoscale* **7** 12133-42

[519] Chen W, Li Q, Gan H and Zeng W 2014 Study of CuO–SnO2 heterojunction nanostructures for enhanced CO gas sensing properties *Advances in Applied Ceramics* **113** 139-46

[520] Wang Q, Kou X, Liu C, Zhao L, Lin T, Liu F, Yang X, Lin J and Lu G 2018 Hydrothermal synthesis of hierarchical CoO/SnO2 nanostructures for ethanol gas sensor *Journal of Colloid and Interface Science* **513** 760-6

[521] Gao H, Zhao L, Wang L, Sun P, Lu H, Liu F, Chuai X and Lu G 2018 Ultrasensitive and low detection limit of toluene gas sensor based on SnO2-decorated NiO nanostructure *Sensors and Actuators B: Chemical* **255** 3505-15

[522] Parthibavarman M, Hariharan V and Sekar C 2011 High-sensitivity humidity sensor based on SnO2 nanoparticles synthesized by microwave irradiation method *Materials Science and Engineering: C* **31** 840-4

[523] Li W, Liu J, Ding C, Bai G, Xu J, Ren Q and Li J 2017 Fabrication of Ordered SnO2 Nanostructures with Enhanced Humidity Sensing Performance *Sensors* **17** 2392

[524] Yin M, Yang F, Wang Z, Zhu M, Liu M, Xu X and Li Z 2017 A Fast Humidity Sensor Based on Li(+)-Doped SnO(2) One-Dimensional Porous Nanofibers *Materials* **10** 535

[525] Song X, Qi Q, Zhang T and Wang C 2009 A humidity sensor based on KCl-doped SnO2 nanofibers *Sensors and Actuators B: Chemical* **138** 368-73

[526] Ismail A S, Mamat M H, Malek M F, Yusoff M M, Mohamed R, Sin N D M, Suriani A B and Rusop M 2018 Heterogeneous SnO2/ZnO nanoparticulate film: Facile synthesis and humidity sensing capability *Materials Science in Semiconductor Processing* **81** 127-38

[527] Tai W-P and Oh J-H 2002 Fabrication and humidity sensing properties of nanostructured TiO2–SnO2 thin films *Sensors and Actuators B: Chemical* **85** 154-7

[528] Zhang D, Sun Y e, Li P and Zhang Y 2016 Facile Fabrication of MoS2-Modified SnO2 Hybrid Nanocomposite for Ultrasensitive Humidity Sensing *ACS Applied Materials & Interfaces* **8** 14142-9

[529] Yadav B C, Sharma P and Khanna P K 2011 Morphological and humidity sensing characteristics of SnO2-CuO, SnO2-Fe2O3 and SnO2-SbO2 nanocooxides *Bulletin of Materials Science* **34** 689

[530] Karthick S, Lee H-S, Kwon S-J, Natarajan R and Saraswathy V 2016 Standardization, Calibration, and Evaluation of Tantalum-Nano rGO-SnO2 Composite as a Possible Candidate Material in Humidity Sensors *Sensors* **16** 2079

[531] Yujin C, Chunling Z, Maosheng C and Taihong W 2007 Photoresponse of SnO 2 nanobelts grown in situ on interdigital electrodes *Nanotechnology* **18** 285502

[532] Wu J-M and Kuo C-H 2009 Ultraviolet photodetectors made from SnO2 nanowires *Thin Solid Films* **517** 3870-3

[533] Hu L, Yan J, Liao M, Wu L and Fang X 2011 Ultrahigh External Quantum Efficiency from Thin SnO2 Nanowire Ultraviolet Photodetectors *Small* **7** 1012-7

[534] Sharma P and Sawyer S 2016 *A high responsivity SnO2 hollow nanospheres based ultraviolet photodetector*: IEEE)

[535] Lu M-L, Weng T-M, Chen J-Y and Chen Y-F 2012 Ultrahigh-gain single SnO2 nanowire photodetectors made with ferromagnetic nickel electrodes *Npg Asia Materials* **4** e26

[536] Xie T, Hasan M R, Qiu B, Arinze E S, Nguyen N V, Motayed A, Thon S M and Debnath R 2015 High-performing visible-blind photodetectors based on SnO2/CuO nanoheterojunctions *Applied Physics Letters* **107** 241108

[537] Zheng L, Xiaoli Y, Haoran C and Zhongzhu L 2018 Flexible ultraviolet photodetectors based on ZnO–SnO 2 heterojunction nanowire arrays *Journal of Semiconductors* **39** 024002

[538] Tian W, Zhai T, Zhang C, Li S L, Wang X, Liu F, Liu D, Cai X, Tsukagoshi K, Golberg D and Bando Y 2013 Low-Cost Fully Transparent Ultraviolet Photodetectors Based on Electrospun ZnO-SnO2 Heterojunction Nanofibers *Advanced Materials* **25** 4625-30

[539] Li X, Gao C, Duan H, Lu B, Wang Y, Chen L, Zhang Z, Pan X and Xie E 2012 High-Performance Photoelectrochemical-Type Self-Powered UV Photodetector Using Epitaxial TiO2/SnO2 Branched Heterojunction Nanostructure *Small* **9** 2005-11

[540] Gao C, Li X, Zhu X, Chen L, Wang Y, Teng F, Zhang Z, Duan H and Xie E 2014 High performance, self-powered UV-photodetector based on ultrathin, transparent, SnO2–TiO2 core–shell electrodes *Journal of Alloys and Compounds* **616** 510-5

[541] Huang Y, Yu Q, Wang J, Li X, Yan Y, Gao S, Shi F, Wang D and Yu C 2015 A high-performance self-powered UV photodetector based on SnO2 mesoporous spheres @ TiO2 *Electronic Materials Letters* **11** 1059-65

[542] Liu J, Li Y, Huang X and Zhu Z 2010 Tin Oxide Nanorod Array-Based Electrochemical Hydrogen Peroxide Biosensor *Nanoscale Research Letters* **5** 1177

[543] Haider A J, Jasim Mohammed A, Shaker S S, Yahya K Z and Haider M J 2017 Sensing Characteristics of Nanostructured SnO2 Thin Films as Glucose Sensor *Energy Procedia* **119** 473-81

[544] Li L, Huang J, Wang T, Zhang H, Liu Y and Li J 2010 An excellent enzyme biosensor based on Sb-doped SnO2 nanowires *Biosensors and Bioelectronics* **25** 2436-41

[545] Lavanya N, Radhakrishnan S and Sekar C 2012 Fabrication of hydrogen peroxide biosensor based on Ni doped SnO2 nanoparticles *Biosensors and Bioelectronics* **36** 41-7

[546] Lavanya N, Radhakrishnan S, Sekar C, Navaneethan M and Hayakawa Y 2013 Fabrication of Cr doped SnO2 nanoparticles based biosensor for the selective determination of riboflavin in pharmaceuticals *Analyst* **138** 2061-7

[547] Shen Q, Jiang J, Liu S, Han L, Fan X, Fan M, Fan Q, Wang L and Huang W 2014 *Facile synthesis of Au-SnO2 hybrid nanospheres with enhanced photoelectrochemical biosensing performance* vol 6

[548] Wu R, Chen X and Hu J 2012 Synthesis, characterization, and biosensing application of ZnO/SnO2 heterostructured nanomaterials *Journal of Solid State Electrochemistry* **16** 1975-82

[549] Zhu C, Fang Y, Wen D and Dong S 2011 One-pot synthesis of functional two-dimensional graphene/SnO2 composite nanosheets as a building block for self-assembly and an enhancing nanomaterial for biosensing *Journal of Materials Chemistry* **21** 16911-7

[550] Li F, Song J, Li F, Wang X, Zhang Q, Han D, Ivaska A and Niu L 2009 Direct electrochemistry of glucose oxidase and biosensing for glucose based on carbon nanotubes@SnO2-Au composite *Biosensors and Bioelectronics* **25** 883-8

[551] Yang L, Zhou Q, Wang G and Yang Y 2013 *Acetylcholinesterase biosensor based on SnO2 nanoparticles–carboxylic graphene–nafion modified electrode for detection of pesticides* vol 49C

[552] Chen D, Sun X, Guo Y, Qiao L and Wang X 2015 Acetylcholinesterase biosensor based on multi-walled carbon nanotubes-SnO2-chitosan nanocomposite *Bioprocess and Biosystems Engineering* **38** 315-21

[553] Kaçar C, Erden P E and Kılıç E 2017 Amperometric l-lysine biosensor based on carboxylated multiwalled carbon nanotubes-SnO2 nanoparticles-graphene composite *Applied Surface Science* **419** 916-23

[554] Schoiswohl J, Surnev S, Netzer F P and Kresse G 2006 Vanadium oxide nanostructures: from zero- to three-dimensional *Journal of Physics: Condensed Matter* **18** R1

[555] Fu H, Jiang X, Yang X, Yu A, Su D and Wang G 2012 Glycothermal synthesis of assembled vanadium oxide nanostructures for gas sensing *J Nanopart Res* **14** 871

[556] Naoufal B and Damien L 2014 Vanadium Oxide Compounds: Structure, Properties, and Growth from the Gas Phase *Chemical Vapor Deposition* **20** 299-311

[557] Peys N, Ling Y, Dewulf D, Gielis S, De Dobbelaere C, Cuypers D, Adriaensens P, Van Doorslaer S, De Gendt S, Hardy A and Van Bael M K 2013 V6O13 films by control of the oxidation state from aqueous precursor to crystalline phase *Dalton Transactions* **42** 959-68

[558] Haihong Y, Ke Y, Zhengli Z, Min Z, Lei L and Ziqiang Z 2011 Humidity Sensing Properties of Flower-Like VO2(B) and VO2(M) Nanostructures *Electroanalysis* **23** 1752-8

[559] Leroux C, Nihoul G and Van Tendeloo G 1998 From ${\mathrm{VO}}_{2}(B)$ to ${\mathrm{VO}}_{2}(R):$ Theoretical structures of ${\mathrm{VO}}_{2}$ polymorphs and in situ electron microscopy *Physical Review B* **57** 5111-21

[560] Lee S, Ivanov I N, Keum J K and Lee H N 2016 Epitaxial stabilization and phase instability of VO2 polymorphs *Scientific Reports* **6** 19621

[561] Zhang S, Shang B, Yang J, Yan W, Wei S and Xie Y 2011 From VO2 (B) to VO2 (A) nanobelts: first hydrothermal transformation, spectroscopic study and first principles calculation *Physical Chemistry Chemical Physics* **13** 15873-81

[562] Li H, He P, Wang Y, Hosono E and Zhou H 2011 High-surface vanadium oxides with large capacities for lithium-ion batteries: from hydrated aerogel to nanocrystalline VO2(B), V6O13 and V2O5 *Journal of Materials Chemistry* **21** 10999-1009

[563] Hongbo Q, Memgmeng Y, Yongqi D, Han X, Bin H, Yueliang G, Yuanjun Y, Chongwen Z, Zhenlin L and Chen G 2015 The tetragonal-like to rutile structural phase transition in epitaxial VO 2 /TiO 2 (001) thick films *New Journal of Physics* **17** 113016

[564] Belbeoch B, Kleinberger R and Roulliay M 1978 Correlation between the high temperature anomalies in V2O3 and the lattice parameters *Journal of Physics and Chemistry of Solids* **39** 1007-12

[565] Liu J, Xia H, Xue D and Lu L 2009 Double-Shelled Nanocapsules of V2O5-Based Composites as High-Performance Anode and Cathode Materials for Li Ion Batteries *Journal of the American Chemical Society* **131** 12086-7

[566] Mettan Y, Caputo R and Chatterji T 2015 A theoretical and experimental study of the crystal structure of H2V3O8 *RSC Advances* **5** 106543-50

[567] Yamazaki S, Li C, Ohoyama K, Nishi M, Ichihara M, Ueda H and Ueda Y 2010 Synthesis, structure and magnetic properties of V4O9—A missing link in binary vanadium oxides *Journal of Solid State Chemistry* **183** 1496-503

[568] Horiuchi S, Saeki M, Matsui Y and Nagata F 1975 *Transition of V6O13 to VO2 observed with a high-resolution electron microscope* vol 31

[569] Dai L, Gao Y, Cao C, Chen Z, Luo H, Kanehira M, Jin J and Liu Y 2012 VO2 (A) nanostructures with controllable feature sizes and giant aspect ratios: one-step hydrothermal synthesis and lithium-ion battery performance *RSC Advances* **2** 5265-70

[570] Kysar J S, Wignes F L and Sekhar P K 2017 Growth Mechanism of Vanadium (II) Oxide Nanowires *IEEE Transactions on Nanotechnology* **16** 3-10

[571] V. G A, M. B S, A. G E, N. R M, M. G A, Alexander B and D. T Y 2010 Synthesis, Structure, and Sensor Properties of Vanadium Pentoxide Nanorods *European Journal of Inorganic Chemistry* **2010** 5247-53

[572] Wu M, Zhang X, Gao S, Cheng X, Rong Z, Xu Y, Zhao H and Huo L 2013 Construction of monodisperse vanadium pentoxide hollow spheres via a facile route and triethylamine sensing property *CrystEngComm* **15** 10123-31

[573] Nakano M, Shibuya K, Ogawa N, Hatano T, Kawasaki M, Iwasa Y and Tokura Y 2013 Infrared-sensitive electrochromic device based on VO2 *Applied Physics Letters* **103** 153503

[574] Gonçalves A, Resende J, Marques A C, Pinto J V, Nunes D, Marie A, Goncalves R, Pereira L, Martins R and Fortunato E 2016 Smart optically active VO2 nanostructured layers applied in roof-type ceramic tiles for energy efficiency *Solar Energy Materials and Solar Cells* **150** 1-9

[575] Lim H, Stavrias N, Johnson B, Marvel R, Haglund R and McCallum J 2014 *Optical Switching and Photoluminescence in Erbium Implanted Vanadium Dioxide Thin Films* vol 115

[576] McGahan C, Appavoo K, Jr. R F H and Shapera E P 2013 Switchable plasmon-induced transparency in gold nanoarrays on vanadium dioxide film *Journal of Vacuum Science & Technology B* **31** 06FE1

[577] Yang Y, Strong K, Pandey G P and Meda L 2018 Nanostructured V2O5/Nitrogen-doped Graphene Hybrids for High Rate Lithium Storage *MRS Advances* 1-6

[578] Lee J, Badie S, Srimuk P, Ridder A, Shim H, Choudhury S, Nah Y-C and Presser V 2018 Electrodeposition of hydrated vanadium pentoxide on nanoporous carbon cloth for hybrid energy storage *Sustainable Energy & Fuels* **2** 577-88

[579] J. L, X. W, Q. P and Y. L 2005 Vanadium Pentoxide Nanobelts: Highly Selective and Stable Ethanol Sensor Materials *Advanced Materials* **17** 764-7

[580] Liang J, Zhu K, Yang R and Hu M 2018 Room temperature NO2 sensing properties of Au-decorated vanadium oxide nanowires sensor *Ceramics International* **44** 2261-8

[581] Vernardou D, Sapountzis A, Spanakis E, Kenanakis G, Koudoumas E and Katsarakis N 2013 Electrochemical Activity of Electrodeposited V2O5 Coatings *Journal of The Electrochemical Society* **160** D6-D9

[582] Rasoulis M and Vernardou D 2017 Electrodeposition of Vanadium Oxides at Room Temperature as Cathodes in Lithium-Ion Batteries *Coatings* **7** 100

[583] Araújo E S, Libardi J, Faia P M and de Oliveira H P 2018 Characterization and Electrical Response to Humidity of Sintered Polymeric Electrospun Fibers of Vanadium Oxide-($${\hbox{TiO}}_{{2}} /{\hbox{WO}}_{{3}} $$ TiO 2 / WO 3) *Journal of Electronic Materials* **47** 2710-7

[584] Grigorieva A V, Goodilin E A, Anikina A V, Kolesnik I V and Tretyakov Y D 2008 Surfactants in the formation of vanadium oxide nanotubes *Mendeleev Communications* **18** 71-2

[585] Niederberger M, Muhr H-J, Krumeich F, Bieri F, Günther D and Nesper R 2000 Low-Cost Synthesis of Vanadium Oxide Nanotubes via Two Novel Non-Alkoxide Routes *Chemistry of Materials* **12** 1995-2000

[586] Khan Z, Senthilkumar B, Park S O, Park S, Yang J, Lee J H, Song H-K, Kim Y, Kwak S K and Ko H 2017 Carambola-shaped VO2 nanostructures: a binder-free air electrode for an aqueous Na-air battery *Journal of Materials Chemistry A* **5** 2037-44

[587] Schneider K, Lubecka M and Czapla A 2016 V2O5 thin films for gas sensor applications *Sensors and Actuators B: Chemical* **236** 970-7

[588] Qu W and Meyer J-U 1997 A novel thick-film ceramic humidity sensor *Sensors and Actuators B: Chemical* **40** 175-82

[589] Evans G P, Powell M J, Johnson I D, Howard D P, Bauer D, Darr J A and Parkin I P 2018 Room temperature vanadium dioxide–carbon nanotube gas sensors made via continuous hydrothermal flow synthesis *Sensors and Actuators B: Chemical* **255** 1119-29

[590] Zhai T, Liu H, Li H, Fang X, Liao M, Li L, Zhou H, Koide Y, Bando Y and Golberg D 2010 Centimeter-Long V2O5 Nanowires: From Synthesis to Field-Emission, Electrochemical, Electrical Transport, and Photoconductive Properties *Advanced Materials* **22** 2547-52

[591] Wu J M and Chang W E 2014 Ultrahigh Responsivity and External Quantum Efficiency of an Ultraviolet-Light Photodetector Based on a Single VO2 Microwire *ACS Applied Materials & Interfaces* **6** 14286-92

[592] Miyazaki H, Matsuura T and Ota T 2017 Vanadium oxide-based photochromic composite film *RSC Advances* **7** 2388-91

[593] Srivastava T, Bajpai G, Rathore G, Liu S W, Biring S and Sen S 2018 Vanadium substitution: A simple and economic way to improve UV sensing in ZnO *Journal of Applied Physics* **123** 161407

[594] Alagappan L P, Shanmugasundaram P, Ramachandra B L, Gumpu M B, Nesakumar N, Jayanth Babu K, Vedantham S and Balaguru Rayappan J B 2017 Fabrication of electrochemical biosensor with vanadium pentoxide nano-interface for the detection of methylglyoxal in rice *Analytical Biochemistry* **528** 19-25

[595] Suresh R, Giribabu K, Manigandan R, Kumar S P, Munusamy S, Muthamizh S, Stephen A and Narayanan V 2014 New electrochemical sensor based on Ni-doped V2O5 nanoplates modified glassy carbon electrode for selective determination of dopamine at nanomolar level *Sensors and Actuators B: Chemical* **202** 440-7

[596] Yang F, Jiang X, Zhong X, Wei S and Yuan R 2018 Highly sensitive electrochemiluminescence detection of mucin1 based on V2O5 nanospheres as peroxidase mimetics to catalyze H2O2 for signal amplification *Sensors and Actuators B: Chemical* **265** 126-33

[597] Hu X, Goud K Y, Kumar V S, Catanante G, Li Z, Zhu Z and Marty J L 2018 Disposable electrochemical aptasensor based on carbon nanotubes- V2O5-chitosan nanocomposite for detection of ciprofloxacin *Sensors and Actuators B: Chemical* **268** 278-86

[598] Sun W, Qin P, Gao H, Li G and Jiao K 2010 Electrochemical DNA biosensor based on chitosan/nano-V2O5/MWCNTs composite film modified carbon ionic liquid electrode and its application to the LAMP product of Yersinia enterocolitica gene sequence *Biosensors and Bioelectronics* **25** 1264-70

[599] Zhu L and Zeng W 2017 Room-temperature gas sensing of ZnO-based gas sensor: A review *Sensors and Actuators A: Physical* **267** 242-61

[600] Long H, Zeng W and Zhang H 2015 Synthesis of WO3 and its gas sensing: a review *Journal of Materials Science: Materials in Electronics* **26** 4698-707

[601] Kaisti M 2017 Detection principles of biological and chemical FET sensors *Biosensors and Bioelectronics* **98** 437-48

[602] Feng P, Shao F, Shi Y and Wan Q 2014 Gas Sensors Based on Semiconducting Nanowire Field-Effect Transistors *Sensors* **14** 17406

[603] Nunes D, Santos L, Pimental A, Barquinha P, Pereira L, Fortunato E and Martins R 2018 *Metal Oxide Nanostructures: Synthesis, Properties and Applications*: Elsevier)

[604] Diao F and Wang Y 2018 Transition metal oxide nanostructures: premeditated fabrication and applications in electronic and photonic devices *Journal of Materials Science* **53** 4334-59

[605] Xiang J K, Ji Hun; Lu, Wei 2014 *Semiconductor Nanowires: From Next-Generation Electronics to Sustainable Energy,* ed W X Lu, Jie (Cambridge: Royal Society of Chemistry)

[606] Mathews N, Varghese B, Sun C, Thavasi V, Andreasson B P, Sow C H, Ramakrishna S and Mhaisalkar S G 2010 Oxide nanowire networks and their electronic and optoelectronic characteristics *Nanoscale* **2** 1984-98

[607] Chang P C and Lu J G 2008 ZnO Nanowire Field-Effect Transistors *IEEE Transactions on Electron Devices* **55** 2977-87

[608] Ju S, Lee K, Yoon M-H, Facchetti A, Marks T, J. and Janes D 2007 High performance ZnO nanowire field effect transistors with organic gate

nanodielectrics: effects of metal contacts and ozone treatment *Nanotechnology* **18** 155201

[609] Tiong T-Y, Dee C-F, Hamzah A A, Goh B T, Wong Y-Y, Ooi L, Majlis B Y, Salleh M M and Ahmad I 2017 A rapid responding ultraviolet sensor based on multi-parallel aligned ZnO nanowires field effect transistor *Sensors and Actuators A: Physical* **260** 139-45

[610] Liu X, Lin P, Yan X, Kang Z, Zhao Y, Lei Y, Li C, Du H and Zhang Y 2013 Enzyme-coated single ZnO nanowire FET biosensor for detection of uric acid *Sensors and Actuators B: Chemical* **176** 22-7

[611] Lundström I, Shivaraman S, Svensson C and Lundkvist L 1975 A hydrogen−sensitive MOS field−effect transistor *Applied Physics Letters* **26** 55-7

[612] Zhao X, Cai B, Tang Q, Tong Y and Liu Y 2014 One-Dimensional Nanostructure Field-Effect Sensors for Gas Detection *Sensors* **14** 13999

[613] Andringa A-M, Piliego C, Katsouras I, Blom P W M and Leeuw D M d 2014 NO2 Detection and Real-Time Sensing with Field-Effect Transistors *Chemistry of Materials* **26** 773-85

[614] Choi K J and Jang H W 2010 One-Dimensional Oxide Nanostructures as Gas-Sensing Materials: Review and Issues *Sensors* **10** 4083

[615] Zhang Y, Kolmakov A, Chretien S, Metiu H and Moskovits M 2004 Control of Catalytic Reactions at the Surface of a Metal Oxide Nanowire by Manipulating Electron Density Inside It *Nano Letters* **4** 403-7

[616] Vomiero A, Bianchi S, Comini E, Faglia G, Ferroni M and Sberveglieri G 2007 Controlled Growth and Sensing Properties of In2O3 Nanowires *Crystal Growth & Design* **7** 2500-4

[617] Yoshizumi T and Miyahara Y 2017 *Different Types of Field-Effect Transistors,* ed M Pejović: Intech)

[618] Kuang Q, Lao C-S, Li Z, Liu Y-Z, Xie Z-X, Zheng L-S and Wang Z L 2008 Enhancing the Photon- and Gas-Sensing Properties of a Single SnO 2 Nanowire Based Nanodevice by Nanoparticle Surface Functionalization *The Journal of Physical Chemistry C* **112** 11539-44

[619] Syed M and Martin M 2011 Gate-Tunable Surface Processes on a Single-Nanowire Field-Effect Transistor *Advanced Materials* **23** 2306-12

[620] Dattoli E N, Davydov A V and Benkstein K D 2012 Tin oxide nanowire sensor with integrated temperature and gate control for multi-gas recognition *Nanoscale* **4** 1760-9

[621] Matt L, Hannes K, Benjamin M, Franklin K and Peidong Y 2002 Photochemical Sensing of NO2 with SnO2 Nanoribbon Nanosensors at Room Temperature *Angewandte Chemie* **114** 2511-4

[622] Sharma B, Sharma A and Kim J-S 2018 Recent advances on H2 sensor technologies based on MOX and FET devices: A review *Sensors and Actuators B: Chemical* **262** 758-70